NASA CR-112012

INVESTIGATION OF SINGLE CRYSTAL FERRITE THIN FILMS

By:

J. E. Mee, P. J. Besser, P. E. Elkins

H. L. Glass and E. C. Whitcomb

February 1972

Prepared under Contract No. NAS 12-522 by

NORTH AMERICAN ROCKWELL CORPORATION

Anaheim, California

Langley Research Center

NATIONAL AERONAUTICS AND SPACE ADMINISTRATION

Dr. Robert L. Stermer
Technical Monitor
NAS 12-522
NASA Langley Research Center
Hampton, Virginia 23365

"Requests for copies of this report
should be referred to
NASA Scientific and Technical Information Facility
P.O. Box 33, College Park, Maryland 20740"

NASA CR-112012

INVESTIGATION OF SINGLE CRYSTAL FERRITE THIN FILMS

By:

J. E. Mee, P. J. Besser, P. E. Elkins

H. L. Glass and E. C. Whitcomb

February 1972

Prepared under Contract No. NAS 12-522 by

NORTH AMERICAN ROCKWELL CORPORATION

Anaheim, California

Langley Research Center

NATIONAL AERONAUTICS AND SPACE ADMINISTRATION

CONTENTS

		Page
1.0	SUMMARY	1
2.0	INTRODUCTION	2
	2.1 History of Fabrication of Epitaxial Garnets	2
	2.2 Report Organization	3
3.0	REVIEW OF MAGNETIC BUBBLE DOMAINS AND GARNETS	5
	3.1 Material Requirements for Bubble Domains	7
	3.1.1 Requirements for the existence of bubble domains	7
	3.1.2 Requirements for desirable bubble diameters	10
	3.1.3 Requirements for highly mobile bubble domains	10
	3.1.4 Requirements for temperature stability	11
	3.1.5 Summary of material requirements	11
	3.2 Properties of Magnetic Garnets	12
	3.2.1 Effect of temperature	13
	3.2.2 Effect of composition	15
	3.3 Potential Materials	15
4.0	MATERIALS FABRICATION	19
	4.1 Substrate Preparation	19
	4.1.1 Introduction	19
	4.1.2 Experimental	20
	4.1.3 Results	23
	4.1.4 Discussion	27
	4.1.5 Conclusions	29
	4.1.6 Recommendations for future work	33
	4.2 Epitaxial Deposition	33
	4.2.1 Introduction	33
	4.2.2 Reactors	35
	4.2.3 Source materials	37
	4.2.4 Film growth	38
	4.2.5 Film Compositions	38
	4.2.6 Composition determination	46
	4.2.7 Typical run sequence	48
5.0	MATERIALS CHARACTERIZATION	54
	5.1 Introduction	54
	5.2 Thermal Expansion	56
	5.2.1 Apparatus	56
	5.2.2 Thermal expansion data	59
	5.3 Stress Model	64
	5.4 Film/Substrate Crystal Quality	65
	5.4.1 X-ray diffraction topography	65
	5.4.2 Experimental procedure and results	65
	5.4.3 Discussion	81
	5.5 Film-Substrate Lattice Parameter Difference and Film Lattice Parameter	84
	5.6 Film Thickness	86

Page

5.7 Domain Structure and Film Crazing Observations 87
5.8 Bubble Diameter as a Function of Bias Field and Temperature 94
5.9 Magnetization 100
5.10 Characteristic Length 102
5.11 Wall Energy 102
5.12 Ferromagnetic Resonance 102
5.13 Anisotropy Field 104
5.14 Wall Coercive Force 104
5.15 Domain Wall Mobility 105
5.16 Heat Treatment of Films 106
5.17 Characteristics of a Typical Bubble-Domain Film of $Y_{3-z}Gd_zGa_xFe_{5-x}O_{12}$ 107
5.18 Bubble Propagation 109
6.0 CONCLUSIONS 111
6.1 Program Results 111
6.2 Discussion of Bubble-Material Technology 113
6.3 Future Work 115
APPENDIX 120
NEW TECHNOLOGY APPENDIX 139

ILLUSTRATIONS

Figure		Page
1.	Magnetic Domain Patterns in a Uniaxial Material Viewed Along the Easy Axis by the Faraday Effect	6
2.	Relative Orientation of Sublattice Magnetizations in Garnets	13
3.	Magnetization as a Function of Temperature for Several Magnetic Garnets	14
4.	Variation of Room-Temperature Magnetization with Ga Content in Yttrium-Gadolinium-Iron Garnet System	16
5.	A. D. Little Crystal-Growth Furnace	21
6.	Crucible Setup for the Growth of the Rare-Earth Gallium Garnets	22
7.	$Nd_3Ga_5O_{12}$ Boule	24
8.	$Sm_3Ga_5O_{12}$ Boule	24
9.	$Gd_3Ga_5O_{12}$ Boule	25
10.	$Sm_{0.48}Gd_{2.54}Ga_5O_{12}$ Boule	25
11.	Optical Transmission Spectra of $Nd_3Ga_5O_{12}$	30
12.	Optical Transmission Spectra of $Sm_3Ga_5O_{12}$	31
13.	Optical Transmission Spectra of $Gd_3Ga_5O_{12}$	32
14.	The T Reactor for Garnet Depositions	34
15.	Typical Three-Zone Profile for Reactor AG-1	36
16.	Gallium Chloride Injection Apparatus	39
17.	Typical Domains in YGdIG Films	41
18.	Typical Rough YGdIG Films on SmGaG Under Previous Growth Conditions (AG-2, Run 484, 111X Magnification)	42
19.	Best Area in YGdIG Films on SmGaG Under Previous Growth Conditions (AG-2, Run 482, 115X Magnification)	42
20.	Typical Area in YGdIG Films on SmGaG Under Present Growth Conditions (AG-2, Run 489, 115X Magnification) (Photograph taken under same microscope lighting conditions as figure 19.)	45
21.	$\Delta a_0/a_0$ vs Absolute Temperature	57
22.	Thermal Expansion Apparatus	58
23.	Lang Topographic Technique	66
24.	Lang Transmission Topograph of Thin (111) GdGaG Wafer; Boule A, $AgK\alpha_1$ Radiation, $(04\bar{4})$ Reflection, 7.3X Magnification	68
25.	Lang Transmission Topograph of Thin (111) GdGaG Wafer; Boule B, $AgK\alpha_1$ Radiation, $(\bar{4}22)$ Relfection, 3.5X Magnification	68
26.	Lang Transmission Topograph of Thin (111) GdGaG Wafer; Boule B, $AgK\alpha_1$ Radiation $(4\bar{2}\bar{2})$ Reflection, 3.8X Magnification. Slice adjacent to that shown in figure 25.	69
27.	Lang Transmission Topograph of Thin (111) GdGaG Wafer; Boule C, $AgK\alpha_1$ Radiation $(\bar{4}22)$ Reflection, 3.9X Magnification	69
28.	Lang Transmission Topograph of Thin (012) GdGaG Wafer; Boule C, $AgK\alpha_1$ Radiation $(24\bar{2})$ Reflection, 3.5X Magnification	70
29.	Relfection Topography on Lang Camera	70

Figure		Page
30.	Scanning Reflection Topograph of Thin (111) GdGaG Wafer; Boule A, $CuK\alpha_1$ Radiation (888) Reflection 12X Magnification	71
31.	Scanning Reflection Topograph of Thin (111) GdGaG Wafer; Boule B, $FeK\alpha_1$ Radiation, (444) Reflection, 5.8X Magnification	71
32.	Scanning Reflection Topograph of Thin (111) GdGaG Wafer; Boule B, $FeK\alpha_1$ Radiation, (444) Reflection, 5.3X Magnification	72
33.	Scanning Reflection Topograph of Thin (111) GdGaG Wafer; Boule C, $FeK\alpha_1$ Radiation, (444) Reflection, 4.5X Magnification	72
34.	Scanning Reflection Topograph of Thin (012) GdGaG Wafer, Boule C, $FeK\alpha_1$ Radiation, (048) Reflection, 4.8X Magnification	73
35.	Scanning Reflection Topograph of Thick (111) GdGaG Wafer; Boule D, $CuK\alpha_1$ Radiation, (888) Reflection, 5.4X Magnification	74
36.	Scanning Reflection Topograph of Thick (111) GdGaG Wafer; Boule B, $CrK\alpha_1$ Radiation, (444) Reflection, 4.5X Magnification	74
37.	Scanning Reflection Topograph of Thick (111) GdGaG Wafer; Boule B, $FeK\alpha_1$ Radiation, (444) Reflection, 5.7X Magnification	75
38.	Scanning Reflection Topograph of Thick (111) DyGdGaG Wafer; Boule E, $FeK\alpha_1$ Radiation, (888) Reflection, 4.9X Magnification	75
39.	Scanning Reflection Topograph of Thick (111) DyGdGaG Wafer; Boule E, $CuK\alpha_1$ Radiation, (888) Reflection, 4.9X Magnification	76
40.	Scanning Reflection Topograph of Thick (111) GdGaG Wafer; Boule B, $FeK\alpha_1$ Radiation, (444) Reflection, 4.9X Magnification	76
41.	Scanning Asymmetric Reflection Topograph of Wafer shown in Figure 40; $FeK\alpha_1$ Radiation, (480) Reflection, 4.4X Magnification	77
42.	Double-Crystal Diffractometer (Specimen is rotated around axis normal to plane of paper)	78
43.	Asymmetric Reflection Topography	79
44.	Double-Crystal Asymmetric Reflection Topographs of YIG Film on GdGaG Substrate; $FeK\alpha$ Radiation, (480) Reflection, 2.1X Magnification	80
45.	Double-Crystal Asymmetric Reflection Topograph of Substrate Underlying Film of Figure 44; $FeK\alpha$ Radiation, (480) Reflection, 2.1X Magnification	82
46.	Double-Crystal Asymmetric Reflection Topographs of GaYGdIG Film on GdGaG Substrate; $FeK\alpha$ Radiation, (480) Reflection, 2.1X Magnification	83
47.	Optical Transmission Spectrum of a Magnetic Garnet Film on a Nonmagnetic Garnet Substrate	86
48.	Magnetic Domain Pattern in (111) GdIG/GdGaG (~200X Magnification).	89
49.	Domain Pattern of (111) GdIG/SmGaG (~200X Magnification)	91
50.	Domain Pattern in Low-Coercivity Region of (111) GdIG/NdGdGaG (~200X Magnification)	91
51.	Nearly In-Plane Domains in (111) YGdIG/SmGaG (~200X Magnification)	92
52.	Smooth Serpentine Domains in Sample 2558, (111) GaYGdIG/GdGaG (~200X Magnification)	95
53.	Zero-Field Domain Pattern in Sample 2614Z3 (111) GaYGdIG/GdGaG (~200X Magnification)	95

Figure		Page
54.	Magnetic Domain Pattern as a Function of Bias Field in GaYGdIG Film	96
55.	Temperature Dependence of Domain Diameter in Epitaxial GaYGdIG - Sample 2614Z3 under Constant Bias Field	97
56.	Y-Bar Propagation Pattern	110
57.	An Imperfection in a Bubble Domain Film/Substrate Combination	117
58.	Effect of Imperfection on Magnetic-Domain Patterns	118

TABLES

Table		Page
I.	Anisotropy Fields Perpendicular to the Plane of an Epitaxial Magnetic Film	9
II.	Normalized Anisotropy Field for Magnetic Garnets	9
III.	Crystal Growth Summary	26
IV.	Properties of Selected Rare-Earth Gallium Garnets	28
V.	GaYGdIG Deposition Conditions	39
VI.	YIG Deposition Conditions	43
VII.	YGdIG Deposition Conditions	44
VIII.	Estimated Compositions of $Y_{3-z}Gd_zGa_xFe_{5-x}O_{12}$ Films	48
IX.	Deposition Conditions, AG-2, Run 2611, August 18, 1971	49
X.	Deposition Conditions, AG-2, Run 2612, August 18, 1971	50
XI.	Deposition Conditions, AG-2, Run 2613, August 19, 1971	51
XII.	Deposition Conditions, AG-2, Run 2614, August 19, 1971	52
XIII.	Bubble-Domain Film Parameters	55
XIV.	Thermal Expansion Data for $Sm_3Ga_5O_{12}$	60
XV.	Thermal Expansion Data for $Gd_3Ga_5O_{12}$	60
XVI.	Thermal Expansion Data for $Sm_{0.48}Gd_{2.52}Ga_5O_{12}$	61
XVII.	Thermal Expansion Data for $Sm_{1.88}Gd_{1.12}Ga_5O_{12}$	61
XVIII.	Thermal Expansion Data for $Nd_{1.76}Gd_{1.24}Ga_5O_{12}$	62
XIX.	Thermal Expansion Data for $Nd_3Ga_5O_{12}$	62
XX.	Thermal Expansion Data for $Sm_3Ga_5O_{12}$ (# 2)	63
XXI.	Average Thermal Expansion Coefficients	63
XXII.	Lattice Matching and Crazing Data for GaYGdIG/GdGaG	85
XXIII.	Lattice Constants of Substrates and End Members of Film Compositions	88
XXIV.	Comparison of Lattice Constant Mismatch for GdIG on Various Gallium Garnet Substrates	90
XXV.	Characteristics of Typical Epitaxial GaYGdIG Films	98
XXVI.	Parameters of an Epitaxial {111} Film of $Y_{3-z}Gd_zGa_xFe_{5-x}O_{12}$ on $Gd_3Ga_5O_{12}$	108
XXVII.	A Comparison Between CVD Bubble Garnet Films	112

INVESTIGATION OF SINGLE-CRYSTAL FERRITE THIN FILM

By J. E. Mee, P. J. Besser, P. E. Elkins
H. L. Glass, and E. C. Whitcomb

1.0 SUMMARY

The objective of the program described in this report was: (1) to develop, characterize, and optimize materials suitable for use in magnetic bubble-domain memories for aerospace applications, and (2) to develop practical techniques for the preparation of such materials in forms required for fabrication of computer memory devices. Specifically, the materials studied were epitaxial films of different compositions of the gallium-substituted yttrium gadolinium iron garnet ($Y_{3-z}Gd_zFe_{5-x}Ga_xO_{12}$) system. The present program is a continuation of a contract started in February 1967 with the NASA Electronics Research Center (ERC) in Cambridge, Massachusetts. With the closing of NASA-ERC June 30, 1970, the contract was transferred to the NASA-Langley Research Center. The program has concentrated on bubble domain garnets since April 1970.

The earlier work (1967-1970) was devoted to the growth and characterization of single-crystal thin films of ferromagnetic oxides. Such films are of interest from both a materials and a device standpoint. The method of growth was chemical vapor deposition (CVD) onto single-crystal nonmagnetic substrates. The materials studied were lithium ferrite on magnesium oxide ($LiFe_5O_8/MgO$) and gadolinium iron garnet (GdIG) on gadolinium gallium garnet ($Gd_3Fe_5O_{12}/Gd_3Ga_5O_{12}$). The interest in lithium ferrite arises from its useful properties for both microwave and memory applications while the interest in gadolinium iron garnet is mainly for memory applications. The approach and progress in this area during the first 3 years of the program are covered in the Interim Report dated February 1970 (ref. 1). In particular, that report has a complete account of the epitaxial lithium ferrite work. We are aware of only one other brief reference (ref. 2) about epitaxial lithium ferrite films grown by a close-space chemical vapor deposition method. On the other hand, more recent work on epitaxial garnets explains some of the cracking in the GdIG films mentioned in that report. These results are discussed in the present report.

In the present bubble-material phase of this program we grew and investigated epitaxial films of the $Y_{3-z}Gd_zGa_xFe_{5-x}O_{12}$ composition system. The major emphasis was to determine their bubble properties and to determine the necessary conditions for growing uncracked, high-quality films.

This final report has been assigned Autonetics Research and Technology Division Report No. C71-973/501.

2.0 INTRODUCTION

2.1 History of Fabrication of Epitaxial Garnets

The bubble-domain materials developed on this program were certain epitaxial garnets prepared by the chemical vapor deposition (CVD) process first developed in this laboratory for growing yttrium iron garnet (YIG) films (refs. 3 and 4). The CVD growth of epitaxial ferrites and garnets has been discussed at some length by Mee, et al (ref. 5). The first YIG films were cracked, had poor quality and were difficult to reproduce. As the process was improved and better substrates became available, high-quality YIG films were produced routinely. Evidence for the quality came from ferromagnetic resonance studies (refs. 5, 6 and 7), and from the performance of YIG films as acoustic shear-wave generators (ref. 8), disk filters (refs. 9 and 10) and magnetostatic surface wave devices (refs. 11 to 14). Resonance linewidths of 0.6 to 0.8 oersted (Oe) (ref. 6) at 9.1 GHz are now routinely observed on disk-shaped YIG samples produced by photolithographic etching techniques.

The CVD process used to grow epitaxial YIG obviously was applicable to the growth of epitaxial rare-earth iron garnets. A few epitaxial gadolinium iron-garnet (GdIG) films were grown in this laboratory in March 1967, to prove the feasibility and similarity to the YIG depositions (ref. 3). We returned to the GdIG depositions on this contract in late 1969. This work is reported in the Interim Report dated February 1970 (ref. 1). Also see Section 4.2.5 in this report for further comments on epitaxial GdIG. Stein (refs. 15 to 17) has also performed work on CVD GdIG. Epitaxial GdIG films have also been prepared by rf sputtering (refs. 18 and 19), but their properties are generally inferior to CVD GdIG films.

In April 1970, on another program, Autonetics grew the first known epitaxial material that had tiny mobile* bubble domains. The material was a gallium substituted yttrium iron garnet (GaYIG). The first announcement on this breakthrough was in May 1970 (ref. 20). A brief account appeared in Applied Physics Letters (ref. 21), and a more complete account was given in November 1970, at the 16th Annual Conference on Magnetism and Magnetic Materials (ref. 22).

Previous to the GaYIG work, other epitaxial materials—including epitaxial GdIG films (grown on this program), epitaxial yttrium orthoferrite ($YFeO_3$) and gadolinium orthoferrite ($GdFeO_3$)—had displayed single-wall and bubble domains but the domains were not mobile, having high wall coercivities (10 to 100 oe). The orthoferrite work is summarized in ref. 23.

*The domain wall coercivity was low enough so that wall motion could be produced by fields of a few oersteds.

Following the demonstration of highly mobile bubbles in epitaxial GaYIG there has been a great surge of activity in epitaxial bubble garnets. In this laboratory we have continued the CVD work and have been investigating different film and substrate compositions. Generally there were two major objectives:

(1) To investigate several theoretically promising film compositions to determine their bubble properties and to determine any unique problems or advantages in their fabrication.

(2) To determine the necessary film/substrate matching conditions for growing uncracked, high-quality films of each film composition. A corollary of this was to determine if there was a model or basis for film/substrate matching that would apply to all or most epitaxial garnet compositions.

On this program we investigated the $Y_{3-z}Gd_zFe_{5-x}Ga_xO_{12}$ composition system. On other programs we have been investigating $Er_3Fe_{5-x}Ga_xO_{12}$ (ref. 24) and continuing work on GaYIG (ref. 25). There is a short discussion of the relative merits of these materials in Section 6.0, Conclusions. Each of these has sufficiently good properties that bubbles have been successfully propagated using permalloy overlay Y-bar propagation tracks.

The second objective also has been met with these materials and a successful model for film/substrate matching has been formulated. This is discussed in paragraph 5.3 and in the Appendix.

Robinson et al (ref. 26) have also reported the CVD growth of epitaxial $Tb_{3-z}Er_zFe_5O_{12}$ films.

Meanwhile epitaxial bubble garnets have also been achieved by a liquid-phase epitaxy (LPE) method (ref. 27). The first films were not high quality but there has been rapid advancement so that claims have recently been made that very good quality material has been obtained by LPE (ref. 28 and 29).

At this time it appears that the CVD and LPE methods are quite competitive. Either or both techniques are being examined in various labs to determine their eventual adaptability to bubble material production.

Whichever technique is used it is apparent that epitaxial garnets are almost universally accepted as superior bubble materials.

2.2 Report Organization

In the remainder of this report there is first a review of bubbles and garnets. Then the work performed on this program is presented in Sections 4.0, Materials Fabrication; and 5.0, Materials Characterization. Finally, Section 6.0, Conclusions, summarizes the accomplishments of the program, discusses the results in terms of the present bubble material technology, and includes some suggestions for future work.

In addition, there is an Appendix on "A Stress Model for Heteroepitaxial Magnetic Oxide Films Grown by Chemical Vapor Deposition." As will be shown, this is included because of its importance not only to this program but to all bubble-garnet films grown by CVD or LPE. It was written by P. J. Besser, J. E. Mee, P. E. Elkins, and D. M. Heinz.

There are some redundancies in the report because it is difficult to separate material fabrication from material characterization. For example, the stress model is discussed or referred to in several different portions of the report. Similarly, some characterization is cited in the fabrication section as well as in the characterization section. This was deliberately done where it was believed to be necessary for a thorough explanation of some aspect of the work or for reinforcement of major points.

3.0 REVIEW OF MAGNETIC BUBBLE DOMAINS AND GARNETS

Although domain structures in single crystalline magnetic oxides have been studied extensively for many years, recent reports on the device potential of mobile magnetic domains (refs. 30 and 31) have aroused renewed interest. Under certain conditions, magnetic domains in thin plates of some magnetic oxides have the shape of right circular cylinders with the axis of the cylinder perpendicular to the surface of the plate. When observed by the Faraday effect (ref. 32) and viewed end-on, these microscopic domains appear circular, like bubbles, so that the descriptive term "bubble domain" is commonly used. The controlled movement of these small cylindrical or bubble domains holds forth the potential for a new family of magnetic devices.

The materials in which bubble domains can be formed are magnetically uniaxial, that is, they possess a unique easy axis of magnetization. If this easy axis is perpendicular to the plane of a thin plate of a material having the proper characteristics, a magnetic domain pattern such as that shown in figure 1a is observed. Such a domain pattern will usually contain a number of single-walled domains. These are domains in which the wall bounding the domain closes upon itself. Several such domains are present in figure 1a. If a magnetic bias field of suitable magnitude is applied normal to the plane of the plate, the single-walled strip domains contract into cylinders or "bubbles" as shown in figure 1b.

The bubble domains are only stable for a certain range of values of the applied field. If the bias is increased beyond the value given for figure 1b, the bubbles will shrink and eventually collapse. If the bias is reduced from the value shown, the domains expand until eventually the bubbles run out into the serpentine strip domains. The ratio of the runout diameter to the collapse diameter is approximately three to one. This diameter change occurs in a field range of ~10 to ~30 oe, depending on the particular material.

The materials in which bubble domains were first reported and studied were mainly the rare-earth orthoferrites, $RFeO_3$, where R is a rare-earth element or yttrium (refs. 33 and 34). Although the feasibility of bubble-domain devices was demonstrated with the orthoferrites and much device technology was developed on them, they had a number of significant limitations. The most serious disadvantages of the orthoferrite were the large bubble sizes (30 to 100 μm diameters) and the high temperature sensitivity of the domain size. It is also difficult to prepare single crystal samples of these materials with suitably large defect-free areas.

Hexagonal ferrites were also investigated (ref. 35) but were found to have very low domain mobilities and so very little additional work has been done on them.

A breakthrough in the bubble-domain materials area occurred in 1970 with the reports from Bell Telephone Laboratories (ref. 36) and Autonetics (refs. 20 to 22) that magnetic garnets could be made sufficiently uniaxial to support bubble domains. The work at Bell Labs was on bulk garnets grown by a flux technique while that at

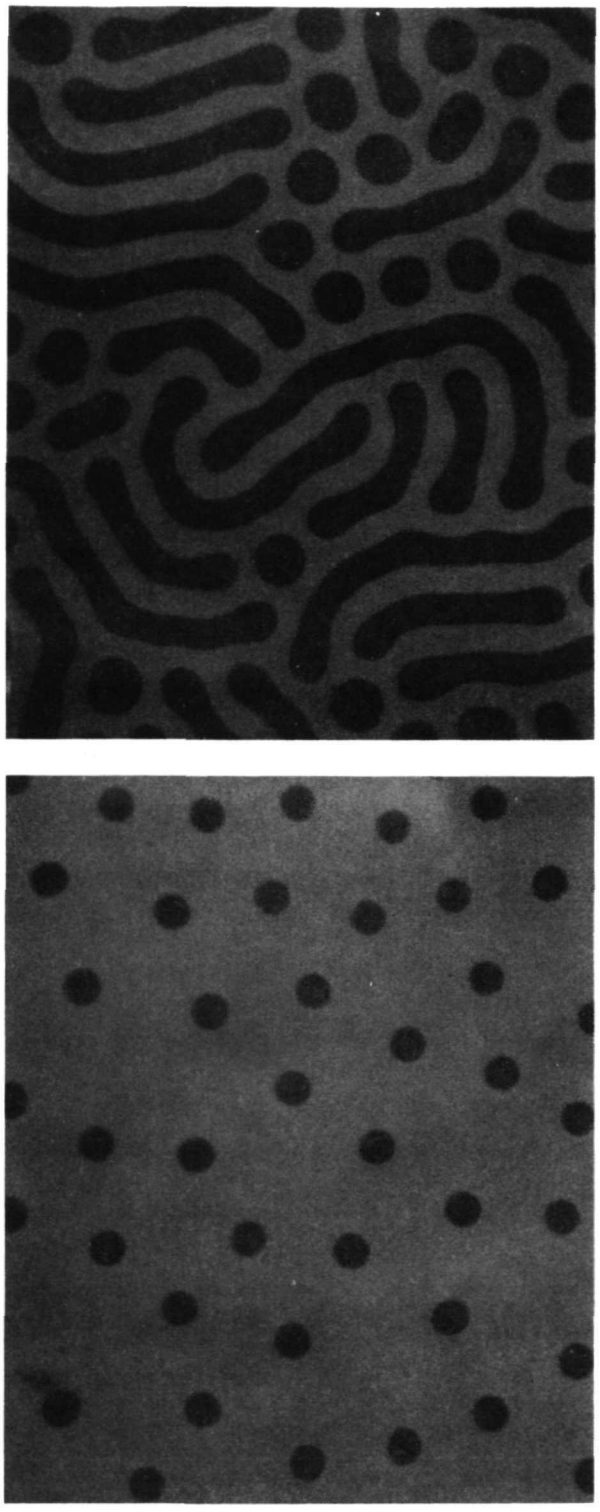

Figure 1. – Magnetic Domain Patterns in a Uniaxial Material Viewed Along the Easy Axis by the Faraday Effect

Autonetics was on thin-film epitaxial garnets grown by CVD. The mechanisms producing the uniaxial anisotropy are different for the two techniques and will be discussed in a later section. The fundamental difference is that the noncubic anisotropy is stress-induced in CVD films and growth-induced in the bulk crystals.

Subsequently a different technique for epitaxial garnet film growth, liquid phase epitaxy (LPE), was reported by workers at Bell Labs (refs. 27 to 29). In the general case the anisotropy in the LPE films results from a combination of growth-induced and stress-induced effects. It appears evident now that epitaxial thin-film garnets are presently the best available solution to the bubble-domain material requirements. It is pertinent therefore to review briefly the requirements for useful bubble-domain materials and discuss how epitaxial garnets meet these requirements.

3.1 Material Requirements for Bubble Domains

In order for magnetic bubble domains to be useful, they must be of suitable size, have a high mobility, and be relatively insensitive to temperature excursions about the operating temperature. Attainment of these properties depends on the relative and absolute values of certain material parameters. It is also essential that the defect density in the material be low (≤ 5 cm^{-2}).

3.1.1 Requirements for the existence of bubble domains. - In a thin plate of magnetic material, with a magnetization of $4\pi M$ and an effective uniaxial anisotropy K_u (producing an easy direction of magnetization perpendicular to the plate), the anisotropy field along the easy direction is defined as $H_A = 2K_u/M$. A general requirement for the existence of cylindrical domains with axes perpendicular to the plate is that $K_u > 2\pi M^2$ (ref. 37). An alternative form of this requirement is that the normalized anisotropy field $\overline{H}_A > 1$, where $\overline{H}_A = H_A/4\pi M = K_u/2\pi M^2$ is the anisotropy field measured in units of $4\pi M$.

Thiele's theory (ref. 37) is strictly valid only for infinite $\overline{H}_A$ but recent theoretical work (ref. 81) indicates the static stability range for bubble domains is almost constant for $\overline{H}_A > 1.5$. Since the domain mobility decreases as $\overline{H}_A$ increases, preferred values of $\overline{H}_A$ are in the range of 2 to 5.

The normal source of the uniaxial anisotropy observed in magnetic materials is the crystal structure of the material. If this structure is conducive to a unique axis of magnetization, as in the hexagonal ferrites and the orthoferrites, the magnitude of the anisotropy constant is very large: e.g., $K_u \sim 10^6$ ergs/cc, for hexagonal ferrites (ref. 38) and $\sim 10^5$ ergs/cc for orthoferrites (ref. 39). The basic structure of the nonmagnetic garnets is cubic but since no material possessing a spontaneous magnetization can be strictly cubic (ref. 40), the magnetic garnets should have a distortion from the cubic structure. However, until the recent observations of Bertaut on terbium iron garnet (ref. 41), no such distortion has been detected by diffraction techniques.

Observations of uniaxial anisotropy in magnetic garnets have been attributed to two types of phenomena. In one type, the effect is produced by the growth process and is attributed to a pair ordering or site preference of the rare-earth ions in the garnet structure (refs. 42 to 44). This growth-induced anisotropy is found in both the bulk garnets and the LPE films.

Other investigators have attributed uniaxial anisotropy in bulk garnets to magnetostriction as a result of stress induced by mechanical polishing (refs. 32, 45, and 46). The dominant source of the uniaxial anisotropy observed in magnetic oxide films formed by chemical vapor deposition (CVD) onto nonmagnetic substrates at elevated temperatures is magnetostriction (refs. 47, 5 and 22). The effect of magnetostriction on anisotropy and bubble-domain formation in epitaxial films is summarized below:

> Epitaxial magnetic films are normally in a state of mechanical stress, σ, due to a mismatch between lattice constants and thermal expansions of the film and substrate (ref. 48). If the film is magnetostrictive, this stress produces a uniaxial magnetic anisotropy that is superimposed on the bulk, unstrained anisotropy. For a material with negative magnetostriction constants (λ_{100}, $\lambda_{111} < 0$), the magnetostrictive contribution tends to make the normal-to-the-film plane an easy axis if the film is in tension ($\sigma > 0$), and a hard axis if the film is in compression ($\sigma < 0$).
>
> The magnetostrictive effect can therefore be used to provide a uniaxial magnetic anisotropy in materials whose crystal structure is nearly cubic.
>
> Values for the effective anisotropy field perpendicular to the film plane can be derived by including the magnetostrictive contribution into the normal expression for the cubic anisotropy energy (refs. 5 and 22). These values are listed in table I for the three principal crystallographic orientations. Here K_1 is the usual first-order cubic anisotropy constant and K_2 is assumed to be zero. The dependence of H_A on the plane of rotation of M for the $\{110\}$ case results because H_A is a function of the azimuthal angle about the film normal as well as the polar angle θ. Thus the stress induced anisotropy is uniaxial for the $\{100\}$ and $\{111\}$ orientations but is orthorhombic for the $\{110\}$.
>
> Consider the case of a material with K_1, λ_{111}, and λ_{100} negative; e.g., yttrium iron garnet (YIG). If the film is in tension the magnetostrictive contribution to H_A is positive for all orientations; i.e., the easy axis is perpendicular to the film plane, as noted previously. For $\{100\}$ films the cubic contribution to H_A is negative and $\sigma\lambda_{100}$ must be larger than about $2K_1/3M$ in order to establish an easy axis perpendicular to the film. However, for a $\{111\}$ deposit the two contributions are both positive and this orientation is the most favorable.
>
> The $\{110\}$ situation is more complicated but a uniaxial domination can be achieved by magnetostrictive contributions that are smaller than in the $\{100\}$ case.
>
> Using literature values of the material parameters and assuming a value of 4×10^9 dynes/cm^2 for σ, one can then tabulate values of $\overline{H}_A$ to compare various materials with regard to their potential as bubble candidates. Such a comparison is made in table II.
>
> The negative $\overline{H}_A$ values for the $\{100\}$ films of gadolinium iron garnet (GdIG) and mixed yttrium-gadolinium iron garnets (YGdIG) indicate that the easy axis is not normal to the film. The $\overline{H}_A$ values less than unity show that these materials and/or orientations cannot support stable bubble domains;

TABLE I. – ANISOTROPY FIELDS PERPENDICULAR TO THE PLANE OF AN EPITAXIAL MAGNETIC FILM

Film Plane	H_A [a]	
{100}	$\frac{2K_1 - 3\sigma\lambda_{100}}{M}$	
{110}	$\frac{2K_1 - 3\sigma(\lambda_{100} + \lambda_{111})}{2M}$	M rotates in {110}
	$\frac{-2K_1 - 3\sigma\lambda_{111}}{M}$	M rotates in {100}
{111}	$\frac{-4K_1 - 9\sigma\lambda_{111}}{3M}$	

[a] Certain errors are present in the H_A values given in ref. 5. The values in this table are the corrected ones.

TABLE II. — NORMALIZED ANISOTROPY FIELD FOR MAGNETIC GARNETS

Material	$\overline{H}_A$		
	{100}	{110}	{111}
$Y_3Fe_5O_{12}$	0.01	0.1 in {100} and {110}	0.1
$Gd_3Fe_5O_{12}$	-100	94 {110}; 375 {100}	340
$Y_{1.5}Gd_{1.5}Fe_5O_{12}$	-0.05	0.2 {110}; 0.6 {100}	0.6
$Y_{0.6}Gd_{2.4}Fe_5O_{12}$	-0.5	0.8 {110}; 2.8 {100}	2.5
$Dy_{2.1}Tb_{0.9}Fe_5O_{12}$	10.6	5.6 {110}; 1.7 {100}	1.3
$Y_3Ga_{0.64}Fe_{4.36}O_{12}$	0.14	0.32 {110}; 0.48 {100}	0.44
$Y_3Ga_{1.1}Fe_{3.9}O_{12}$	0.8	3.4 {110}; 7.9 {100}	7.2
$Y_{2.4}Gd_{0.6}Ga_{1.0}Fe_{4.0}O_{12}$	1.7	3.8 {110}; 7.2 {100}	6.8

whereas bubbles should exist in cases where $\overline{H}_A > 1$ such as {110} and {111} $Y_3Ga_{1.1}Fe_{3.9}O_{12}$ and all three orientations of $Y_{2.4}Gd_{0.6}Ga_{1.0}Fe_{4.0}O_{12}$.

To summarize, the conditions for bubble-domain formation can be achieved readily in epitaxial garnets by using the inherent magnetostrictive anisotropy and lowering the magnetization by substitution or mixing.

3.1.2 Requirements for desirable bubble diameters. - For device work, the domain diameter should be small in order to attain high concentrations of bubbles in a wafer. However, very small bubbles present a problem in manipulation due to the limits of resolution of the photolithographic techniques employed in defining the metal patterns used for domain propagation. Thus bubbles between five and eight μm are of optimum size since, when separated by three domain diameters to minimize repulsion between bubbles, they yield densities of the order of a million bits per square inch.

It is convenient to discuss the domain diameter in terms of an effective length, ℓ, which is defined as $\ell = (AK_u)^{1/2}/\pi M^2$ where A is the exchange constant of the material. Thiele (ref. 37) has shown that the bubble-domain characteristics are optimized for a plate thickness of 4ℓ. In a plate of this thickness, a domain diameter, d_o, of 8ℓ is at the center of the stability range, which represents a desirable point for device operation. Both $4\pi M$ and K_u may be expressed in terms of this preferred domain diameter as $4\pi M = 32\,(2\pi A\overline{H}_A)^{1/2}/d_o$ and $K_u = 256A\overline{H}_A{}^2/d_o{}^2$. The value of the exchange constant, A, does not vary appreciably in bubble materials, typically being 2×10^{-7} ergs/cm in the garnets. Using this value of A, $\overline{H}_A = 4$ and $d_o = 5$ μm, the corresponding values are $4\pi M \approx 150$ gauss and $K_u \approx 3200$ ergs/cm^3. Magnetization and anisotropy of this magnitude are readily attained in garnet materials. It can be seen that materials of lower magnetization and higher anisotropy such as orthoferrites, will have larger bubble diameters while those with higher magnetizations, such as the unsubstituted hexagonal ferrites, will have smaller bubble diameters.

3.1.3 Requirements for highly mobile bubble domains. - Rapid motion of a bubble domain requires a large value of the domain wall mobility, μ_w, which may be expressed as $\mu_w = |\gamma|\,\ell/2\,\overline{H}_A$ where γ is the gyromagnetic ratio, and α is the ferromagnetic damping parameter. The conceptual basis and defining expressions for μ_w are presented in paragraph 5.15 and an excellent discussion of wall motion in bubble domain materials is given in ref 82.

Since the mobility is inversely proportional to $\overline{H}_A$, it is desirable to have a relatively small $\overline{H}_A$ for high mobility. As a practical matter, the most favorable circumstance is to have $\overline{H}_A$ values of two to five so that the bubble domains are stable and at the same time highly mobile.

The wall mobility is directly proportional to the characteristic length, which means that a large domain diameter is desirable for high mobility. Device requirements, however, limit d to the range of 5 to 8 μm, which corresponds to ℓ values between 0.6 and 1.0 μm. Thus both ℓ and $\overline{H}_A$ may only be varied over a rather limited range.

By adjusting the temperature and/or the composition of ferrimagnetic materials such as the iron garnets, $|\gamma|$ can be made quite large. However, the conditions which result in a large $|\gamma|$ also produce a corresponding increase in α so that the ratio $\frac{|\gamma|}{\alpha}$ (and consequently μ_w) is not much affected by changes in $|\gamma|$ (ref. 82).

The damping parameter, α, can produce significant variations in μ_w. This parameter is a measure of the material losses associated with the motion of the magnetization. Since this damping constant is proportional to the ferromagnetic resonance (FMR) linewidth (ΔH) of the material, the relative magnitudes of α in various materials can be obtained from ΔH values. Experimentally it has been found that iron garnets containing ions such as Y^{3+}, Gd^{3+}, Eu^{3+}, Tm^{3+} and Yb^{3+} have relatively small damping constants while those with Er^{3+}, Nd^{3+}, Pr^{3+}, Sm^{3+}, Dy^{3+}, Ho^{3+} and Tb^{3+} have large damping constants. The reasons for these differences are reasonably well understood on a theoretical basis but it is beyond the scope of this report to present a detailed discussion of these concepts. A summary of experimental results and theoretical models of ferromagnetic damping in garnets is contained in ref. 83, p. 106-114; ref. 84, p. 222-228; and ref. 85, p. 574-576. The influence of the damping constant on wall motion in bubble materials is discussed in Hagedorn's paper (ref. 82) and its references.

In addition to the intrinsic losses, imperfections in the material can provide large magnetic losses so that good crystal quality is essential to high mobility.

Therefore, it is anticipated that high quality iron garnets containing only Gd^{3+}, Eu^{3+}, Y^{3+}, Tm^{3+}, Yb^{3+}, or combinations thereof will have high domain wall mobility.

3.1.4 Requirements for temperature stability. - Temperature stability is very desirable for any device. However, material parameters are temperature sensitive and they thereby bound the useful operating temperature range. Of prime concern in bubble-domain devices is the stability of the domain diameter since a metal pattern used for bubble manipulation has a specific spacing that will function properly only for a limited range of domain diameters.

The equilibrium domain diameter, d, will change with temperature since $d \sim (K_u)^{1/2}/M^2$; and both of these parameters are temperature dependent. In the vicinity of certain critical points such as: (1) the Neel temperature, T_N, or (2) the magnetization compensation temperature, T_{comp}, these material parameters exhibit large temperature sensitivity. (See para 3.2.1 and 3.2.2.) To minimize the temperature dependence of the domain diameter, the operating temperature range should not be close to these critical points.

At temperatures well removed from T_N and T_{comp} it is anticipated that the main cause for a change in the domain diameter will be the temperature dependence of the magnetization. This is so because the domain diameter varies as the square of the magnetization but only as the square root of the uniaxial anisotropy.

The domain diameter can therefore be stable over an extended temperature range if the material has a magnetization characteristic which is rather flat as a function of temperature. The approximate requirement on the sign and magnitude of $d(4\pi M)/dT$ is derived in paragraph 5.8.

3.1.5 Summary of material requirements. - The requirements for a useful bubble-domain layer are a composite of magnetic properties, dimensional characteristics, and single-crystalline quality: (1) primarily, the material must possess a uniaxial magnetic anisotropy; (2) the magnitude and ratio of this anisotropy and the magnetization must be within suitable numerical ranges to produce bubble domains of a useful size; (3) the magnetic easy direction must be perpendicular to the layer surface; (4) the layer should be thin and preferably of dimensions comparable to the domain diameter; (5) there should be a minimum of imperfections so that bubble-domain motion is not impeded, which implies good crystalline quality and smooth layer surfaces;

(6) the layer should be unvarying in properties and thickness so that bubble-domain behavior is uniform across the material; (7) the layer should be extensive enough to accommodate a large number of bubble domains; (8) the bubble domains should have a small temperature sensitivity; and (9) the bubble domains should have a high mobility to provide a high data rate.

Good reviews of the bubble-domain material requirements are presented in the papers by Gianola, et al (ref. 33) and Nielsen (ref. 34).

3.2 Properties of Magnetic Garnets

The term garnet is used to describe compounds that have the garnet crystal structure. The stoichiometry of a garnet and the lattice positions of elements in a garnet may be expressed by the formula $\{R\}_3[S]_2(T)_3O_{12}$ where { } represents dodecahedral or (c) sites, [ ] represents octahedral (a) sites, and ( ) represents tetrahedral (d) sites.* The garnet structure is cubic with eight formula units per unit cell so that it contains 24 c sites, 16 a sites and 24 d sites. The c sites are occupied by large ions R, the d sites are occupied by small ions T, and the a sites are occupied by small or medium ions S. Garnets can be either magnetic or nonmagnetic depending upon the type of ions on the a and d sites. If these sites are occupied by nonmagnetic ions such as Al^{3+} or Ga^{3+}, the nonmagnetic garnets result.

When the ferric ion, Fe^{3+}, fills the a and d sites, the magnetic iron garnets are obtained. It has become customary to use a shorthand notation in place of the name or full chemical formula for the various garnets. Thus, for example, yttrium aluminum garnet ($Y_3Al_5O_{12}$), gadolinium gallium garnet ($Gd_3Ga_5O_{12}$) and erbium iron garnet ($Er_3Fe_5O_{12}$) are abbreviated as YAG, GdGaG and ErIG, respectively. Similar notation is used for other members of the garnet system. Gallium substituted yttrium iron garnet ($Y_3Fe_{5-x}Ga_xO_{12}$) is called GaYIG. In this report we abbreviate gadolinium iron garnet ($Gd_3Fe_5O_{12}$), yttrium gadolinium iron garnet ($Y_{3-z}Gd_zFe_5O_{12}$), and gallium-substituted yttrium gadolinium iron garnet ($Y_{3-z}Gd_zFe_{5-x}Ga_xO_{12}$) as GdIG, YGdIG, and GaYGdIG respectively.

In the lattice of a pure rare-earth iron garnet, the rare-earth or yttrium ions enter the 24 c sites and the ferric ions fill the 16 a and 24 d sites. The array of magnetic ions on each type of site is referred to as a sublattice. Very strong interaction between the ferric ions induces a parallel alignment of the magnetic moments of all of the ions within each sublattice, with the a and d sublattices in antiparallel alignment with one another. Since there are two octahedral and three tetrahedral ferric ions per formula unit, there will be a net magnetic moment equivalent to one ferric ion per formula unit from these two sublattices. If the rare-earth ion is nonmagnetic (Y^{3+}, La^{3+}, Lu^{3+}), there is no further magnetic contribution. Other rare-earth ions have their magnetic moments aligned by weaker interactions than the ferric ion sublattices. In all of the pure rare-earth iron garnets except that of samarium, the magnetization of the rare-earth ion sublattice is aligned antiparallel to the net ferric ion moment as indicated schematically in figure 2.

*The designation of "c," "a," and "d" sites comes from an arbitrary use of these letters in a systematic tabulation in the "Crystal Structure Tables."

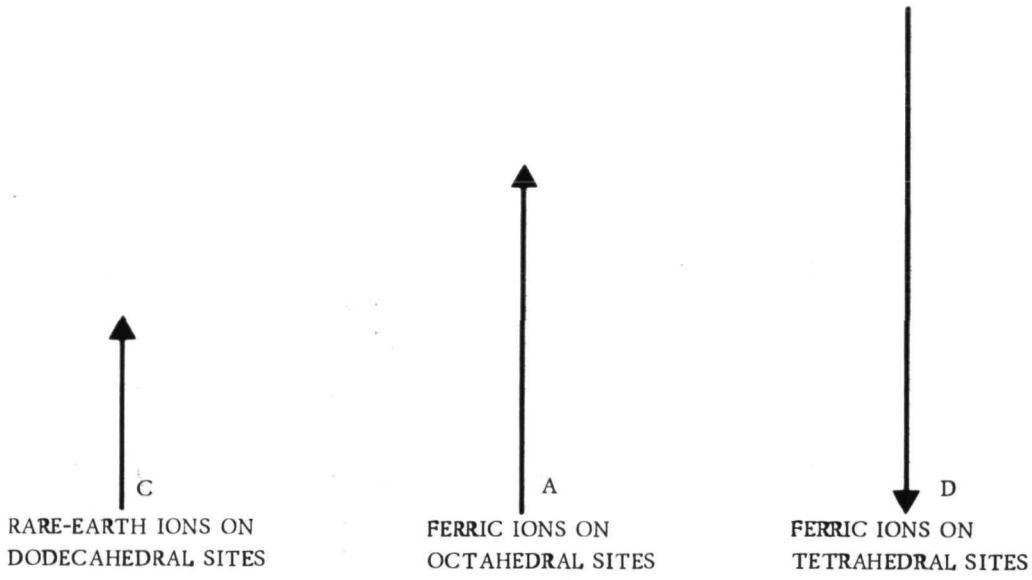

Figure 2. – Relative Orientation of Sublattice Magnetizations in Garnets

3.2.1 Effect of temperature. - In a rare-earth iron garnet, there are several factors that affect the magnetization, $4\pi M$. In some cases the rare-earth ion magnetization can exactly cancel the net ferric ion magnetization. This occurs near room temperature for GdIG and at lower temperatures for other rare-earth iron garnets. These points of zero magnetization are referred to as compensation temperatures, T_{comp}. Figure 3 shows the magnetization as a function of temperature for several magnetic garnets.

The thermal vibrations associated with increasing temperature tend to disrupt a magnetically ordered system. Each magnetic interaction is subject to this thermal weakening, and thus every sublattice magnetization will decrease with temperature, but not necessarily at the same rate. The c-sublattice magnetization, which is not very strongly aligned to begin with, decreases most rapidly with temperature. If the c-sublattice contribution is less than that of the combined a-d sublattices, the ferric-ion-moment is dominant. This is the case for YIG at all temperatures as shown in figure 3 since Y^{3+} is nonmagnetic. For garnets with magnetic rare-earth ions, the c-sublattice magnetization (which is greatest at the lowest temperatures) reduces the room-temperature garnet magnetization below that of YIG. As the temperature is raised, the rare-earth contribution diminishes more rapidly than that of the iron, and at high temperatures the saturation magnetization approaches that of YIG. Eventually, the temperature becomes high enough for a-d interaction to be overcome as well, and all magnetic garnets become paramagnetic at their Neel Temperatures, T_N.

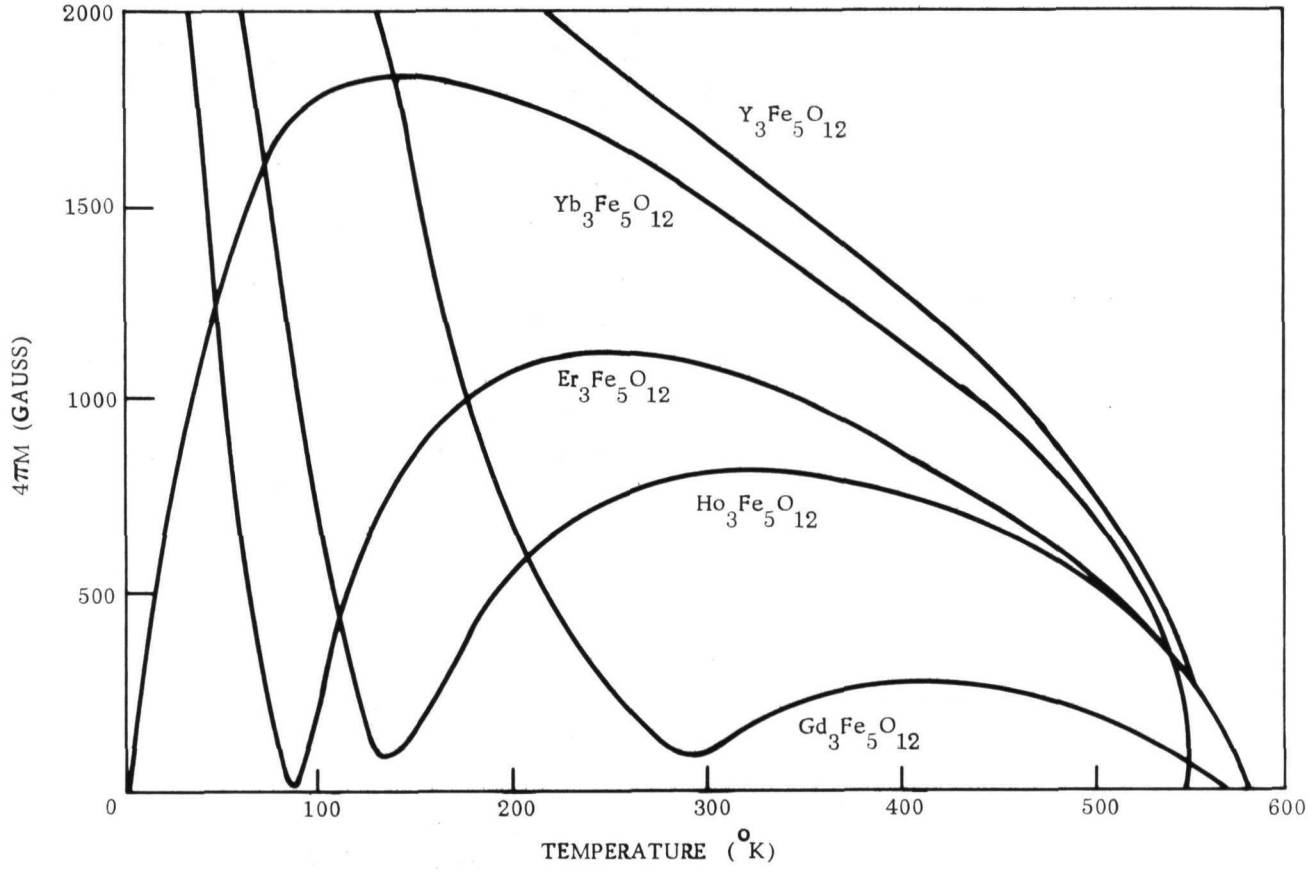

Figure 3. – Magnetization as a Function of Temperature for Several Magnetic Garnets

3.2.2 Effect of composition. - Introduction of more than one rare-earth ion into the c-sublattice yields a garnet whose c lattice magnetization M_c, is approximately equal to the weighted mean of the M_c of the two pure garnets. These are called "mixed" garnets. For example, the introduction of Gd^{3+} into YIG adds a c-sublattice magnetization that gradually reduces the low-temperature magnetization until it reaches zero and a compensation point appears. Further Gd^{3+} substitution into YIG increases T_{comp} until it approaches the value for pure GdIG.

Iron garnets in which some of the iron ions have been replaced by other ions are called substituted garnets. The substituting ion may enter either of the a- or the d-sublattices and many ions show a preference for one or the other. Thus, $A\ell^{3+}$ and Ga^{3+} tend to enter the tetrahedral d sites whereas In^{3+} and Sc^{3+} prefer the octahedral a sites. Substitution, like mixing, can greatly alter the magnetization and shift T_{comp} and T_N. But the change caused by substitution is much more pronounced than that induced by mixing, for the presence of a foreign ion in the a- or d-sublattice invariably weakens the a-d interaction and reduces T_N in proportion to the level of substitution. The net magnetization of a mixed iron garnet such as $(YGd)_3Fe_5O_{12}$ is the algebraic sum of the three sublattice magnetizations, $4\pi M_c$, $4\pi M_a$ and $4\pi M_d$ where $4\pi M_c$ represents the magnetization due to the Gd^{3+} ions on the dodecahedral (c) sites and $4\pi M_a$ and $4\pi M_d$ represent the magnetizations of the Fe^{3+} ions on the octahedral (a) and tetrahedral (d) sites respectively. In YGdIG, $4\pi M_a$ and $4\pi M_c$ are parallel to each other and antiparallel to $4\pi M_d$. The convention $4\pi M = 4\pi[(M_d - M_a - M_c)]$ will be used to define the polarity of $4\pi M$ in the $(YGd)_3Ga_xFe_{5-x}O_{12}$ system.

When gallium is substituted for part of the iron it preferentially enters the d sites and reduces the value of $4\pi M_d$ and hence, $4\pi M$. At a certain level of gallium substitution, $x = x_{comp}$, $4\pi M_d = 4\pi(M_a + M_c)$ and magnetization compensation occurs so that $4\pi M = 0$. For values of $x > x_{comp}$, $4\pi M$ becomes negative and increases in magnitude. Eventually, however, the substitution of the nonmagnetic Ga^{3+} ion reduces the magnetic interactions to such an extent that thermal energy begins to disrupt the ordered magnetic arrangement of ions on the various sublattices and $4\pi M$ again begins to decline in magnitude. Still further increase in the value of x results in the material becoming nonmagnetic at room temperature ($4\pi M = 0$, $T_N = 300°K$). This second point of zero magnetization, x_N results because each of the sublattice magnetizations goes to zero in contrast to the situation at x_{comp} where all three are finite.

A theoretical curve of the variation of $4\pi M$ with gallium content for $Y_{2.4}Gd_{0.6}Ga_xFe_{5-x}O_{12}$ is shown in figure 4. It can be seen that knowledge of $4\pi M$ is not enough to alone define the value of x since x values of A, B and C all produce the same $4\pi M$. By observing the behavior of the Faraday effect domain pattern in response to an external field and comparing this behavior with that of a known sample such as pure YIG, the polarity of $4\pi M$ can be determined in an unknown sample.

3.3 Potential Materials

The initial material requirement for bubble domains is that the material must have a uniaxial anisotropy. Although garnets are nominally materials with cubic anisotropy, it has been demonstrated that certain growth conditions produce crystals

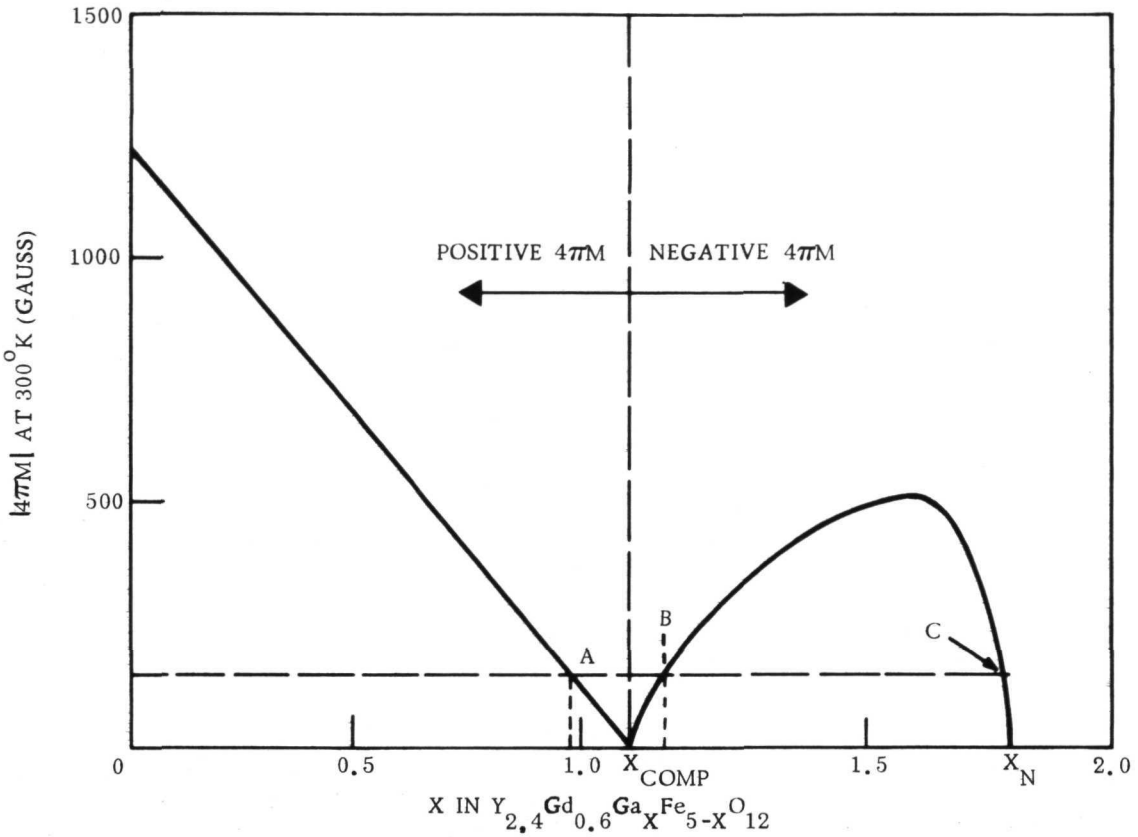

Figure 4. – Variation of Room-Temperature Magnetization with Ga Content in Yttrium-Gadolinium-Iron Garnet System

that exhibit uniaxial anisotropy. Flux-grown bulk garnets and LPE films contain regions of uniaxial anisotropy. Reported compositions that have exhibited bubble domains in bulk samples and LPE films, refs. 27, 49, and 86, are:

	Material	Growth Technique	Substrate
(1)	$Er_2Tb_1Al_{1.1}Fe_{3.9}O_{12}$	Bulk	---
(2)	$Gd_{2.34}Tb_{0.66}Fe_5O_{12}$	Bulk	---
(3)	$Gd_{0.95}Tb_{0.75}Er_{1.3}Al_{0.5}Fe_{4.5}O_{12}$	Bulk	---
(4)	$Eu_2Er_1Ga_{0.7}Fe_{4.3}O_{12}$	Bulk, LPE	GdGaG(110)
(5)	$Eu_1Er_2Ga_{0.7}Fe_{4.3}O_{12}$	LPE	GdGaG(111)
(6)	$Y_2Gd_1Al_{0.8}Fe_{4.2}O_{12}$	Bulk	---
(7)	$Y_{1.8}Eu_{0.2}Gd_{0.5}Tb_{0.5}Al_{0.6}Fe_{4.4}O_{12}$	Bulk	---
(8)	$Eu_{1.5}Gd_{1.5}Al_{0.5}Fe_{4.5}O_{12}$	Bulk	---
(9)	$Eu_{0.5}Y_{2.5}Ga_{1.0}Fe_{4.0}O_{12}$	LPE	GdGaG(111)
(10)	$Gd_{0.5}Y_{2.5}Ga_{1.0}Fe_{4.0}O_{12}$	LPE	GdGaG(111)
(11)	$Ca_2Bi_1V_1Fe_4O_{12}$	Bulk	---
(12)	$Pr_1Gd_2Ga_{0.5}Fe_{4.5}O_{12}$	Bulk	---

Garnet films grown epitaxially upon the proper crystallographic plane of a suitable substrate also exhibit a uniaxial anisotropy (refs. 5, 22, and 47). In heteroepitaxial films prepared by CVD, the uniaxial anisotropy is definitely due to magnetoelastic effects resulting in the film acting through the magnetostriction constants.

Reported bubble-domain compositions of CVD garnet films, refs. 21, 22, 26, 48, 50, and 51, are:

	Film	Substrate
(1)	$Y_3Ga_{1.2}Fe_{3.8}O_{12}$	GdGaG (111) and (110), DyGdGaG (111)
(2)	$Er_3Ga_{0.7}Fe_{4.3}O_{12}$	DyGdGaG (111) and (110)
(3)	$Y_{2.4}Gd_{0.6}Ga_{1.0}Fe_{4.0}O_{12}$	GdGaG (111)
(4)	$Tb_3Fe_5O_{12}$	SmGaG (111)
(5)	$Tb_{2.5}Er_{0.5}Fe_5O_{12}$	SmGaG (100); SmGdGaG ( )

The next material requirement is that the normalized anisotropy field be greater than one. For unsubstituted iron garnets, the magnitude of $\overline{H}_A$ is less than one except in the vicinity of T_{comp} where the magnetization is very small. However, it is undesirable to operate near T_{comp} because of the extreme temperature sensitivity in this region. A more satisfactory method for obtaining a value of $\overline{H}_A$ greater than one is to reduce the magnetization by substitution of nonmagnetic ions in tetrahedral lattice sites.

A review of the material properties of various garnet compositions suggests that rare-earth iron garnets with low-temperature compensation points such as Gd-substituted YIG hold great promise for the simultaneous achievement of reduced magnetization and temperature stability. $A\ell^{3+}$ or Ga^{3+} substitution reduces the dominant d-sublattice magnetization, thereby reducing $4\pi M$. Nonmagnetic ions substituting in the ferric ion sublattices also weaken the coupling so that T_N is lowered. In a useful material, the concentration of substituting ions should be low enough to achieve the desired magnetization while T_N remains well beyond the operating temperature range.

Finally, in order to have high mobility it is desirable to have compositions that do not contain ions with large damping factors. Therefore, mixed combinations of GdIG, EuIG, YbIG, TmIG, and YIG with Ga^{3+} or $A\ell^{3+}$ substitutions appear to be highly desirable bubble-domain material compositions. It has been found that epitaxial samples of $Y_{2.4}Gd_{0.6}Ga_{1.0}Fe_{4.0}O_{12}$ are excellent bubble-domain materials.

4.0 MATERIALS FABRICATION

4.1 Substrate Preparation

4.1.1 Introduction.– In order to obtain an adherent epitaxial film, there should be a similarity between crystal symmetries, lattice spacings, and thermal expansions of the epitaxial film and the substrate surface. A film and substrate that have the same crystal structure and close lattice constants can achieve epitaxy. Thus, nonmagnetic garnets are used as substrates for the magnetic iron garnet. The film/substrate matching requirements for epitaxial bubble garnets prepared by CVD are particularly rigorous because a certain amount of stress is required in the film to produce the uniaxial anisotropy necessary to obtain bubbles (see page 64). However, too much stress will cause film cracking. The stress model that gives the conditions for controlling the stress is given in the appendix and discussed in para 5.3 of this report. It shows that under certain conditions, i.e., when the film and substrate are closely matched in lattice constant and thermal expansion, the state of stress in an epitaxial garnet film is dependent only on the room temperature lattice mismatch between film and substrate. Thus, for a particular magnetic oxide film composition one must select a rare-earth garnet substrate with a specific lattice constant value. This is the situation encountered with the GdIG, YGdIG, and GaYGdIG films investigated on this program. The film composition, once selected, established the magnetic and elastic constants of the film as well as the film lattice constant. It was then necessary to select a suitable rare-earth garnet substrate composition to provide the required substrate lattice constant.

The rare-earth gallium garnets were selected as potential substrates because they were simple chemically and had lattice constants in the required range.

Initially, the selection of specific substrate compositions for the films was complicated by the fact that there was very little information available regarding the rare-earth gallium garnets. There were some room-temperature lattice constants reported by Geller (ref 40). These were obtained for the most part on flux-grown single crystals and sintered oxide compacts. Although we utilized this information initially, we later found that these lattice constant values were lower than the values we determined for the Czochralski-grown boules. Further, details concerning the melting points and phase relationships of the rare-earth gallium garnets, which would have been helpful for crystal growth, were virtually nonexistent. The only helpful data compiled in this area was that of Schneider, Roth and Waring (ref 52), which reported the rare-earth gallium systems that contained a garnet phase.

Initially only the single-garnet compositions were considered, namely $Gd_3Ga_5O_{12}$, $Nd_3Ga_5O_{12}$ and $Sm_3Ga_5O_{12}$. However, preliminary results with GdIG and YGdIG deposits indicated that lattice constants closer to that of the films were required. With this in mind, the growth of mixed rare-earth gallium garnet crystals was initiated. The specific composition of these first few mixed garnet compositions was arrived at by assuming that the end member, e.g., $Nd_3Ga_5O_{12}$ and $Gd_3Ga_5O_{12}$,

formed a series of solid solutions where the lattice constant of any selected composition obeyed Vegards Law (The lattice constant was linear with composition). A number of natural minerals exhibit this behavior and the solid solutions, in this case, were referred to as an isomorphous series. Based on this assumption, a number of mixed crystal compositions were grown in the $Nd_3Ga_5O_{12}/Gd_3Ga_5O_{12}$, $Nd_3Ga_5O_{12}/Sm_3Ga_5O_{12}$, and $Sm_3Ga_5O_{12}/Gd_3Ga_5O_{12}$ systems. The details related to the growth of these crystals are reported along with selected properties of several compositions in the subsequent sections.

4.1.2 Experimental. – The crystals were grown in air by the Czochralski method using the A. D. Little furnace shown in figure 5. The crucible was heated with a 25-KW Toccotron 450-kHz/4-MHz dual-frequency rf generator. A sapphire light pipe abutted the bottom of the iridium crucible and focused the radiation onto a Honeywell Radiametric sensing head that in turn provided a millivolt signal to a Leed and Northrup Speedimax H proportional control system.

The crucible setup for the growth of the crystals is illustrated in figure 6. As indicated in the figure, the crystals were pulled from the molten oxide melt into an insulated cavity. This insulated cavity served two purposes. First, it reduced the temperature gradients within the growing crystals and thus minimized cracking due to thermal stresses. Further, it restricted the flow of air currents around the crystal and minimized the loss of iridium from the crucible via the formation of the volatile IrO_2.

The starting materials were nominally 99.9-percent pure rare-earth oxide powders from Research Chemicals Co., Phoenix, Arizona; and nominally 99.9-percent pure gallium oxide (Ga_2O_3) powder from Alussisse Co., Ft. Lee, New Jersey. The powders were dried, weighed in appropriate amounts to the nearest milligram, and then mixed in a ball mill. After thorough mixing, the powders were pressed into cylindrical pellets 1.0 in. in diameter and 0.5 in. high, using a metallurgical mounting press. These pellets were then placed in the iridium crucible and melted. Usually three sequential loading and meltings were required to bring the melt level to within 0.25 in. of the crucible lip.

Slices of $Gd_3Ga_5O_{12}$ with (111) cut faces were used as seeds. The seeds were attached to a 0.125-in. diameter aluminum pull rod by putting an iridium wire through a hole in the center of the slice and then beading the wire with an O_2-H_2 torch.

The crystals were then grown in one atmosphere of air at a nominal pull rate of 0.125 in./hr and 0.25 in./hr at a rotation rate of 5 rpm. At the end of the crystal growth run the crystals were slowly and carefully separated from the melt so as to minimize thermal shock and prevent cracking of the boules. After separation from the liquid, the crystals were held about 0.125 in. above the liquid and slowly cooled to room temperature.

Initially the crystals were annealed at 1600°C in flowing oxygen or air for 10 hr, and then continuously cooled to room temperature over a period of 20 hr. This practice was discontinued after the examination of crystals and crystal slice with polarized light revealed no significant reduction in residual strains after annealing.

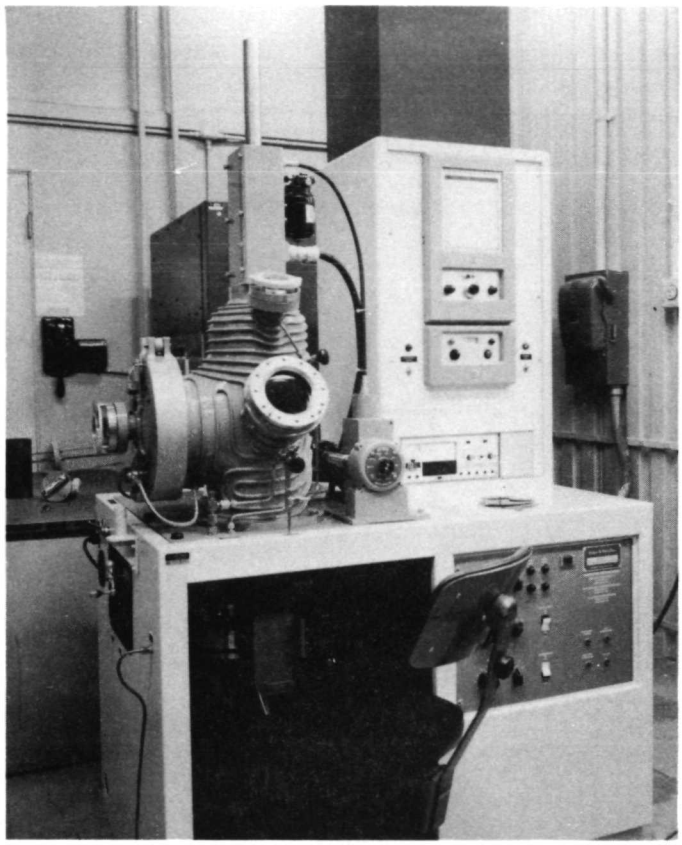

Figure 5. – A. D. Little Crystal-Growth Furnace

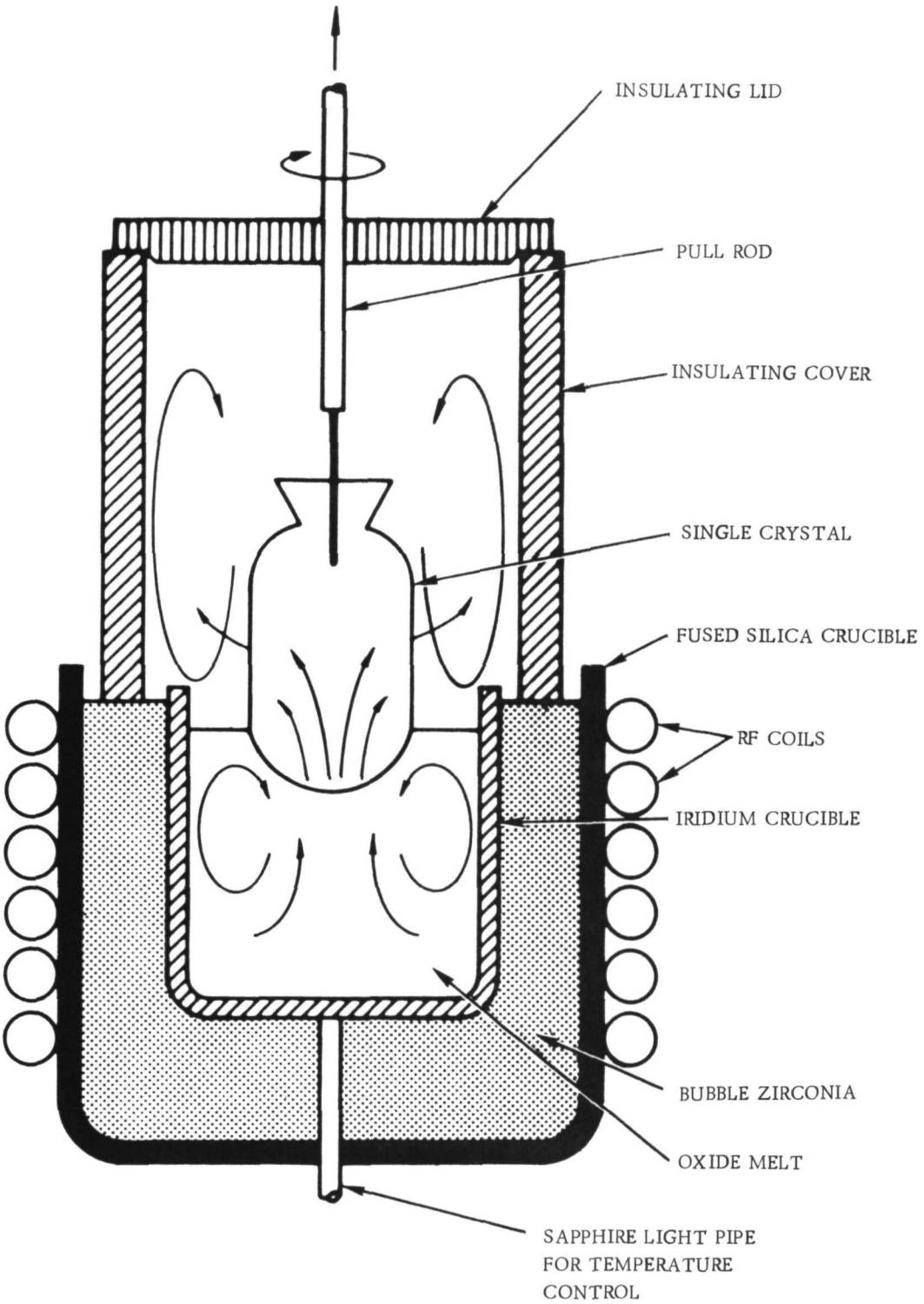

Figure 6. – Crucible Setup for the Growth of the Rare-Earth Gallium Garnets

After a visual examination, the crystals were oriented to the (111) direction and cut into substrate wafers. The thickness of these slices was nominally 0.030 in.

The preparation of the substrate surfaces involved the use of a resonant vibratory machine. This method gives reproducibility of surfaces essentially scratch-free, with minimal subsurface mechanical damage. Evidence for the low-damage quality of the surfaces is obtained from the properties of the epitaxial GaYGdIG films grown.

The as-sawed garnet slices were individually hand lapped on one side to produce flat surfaces for subsequent mounting on appropriate individual fixtures. The slices were then mounted, lapped face down, on the fixtures and were then subjected to a machine-lapping procedure. This employed a vibratory polisher with a metal-lapping plate and a series of loose Al_2O_3 abrasives in sizes ranging from 12 μm down to 3 μm. These lapping steps produced flat surfaces having typically a 3- to 5-μm finish. Each lapped surface was then individually machine polished, also on a vibratory polisher, using a slurry of Linde "A" (0.3-μm particle-size α-alumina) on a nylon cloth.

A variety of additional final polishing steps have been used for this program. The following have been most often used in preparing the garnet surfaces for epitaxy: (1) Linde "B" (0.05-μm α-alumina) following the Linde "A" step; (2) Zirconium Oxide (3- to 5-μm particle size) following the Linde "A" step; and (3) Cab-o-sil (0.05-μm particle-size specially-prepared SiO_2) following the Linde "A" step.

4.1.3 Results. – Photographs of typical boules are shown in figures 7, 8, 9 and 10. Figures 7, 8, and 9 are of single garnet compositions of neodymium gallium garnet ($Nd_3Ga_5O_{12}$), samarium gallium garnet ($Sm_3Ga_5O_{12}$), and gadolinium gallium garnet ($Gd_3Ga_5O_{12}$). The color of the $Nd_3Ga_5O_{12}$ is purple and that of the $Sm_3Ga_5O_{12}$ is orange, while the $Gd_3Ga_5O_{12}$ is transparent. A mixed-garnet boule, $Sm_{0.48}Gd_{2.52}Ga_5O_{12}$, is shown in figure 10. The color of the mixed garnets varied. The crystals that were a mixture of $Gd_3Ga_5O_{12}$ and $Nd_3Ga_5O_{12}$ were light purple. Those boules that were a mixture of $Gd_3Ga_5O_{12}$ and $Sm_3Ga_5O_{12}$ were light orange. Mixed boules of $Nd_3Ga_5O_{12}$ and $Sm_3Ga_5O_{12}$ were a burnt-orange color.

In all there were some 21 rare-earth gallium garnet boules grown. The details related to the growth of these crystals are summarized in table III. In the table the melting temperature and lattice constant for each boule is reported along with growth parameters for that particular boule. The melting temperatures reported are the uncorrected values as determined with an optical pyrometer. When making the reading, the pyrometer was focused on the liquid at the liquid/solid interface. The readings are reproducible to ±5°C. They are believed to be within ±30°C of the actual melting temperature because of the conditions under which the measurements were made. First, the insulated cavity over the crucible reflects most of the radiation. Second, the emissivity of the liquid melt should be very near unity, which would necessitate only a small correction to the measured temperatures.

The growth of the single-garnet compositions was rather straightforward and easy after the melting temperature and melt composites were established. The growth of the mixed-garnet composition was somewhat more difficult. A slower pull rate was required for these boules to minimize the formation of voids. Also, mixed garnets of adjacent rare earths like Nd and Sm seemed to grow with less difficulty and were

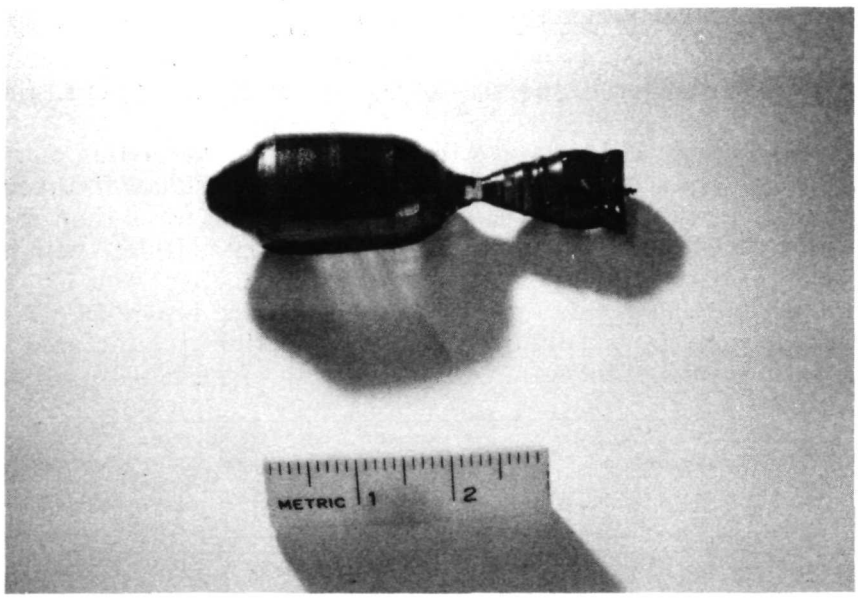

Figure 7. – $Nd_3Ga_5O_{12}$ Boule

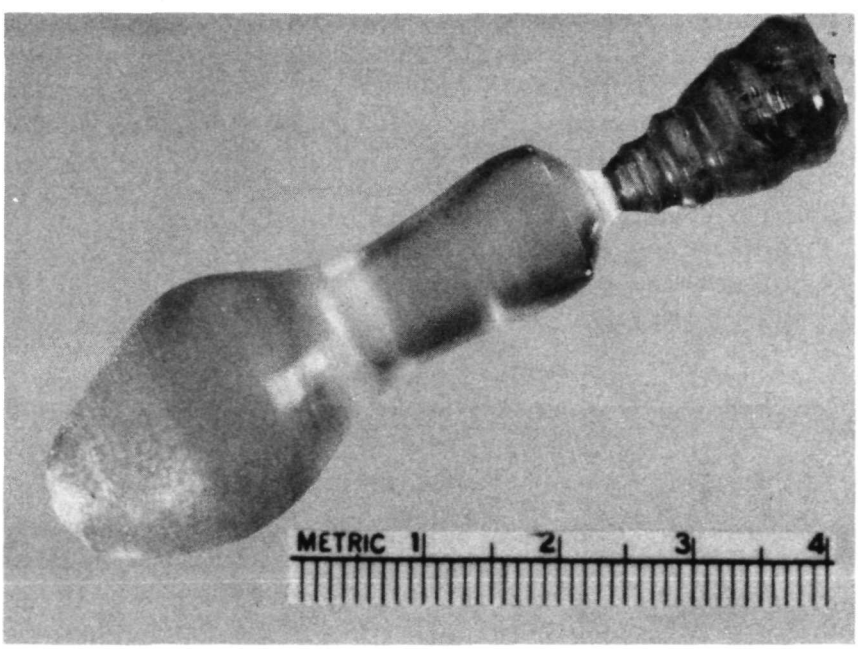

Figure 8. – $Sm_3Ga_5O_{12}$ Boule

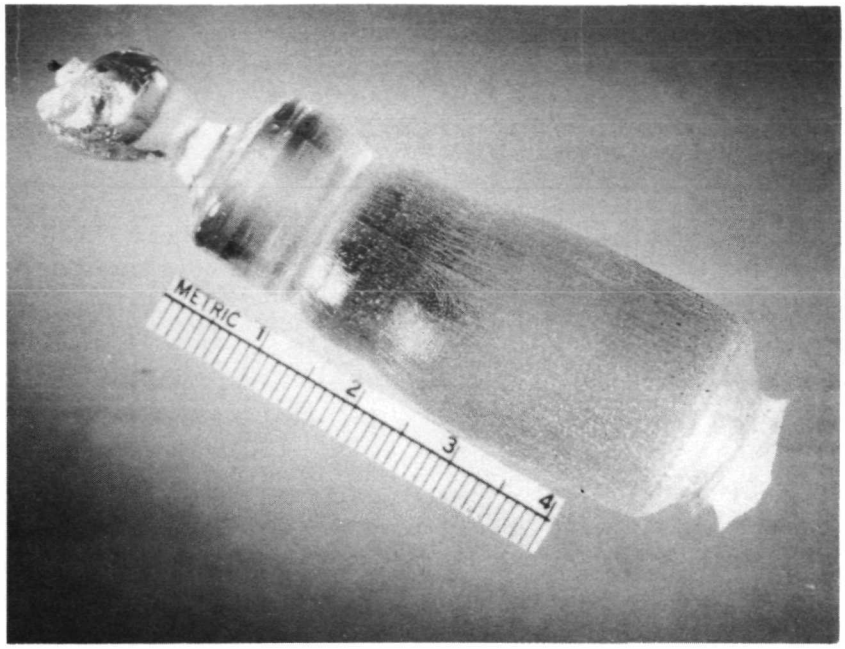

Figure 9. – $Gd_3Ga_5O_{12}$ Boule

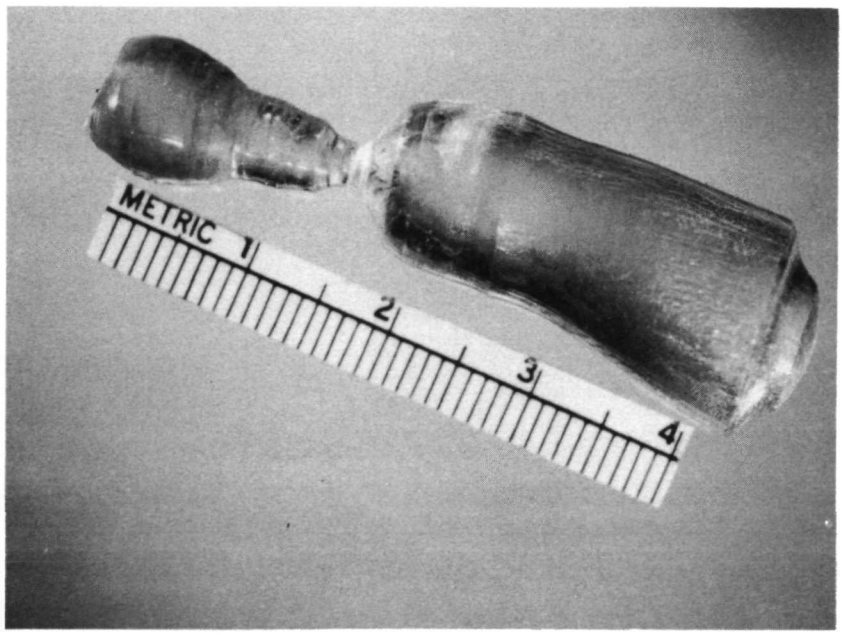

Figure 10. – $Sm_{0.48}Gd_{2.54}Ga_5O_{12}$ Boule

TABLE III. – CRYSTAL GROWTH SUMMARY

Boule Number	Melt Composition	Melting Point °C	Lattice Constant A°	Pull Rate Inch/Hour	Rotation rpm	Remarks
NR-3	$Nd_3Ga_5O_{12}$	1550	12.506	1/4	10	Purple color, good quality
NASA-1	$Nd_{1.76}Gd_{1.24}Ga_5O_{12}$	1460	-	1/4	10	Polycrystalline
NASA-2	$Nd_{1.76}Gd_{1.24}Ga_5O_{12}$	1460	-	1/2	10	Polycrystalline
NASA-3	$Nd_{1.76}Gd_{1.24}Ga_5O_{12}$	1635	-	1/4	10	1% excess Ga_2O_3 in melt
NASA-4	$Nd_{1.76}Gd_{1.24}Ga_5O_{12}$	1635	12.4432	1/4	10	1/2% excess Ga_2O_3 in melt
NASA-5	$Nd_{1.76}Gd_{1.24}Ga_5O_{12}$	1635	-	1/4	10	1-1/2% excess Ga_2O_3 in melt
NASA-6	$Sm_3Ga_5O_{12}$	1645	12.436	1/4	5	1.17% excess Ga_2O_3 in melt
NdSmG-1	$Nd_{0.699}Sm_{2.301}Ga_5O_{12}$	1630	-	1/4	5	Voids and inclusions evident
NdSmG-2	$Nd_{0.699}Sm_{2.301}Ga_5O_{12}$	1630	12.4547	1/8	5	A few voids and inclusions
NdSmG-3	$Nd_{0.699}Sm_{2.301}Ga_5O_{12}$	1630	12.4522	1/8	5	A few voids and inclusions
	$Sm_3Ga_5O_{12}$	1645	12.4166	1/8	5	1.17 wt% Ga_2O_3 in melt
SmGG-3	$Sm_3Ga_5O_{12}$	1645	-	1/4	5	-
SmGG-4	$Sm_3Ga_5O_{12}$	1645	-	1/8	5	-
SmGG-5	$Sm_3Ga_5O_{12}$	1645	12.4384	1/8	10	-
SmGdG-1	$Sm_{1.88}Gd_{1.12}Ga_5O_{12}$	1700	-	1/8	5	-
SmGdG-2	$Sm_{0.48}Gd_{2.52}Ga_5O_{12}$	1720	12.3910	1/8	5	-
SmGdG-3	$Sm_{0.48}Gd_{2.52}Ga_5O_{12}$	1720	12.3885	1/8	5	-
G^3-1	$Gd_3Ga_5O_{12}$	1735	12.3829	1/8	5	Good-quality material
G^3-2	$Gd_3Ga_5O_{12}$	1735	12.3825 AV	1/8	5	Small crystal
G^3-3	$Gd_3Ga_5O_{12}$	1735	12.3841 AV	1/8	5	Ground 10° off (111)
N-6	$Gd_3Ga_5O_{12}$	1735	12.3858 AV	1/8	5	10 1-in. diameter substrates
TbGG-1	$Tb_3Ga_5O_{12}$	1790	12.347	1/8	5	Cracked boule

generally of better quality than those compositions of rare-earth that were more widely separated in the periodic table like Nd and Gd. This tendency is probably related to the fact that the melting temperature of the rare-earth gallium garnets progressively increase as the atomic number of rare-earth increases.

Physical and optical properties as determined for several of the garnet materials are reported in table IV. Values for $Gd_3Ga_5O_{12}$, $Nd_3Ga_5O_{12}$, $Sm_3Ga_5O_{12}$, and $Nd_{1.76}Gd_{1.24}Ga_5O_{12}$ are presented. $Gd_3Fe_5O_{12}$ is included for comparison. The densities were calculated from the measured lattice constants. The refractive index was determined with the aid of Cargille index of refraction liquids. The procedure was to place some of the garnet material in the liquid of known index and to observe the liquid/garnet interface under the microscope. When a close match of indices was observed one could see a bright band of light around the solid. This band would move into the higher index media as the focal plane was moved down.

The index of refraction for the gallium garnets fall in the range of 1.70 to 1.72 except for samarium gallium garnet, which has a value of 2.00. The hardness values were determined with a Leitz Miniload Hardness Tester. The load used was 300 grams. A small load was used to minimize cracking around the DPH indentation so as to obtain accurate hardness numbers.

The optical transmission spectra for $Sm_3Ga_5O_{12}$, $Nd_3Ga_5O_{12}$, and $Gd_3Ga_5O_{12}$ was determined in the visible and infrared regions with a Beckman model DK-1A spectrophotometer and a Beckman model IR-4 spectrophotometer. The samples were thin slices polished flat and parallel on both sides. The results of these measurements are shown in figures 8, 9 and 10. In the figures the percent transmission is shown as a function of wave length. The thickness and other details of the sample are noted on the respective graphs. Very deep absorption bands were noted for the $Sm_3Ga_5O_{12}$ and $Nd_3Ga_5O_{12}$ in the visible spectrum. This is characteristic for these rare-earths.

4.1.4 Discussion. – The growth of the rare-earth gallium garnets is complicated by the fact that they must be grown in air. This was first pointed out by Linares (ref. 53). The problem is that gallium oxide decomposes to a gaseous suboxide at elevated temperatures by the following equilibrium reaction:

$$Ga_2O_{3\,(\text{Liquid Melt})} \rightleftharpoons Ga_2O_{(\text{Gas})}\uparrow + O_{2\,(\text{Gas})}\uparrow$$

As indicated by the equation, high temperatures and a low oxygen pressure over the liquid melt tends to drive the decomposition reaction to the right. Attempts to grow the rare-earth gallium garnets in neutral atmosphere such as argon or nitrogen caused white fumes of the Ga_2O to rise from the melt. The loss of this suboxide causes the melting temperature of the liquid to decrease as the composition of the melt becomes richer in the rare-earth oxide component. Also inclusions are found in boules grown under these conditions. With an air environment, the reaction proceeds slowly enough so that it does not present a real problem during the crystal growth runs.

TABLE IV. – PROPERTIES OF SELECTED RARE-EARTH GALLIUM GARNETS

Property	$Gd_3Fe_5O_{12}$	$Sm_3Ga_5O_{12}$	$Gd_3Ga_5O_{12}$	$Nd_{1.76}Gd_{1.24}Ga_5O_{12}$	$Nd_3Ga_5O_{12}$
MP--°C	1640°C	1645	1735	1635	1550
Hardness DPH ±40		1230	1250	1260	1175
Color	Green	Orange	Clear	Light Purple	Purple
Density** (gm/cc)	6.459	6.846	7.080	6.841	6.609
Lattice Constant A°	12.471***	12.438	12.383	12.432	12.506
Refractive Index	-	2.00	1.720	1.710	1.700

*Leitz Miniload Hardness Tester - 300 gram load
**Calculated from Lattice Constant
***Geller, S., Espinosa, L. and Crandall, D. E., J. Appl. Cryst. 2 86 (1969)

Growth of the crystals in air does result in difficulties with the oxidation of the iridium crucible. After pulling several crystals from a melt, iridium oxide occasionally floats free from the sides of the crucible and attaches itself to the growing crystal. This oxide is then incorporated into the growing crystal. Such inclusions will cause the crystal to crack during subsequent cooling. This oxide also permeates the insulation, coats the cover cap, and condenses on the furnace walls. It is electrically conductive and causes arcs at the rf leads when it is sufficiently thick to provide a low resistive path. The harmful effects are minimized by keeping the pulling times and heating times short so that only a small amount forms during growth.

The boules occasionally contained voids and a few iridium inclusions. The voids were located in bands that appeared to conform to the convex growth interface of the crystals. In addition, they seemed to be strung out in the direction of the boule axis. These bands were generally localized to regions of the crystal where the diameter increased sharply in response to a decrease in the crucible control temperature.

The formation of these voids is related to the amount of dissolved gases in the molten oxide at the crystal interface. Considering the decomposition reaction and the inherently higher solubility of gases in the liquid than in solids, one can visualize the nucleation of gases bubbles on the surface of the growing crystal when the crucible control temperature is abruptly lowered. Such a situation creates a condition of supersaturation of the dissolved gases as the crystal rapidly grows out and rejects dissolved gases. When the concentration of these gases exceeds the solubility limits sufficiently,

gas bubbles form and attach themselves to the growing crystal. Growth of the crystal around these bubbles then results in the formation of the veil-like voids. The composition of the gas is probably a mixture of nitrogen, oxygen, and possibly the gallium suboxide Ga_2O that probably exists in the liquid as an identifiable species.

The presence of the iridium inclusions can be explained in a similar fashion. First, one notes that there is a considerable solubility of the iridium metal in the rare-earth garnet melts. The metal frequently will start to come out of solution in the liquid-crystal-air interface and coat the crystal. Usually a sharp drop in the control temperature initiates the formation of this iridium coating. Once it is nucleated, the metal continues to come out of solution and collect onto the crystal surface.

The fact that there is a considerable amount of iridium dissolved in the oxide melt is further borne out by examining the crucibles during cleaning. One often finds a sponge like masses of iridium deposited on the bottom of the crucible. This sponge apparently forms as iridium precipitates out of solution and deposits on the crucible floor as the melt freezes. The few iridium inclusions found in the crystal result from localized supersaturation of the melt, nucleation of iridium particles, and incorporation of these particles at the growing crystal interface.

The formation of the voids was much more pronounced in the mixed-garnet boules than in the single-garnet boules. To minimize void formation in the mixed garnet compositions the pull rate was reduced from 0.25 in./hr to 0.125 in./hr. A significant reduction in the voids was noted. To further minimize the formation of the void, a modification of the temperature control system was made so that the crucible temperature changes could be made continuously over a period of ten min or so. A further decrease in the occurrence of voids was noted. No doubt all of the voids could be eliminated by further modification of the crystal growth parameters. One such change might be to increase the crystal rotation rate.

Transmission and reflection topographs of selected sections of a number of the crystals revealed the presence of growth striations. (See figures 11, 12, and 13). The origin of these striations has not been determined but is believed to be due to pulling the crystal under a conditions of thermal asymmetry (ref. 54). That is, the crystal growth axis does not conform to the thermal center of the crucible. The loss of radiation through the viewing slot of the insulated cavity contributes to this condition.

4.1.5 Conclusions. - Conclusions are as follows:

(1) $Sm_3Ga_5O_{12}$, $Nd_3Ga_5O_{12}$, and $Gd_3Ga_5O_{12}$ can be grown in single-crystal form by the Czochralski method in air.

(2) Mixed rare-earth gallium garnet compositions in the system $(Nd_{x-3}, Gd_x)Ga_5O_{12}$, $(Sm_{x-3}, Gd_x)Ga_5O_{12}$, and $(Nd_{x-3}Sm_x)Ga_5O_{12}$ can also be grown by the same method.

(3) The melting point and lattice constant of the mixed garnet are for all practical considerations a linear function of the composition.

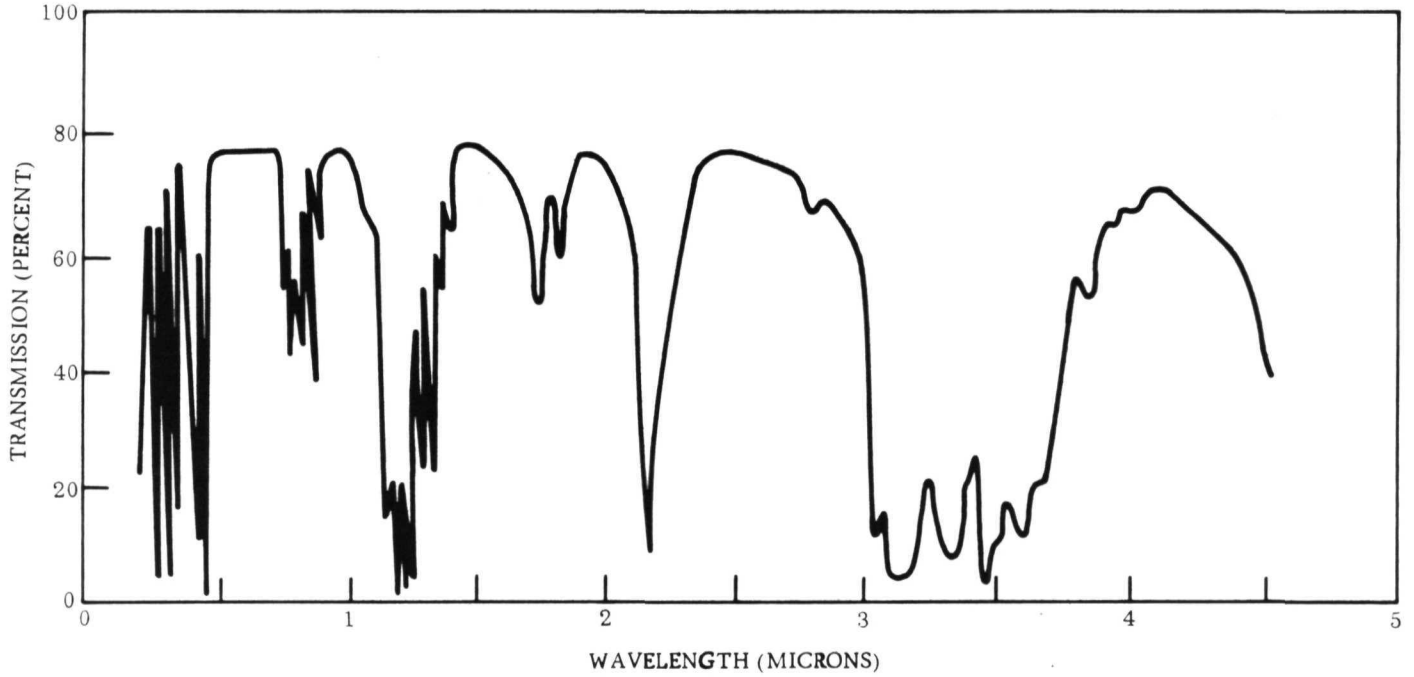

Figure 11. – Optical Transmission Spectra of $Nd_3Ga_5O_{12}$

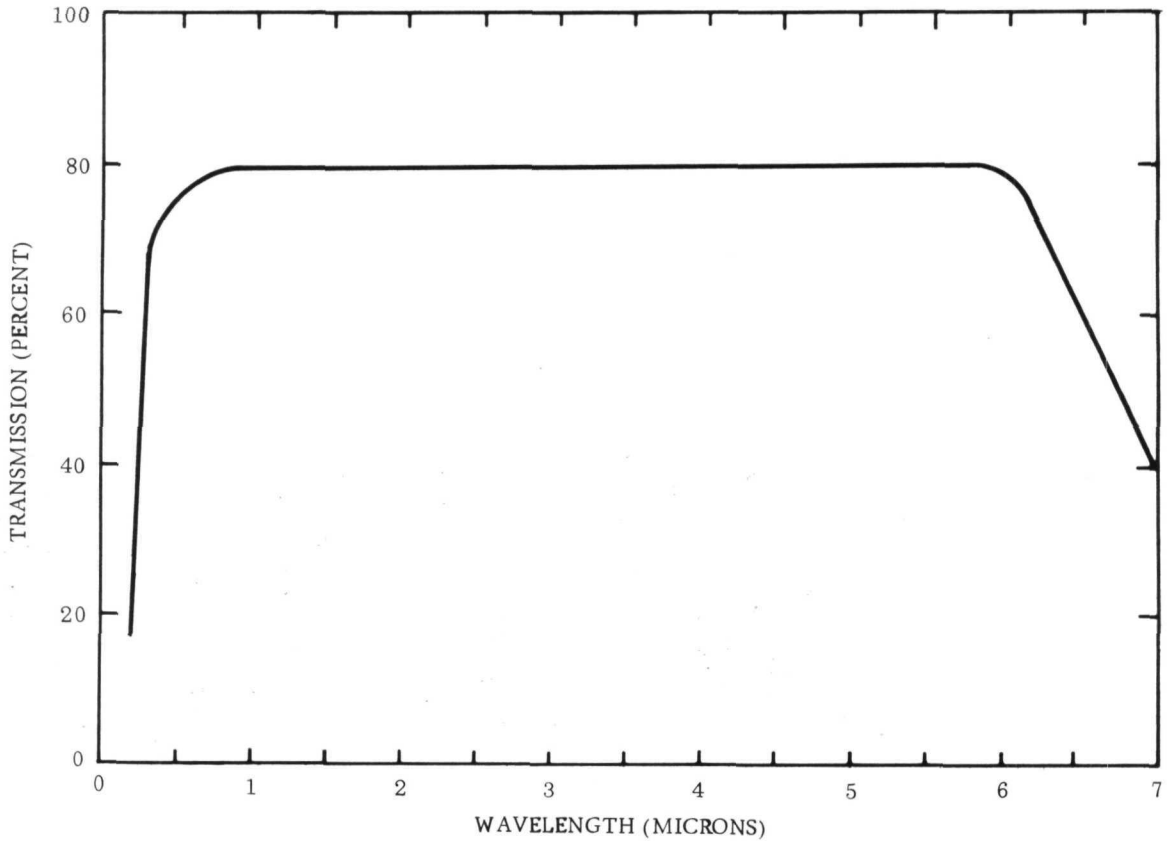

Figure 12. – Optical Transmission Spectra of $Sm_3Ga_5O_{12}$

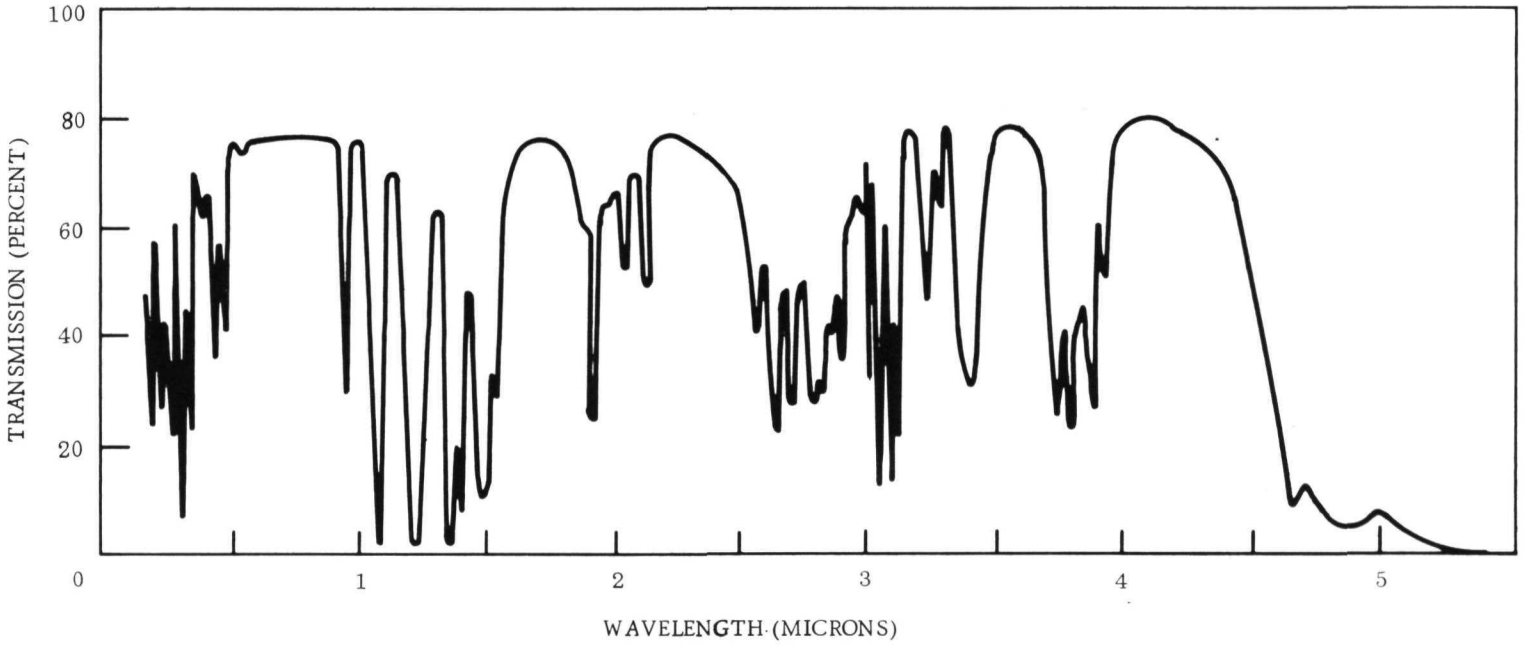

Figure 13. – Optical Transmission Spectra of $Gd_3Ga_5O_{12}$

(4) Although problems with growth striations and void formation were encountered, these problems do not appear insurmountable and can be minimized if not eliminated by modifying the thermal configuration, pulling method, and the crystal growth parameters.

(5) The mixing of two single rare-earth gallium garnet compositions to produce a mixed-garnet material with a specific lattice constant that introduces the desired amount of strain in the magnetic oxide films has been accomplished.

4.1.6 Recommendations for future work. – Future work recommendations are as follows:

(1) Efforts should be concentrated on the growth of large mixed-garnet boules free of voids, inclusions and other defects that could propagate into the film.

(2) Studies should be conducted to determine the extent that banding and growth striations will affect bubble-domain mobility. Further, the condition for growth of substrate boules free of these striations should be established.

4.2 Epitaxial Deposition

4.2.1 Introduction. – The CVD processes used for deposition of magnetic thin films in this program or of other specific materials in other programs depend on the controlled reaction of gaseous components in a heated reaction chamber. The substrate receiving the deposit is placed in a favorable position in this reaction chamber. The reaction products and unreacted gases are swept out of the chamber and into an exhaust system.

These processes are carried out in a T-shaped reaction chamber, 4 ft wide and 4 ft high, made of 2- or 3-in. diameter fused silica tubing as shown in figure 14. Anhydrous metal halides are contained in platinum or fused silica crucibles that are independently heated to control the individual vapor pressures. These vapors mix as they are swept up the vertical portion of the reactor by an inert carrier gas. Oxidizing gases, introduced into one horizontal arm of the reactor, mix with the halide vapors at the crux of the T to deposit metal oxides downstream on substrates at 1100 to 1200°C.

A characteristic of the CVD process called the shifting reaction zone (SRZ) behavior (ref. 5), provides a basis for process control. The SRZ is a simple extension of thermodynamic reactivity principles that largely control the garnet depositions. In deposition of YIG (ref. 5), for example, products other than YIG also are formed. Depending on the gas-flow conditions and the concentrations of yttrium chloride (YCl_3), iron (II) chloride ($FeCl_2$), H_2O, O_2, and HCl, the possible products include yttrium oxide (Y_2O_3), yttrium orthoferrite ($YFeO_3$), yttrium iron garnet ($Y_3Fe_5O_{12}$) iron oxides (Fe_2O_3 and Fe_3O_4), or mixtures of these compounds. In any given run as many as three and sometimes four of these are deposited in or near the seed area. These products appear in a very orderly manner, however, and

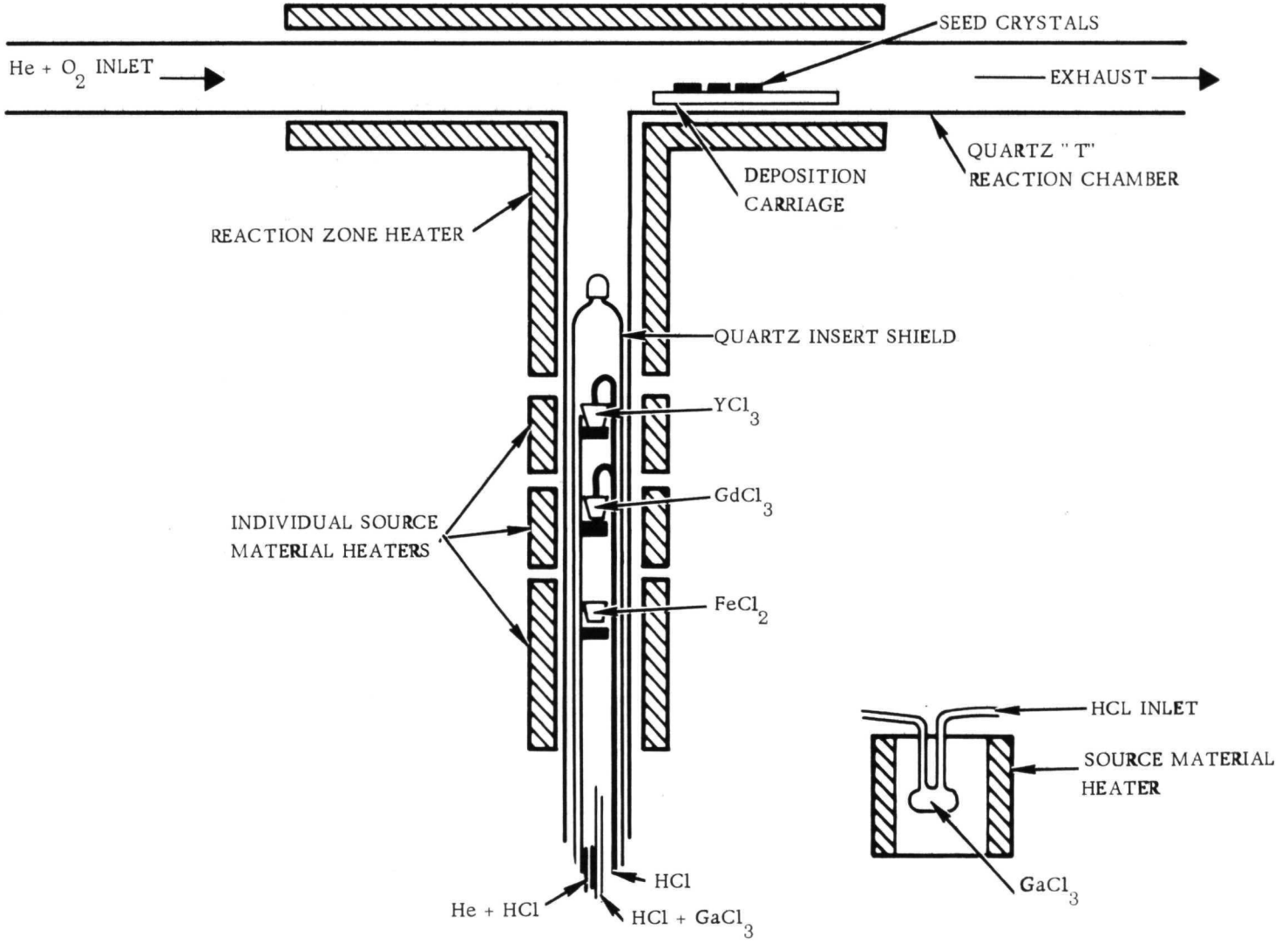

Figure 14. – The T Reactor for Garnet Depositions

their order of appearance is consistent with the chemical reactivity of YCl_3 and $FeCl_2$. Thus, because YCl_3 is considerably more reactive than $FeCl_2$, Y_2O_3 is formed first in the reactor, followed by $YFeO_3$, $Y_3Fe_5O_{12}$, and finally Fe_2O_3. The total reaction zone embracing the Y_2O_3, $YFeO_3$, $Y_3Fe_5O_{12}$, and Fe_2O_3 can be shifted from run to run, and the individual reaction zones; e.g., the $Y_3Fe_5O_{12}$ or $YFeO_3$ zone, can be shifted or expanded at the expense of the other zones. However, the sequence of deposits is always the same. Additional details and discussions are in ref. 5.

But how does the SRZ behavior manifest itself in the GaYGdIG depositions? With the addition of the third and fourth metal halide reactants, gadolinium chloride ($GdCl_3$) and gallium chloride ($GaCl_3$), the products may presumably include any possible single or mixed oxides of Y_2O_3, Gd_2O_3, Fe_2O_3, and Ga_2O_3. However, under the experimental conditions employed to date, the YCl_3 and $GdCl_3$ behave as one source material so that essentially the same basic rare-earth oxide, orthoferrite and garnet zones, are observed.

Thus the oxide zone is a mixture or solid solution of Y_2O_3 and Gd_2O_3, the orthoferrite zone is a mixture or solid solution of $YFeO_3$ and $GdFeO_3$, and the garnet zone is a solid solution of $Y_zGd_{3-z}Fe_5O_{12}$. The exact nature of the oxide and orthoferrite zones was not of major concern in this program and was not explored in any detail. However, most likely the orthoferrite deposit is also a solid solution like the garnet deposit. With the addition of the $GaCl_3$ there is also no change in the basic rare-earth oxide, orthoferrite and garnet zones, under transport conditions used for this program. Again there was no need and hence no attempt to determine if any significant amounts of gallium are incorporated in the rare-earth oxide or orthoferrite deposits. However, the gallium is readily incorporated in the garnet deposits where it substitutes for part of the iron as desired. $GaCl_3$ is less active than YCl_3 and $GdCl_3$, but slightly more reactive than $FeCl_2$, so the gallium concentration is somewhat higher in the front of the garnet zone and lower in the downstream end of the zone. Thus, in the front of the zone, x in $(Y, Gd)_3Ga_xFe_{5-x}O_{12}$ will be high because $GaCl_3$ is more reactive than $FeCl_2$. As the more reactive $GaCl_3$ is partially depleted, more $FeCl_2$ will react and (Ga/Fe ratio) and will be continually lower in deposits downstream. The effect is not large and can be minimized by proper control of the $GaCl_3$ and $FeCl_2$ transport conditions.

4.2.2 Reactors. - Early depositions were performed in reactor Ag-1, which has a T-reaction chamber made of 2-in. diameter fused silica tubing. This was the first T-reactor designed and used for the epitaxial YIG films (ref. 3) and also used successfully for depositing GdIG films (ref. 1 and 3). However, AG-1 has only three separately controlled regions in the vertical section of the furnace. This is adequate for unsubstituted YIG (or GdIG or other rare-earth iron garnets) where there are only two source materials, YCl_3 and $FeCl_2$, to be maintained at separate temperatures. However, we were not able to obtain the necessary temperature profile in AG-1 to give adequate control over the transport of three source materials YCl_3, $GdCl_3$, and $FeCl_2$ required for the YGdIG films and the GaYGdIG films. (As discussed later, vapors of the fourth source material, $GaCl_3$ were injected into the vertical section from an external source). Figure 15 shows typical AG-1 temperature profiles for the three source materials. Either the $GdCl_3$ or the $FeCl_2$ were in regions with steep temperature gradients that resulted in continually decreasing vaporization rates throughout the runs.

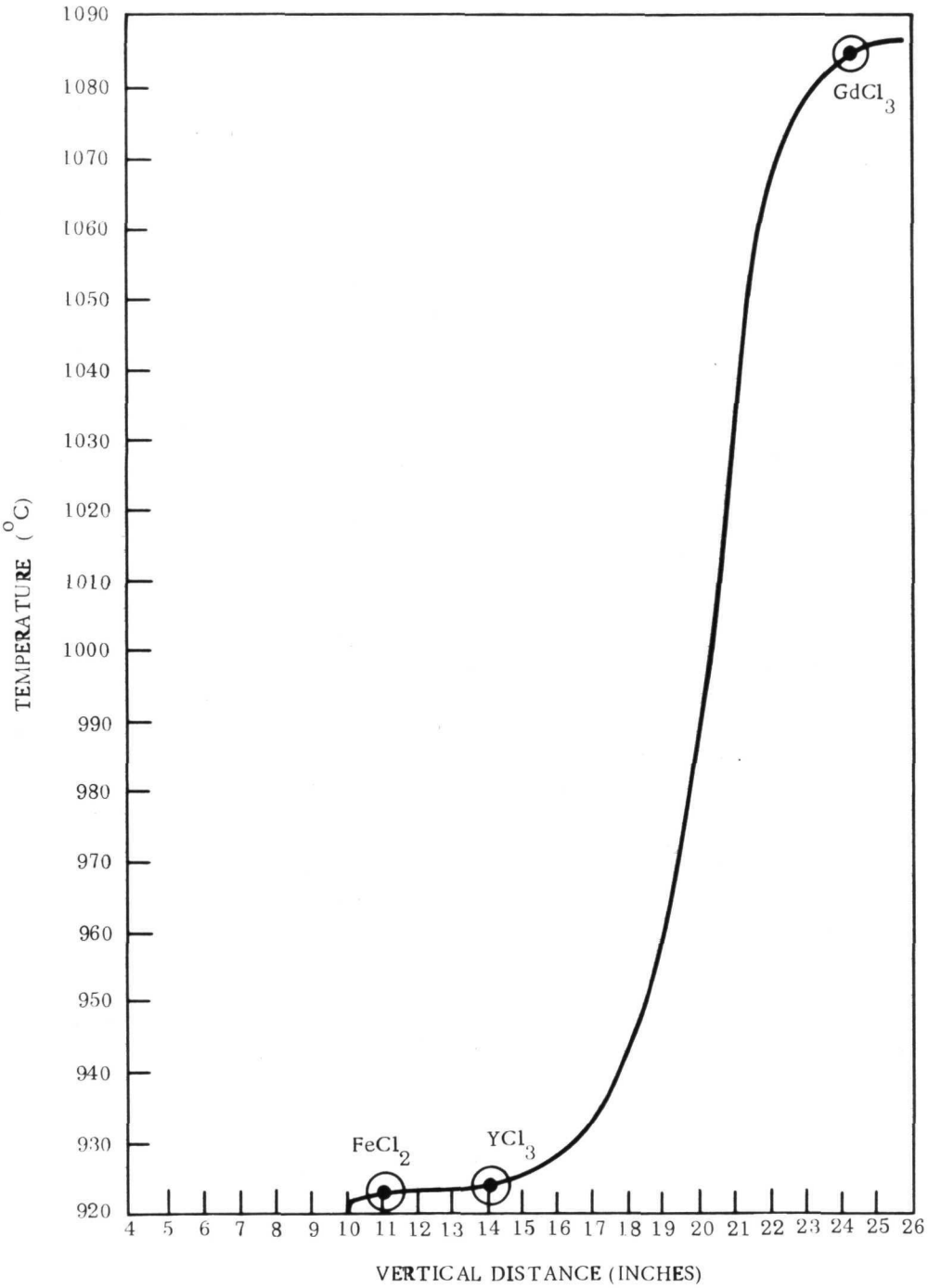

Figure 15. – Typical Three-Zone Profile for Reactor AG-1

A newer reactor, AG-2, became available in July 1970. AG-2 had six separately controlled regions in the vertical section. Two very flat temperature zones for the $FeCl_2$ and $GdCl_3$ and an acceptably flat zone for the YCl_3 were obtained in this reactor. AG-2 also had the 2-in. diameter reactor tubing. Most of the work was performed in this reactor.

In May and June of 1971, AG-2 was shut down for various necessary repairs in the control unit and to change the reactor tube. While it was down it was modified to accommodate a T made of 3-in. diameter tubing rather than the 2-in. tubing. The 3-in. tubing offered various immediate and potential advantages and had already been successfully used in the latest reactor, AG-3. Immediate advantages included less cluttering of the source cup holders and gas inlet tubes. Thus the tasks of loading source materials and connecting gas lines are easier and less susceptible to accidents. Larger source cups are used so, if desired, one charge of materials will last several hours and permit several depositions without reloading. Finally, the garnet deposition zone is larger with obvious potential advantages if we wish to deposit on larger substrate wafers or on several wafers simultaneously.

Following several conditioning runs the last series of runs on this contract were performed in the now modified AG-2.

4.2.3 Source materials. - The source materials for the metal ion components in the films were anhydrous metal chlorides namely YCl_3, $GdCl_3$, $FeCl_2$ and $GaCl_3$. Anhydrous YCl_3 and $GdCl_3$ are obtained from the Lunex Co. of Pleasant Valley, Iowa. They are further purified by vacuum sublimation in a molybdenum sublimation train at about 1050°C. The anhydrous $FeCl_2$ is prepared by direct reaction of iron wire with HCl gas at temperatures just slightly above the $FeCl_2$ melting point (677°C). A vertical fused-silica reactor is used which permits the molten $FeCl_2$ to drip into a collecting crucible as it is formed, thus leaving the iron wire continually exposed for reaction with the HCl gas (ref. 55). A normal batch preparation yields 250 to 350 grams. The product is in chunk form which is desirable, since a minimum surface area is exposed to air when the batch is unloaded. The anhydrous YCl_3, $GdCl_3$ and $FeCl_2$ are stored in evacuated containers. Loading of crucible for depositions is performed in a dry box.

Anhydrous $GaCl_3$ is obtained in sealed ampoules from Research Inorganic Chemical Co., Sun Valley, California. Containers are filled by vacuum distillation.

We have had inquiries from time to time on the need for separate YCl_3 and $GdCl_3$ sources versus one source of a solution of $GdCl_3$ in YCl_3 (or vice versa depending on which is the major component). The same question applies to any mixed rare-earth halide system. For example; Robinson, et al (ref. 26) used a molten solution of $TbCl_3$ and $ErCl_3$ in one source cup for their depositions of epitaxial films of $Tb_{3-z}Er_zFe_5O_{12}$. In some brief, unreported work on epitaxial garnet films for microwave applications we deposited YGdIG films using molten solutions of $GdCl_3$ in YCl_3. However, not unexpectedly, we experienced a continual change in the YCl_3:$GdCl_3$ transport ratio. The YCl_3:$GdCl_3$ mole ratio in the vapor was always greater than in the melt so the melt composition (and hence vapor composition) did not remain constant. Thus, unless a constant boiling mixture can be attained, we prefer separate sources. Also, where different film compositions are being investigated, separate sources in

separate temperature regions readily permit controlled changes in transport rates of the individual components.

Since the magnetic bubble-domain characteristics of the GaYGdIG films (or any of the gallium-substituted iron garnet films) are very sensitive to gallium content, a technique for critically controlling the introduction of gallium into a depositing film is required. $GaCl_3$ has a much higher vapor pressure than YCl_3, $GdCl_3$, and $FeCl_2$. Typical temperatures used to provide the necessary concentrations of vapors during a deposition run are 1055°C for YCl_3, 972°C for $GdCl_3$, 950°C for $FeCl_2$, and 162°C for $GaCl_3$. Thus a low-temperature furnace, separate from the high temperatures of the T-reactor, is used to control the $GaCl_3$ vapor pressure and the $GaCl_3$ vapors are injected into the vertical section of the reactor. Problems encountered with this method included: (1) condensation of $GaCl_3$ in tubing and connections and on chamber walls, (2) premature reaction of $GaCl_3$ with air due to leaks, and (3) changing evaporation rate due to a falling level of $GaCl_3$ in the source vessel during successive runs. However, the arrangement evolved during this program and shown in figure 16 prevents condensation and gives fair reproducibility and control. With this system we were able to reproduce $GaCl_3$ transport rates within 0.1 gm/hr for a 1.6 gm/hr rate.

4.2.4 Film growth. - In a typical run for depositing GaYGdIG, the anhydrous metal halides are loaded into crucibles, weighed, and positioned in separate thermal zones of the reactor. The $GaCl_3$ injection line and gas lines are connected to the reactor and the $GaCl_3$ furnace is brought up to temperature. The vaporized halides mix as they rise up the vertical portion of the T-reaction chamber. At the crux of the T, the halides begin reacting with oxidizing gases to produce metal oxides that deposit from the gas stream. Since several products are produced by the reacting chemicals, the growth parameters must be adjusted to maximize the probability of depositing GaYGdIG and minimize the probability of depositing other products in the seed zone. Using the SRZ concept to adjust chemical ratios and concentrations, the GaYGdIG deposition zone may be extended to cover 3.5 in..

Once the proper conditions have been achieved and stabilized, the seed crystals are pulled into the deposition zone that is located a few in. downstream from the crux of the T. At the conclusion of a deposition period, the seed crystals are withdrawn from the deposition zone. The source chemicals are cooled and weighed to determine use rate. Typical deposition conditions for AG-2 with 2-in. diameter and 3-in. diameter tubing are listed in table V. If desired, several depositions can be performed before reweighing and reloading the source chemicals.

The color of GdIG; YGdIG and GaYGdIG in thin-film form is green so their presence on a substrate is readily evident. Good films are uniformly smooth (uncrazed) and specularly reflecting. Full-circle X-ray diffraction and back-reflection Laue diagrams show the magnetic garnet films to be single crystals that are oriented parallel to the substrate.

4.2.5 Compositions. - Films deposited on this program included $Gd_3Fe_5O_{12}$ (GdIG), $Y_zGd_{3-z}Fe_5O_{12}$ (YGdIG), and $Y_zGd_{3-z}Ga_xFe_{5-x}O_{12}$ (GaYGdIG). As will be discussed later, a few YIG depositions were also made to help solve some film roughness problems.

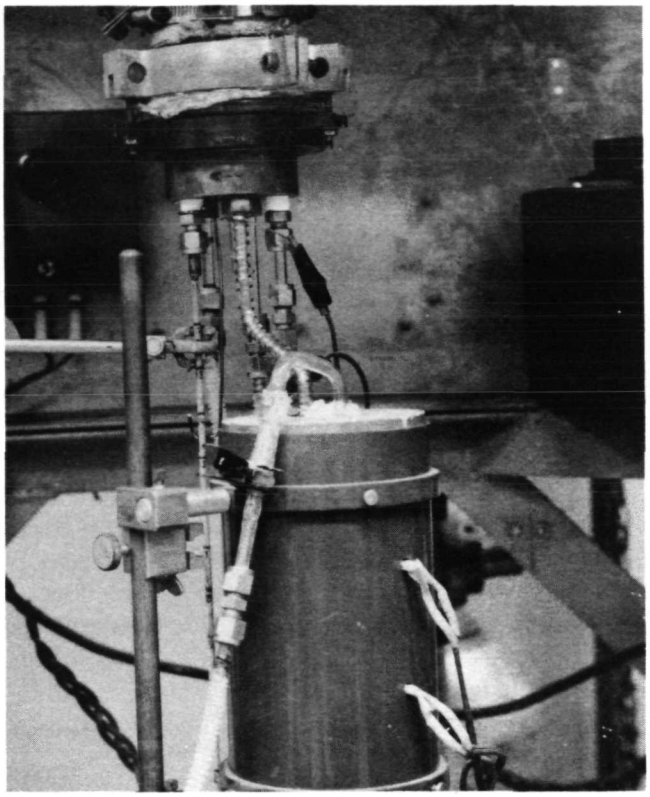

Figure 16. - Gallium Chloride Injection Apparatus

TABLE V. – GaYGdIG DEPOSITION CONDITIONS

Reactor Deposition Conditions	
Vertical Gasflows in (cc/min)	
He	10,370
HCl	0
HCl over YCl_3	95
HCl over $GdCl_3$	170
HCl over $GaCl_3$	48.8
Horizontal Gasflows in (cc/min)	
He	4725
O_2	43
Chemical Transport Rate in (gms/hr)	
YCl_3	0.793
$GdCl_3$	0.178
$GaCl_3$	1.62
$FeCl_2$	11.2
Deposition Temperature 1175°C	

Most of the GdIG work was reported in the Interim Report dated February 1970 (ref. 1). However a few GdIG runs were made subsequent to that report. For example, epitaxial GdIG was deposited on (111) NdGdGG. Nominal substrate composition was $Nd_{1.75}Gd_{1.25}Ga_5O_{12}$. The deposits were very inhomogeneous with three kinds of general growth features – very rough with polycrystalline nuclei, almost smooth, and very smooth. This was apparently due to bad-quality, inhomogeneous substrate material. Epitaxial GdIG was also deposited on (111) SmGaG. The magnetic domains were vertical, single-wall domains but were immobile. The film surface was not good but in this case it was due to the deposition conditions. No other GdIG films were grown. However, work this past year (on this and other programs) now properly explains the GdIG film cracking reported in the Interim Report. The stress model (ref. 48 and Appendix of this report) clearly shows why cracking in epitaxial GdIG on GdGaG is more severe than for epitaxial YIG on GdGaG. The calculated stress of $\sim 3.5 \times 10^9$ dynes/cm^2 for GdIG on GdGaG is correct since this is a Region II film/substrate system; i.e., the stress results only from the thermal expansion coefficient mismatch between film and substrate. The calculated stress (ref. 1) of $\sim 4.1 \times 10^9$ dynes/cm^2 for YIG on GdGaG was incorrect. That is the calculated stress for a Region II film/substrate but, in fact, YIG on GdGaG is a Region I case (see ref. 48) and the calculated stress should be $\sim 1.6 \times 10^9$ dynes/cm^2. FMR data (ref. 48) indicates thin ($\sim 1\mu$m) YIG on GdGaG has $\sigma = 2.0 \times 10^9$ dynes/cm^2. We can now predict that, to avoid cracking in epitaxial GdIG films, the room termperature lattice constant difference, $\Delta a = a_s - a_f$, should be less than +0.010A if the substrate lattice constant a_s is larger than the lattice constant for GdIG ($a_f = 12.472$Å). The film should be in compression for substrates with a_s smaller than 12.472Å down to some limiting value, when the films will again be in tension. This assumes the films are always slightly more expansive than the substrates (ref. 48).

Most of the garnet films deposited on this program were YGdIG and GaYGdIG. Using Reactor AG-1, epitaxial YGdIG was first deposited on GdGaG, mostly (111)'s but a couple of (110)'s. The films were generally cracked with typical domain structures as shown in Figure 17. Although there were many single-wall domains they were immobile, apparently largely due to excessive stress in the films.

After the work was transferred to Reactor AG-2, YGdIG was deposited on (111) SmGaG and sometimes on (111) or (110 GdGaG. The run objectives were not always the same. For example, in Runs 2473 to 2477, 2479, and 2480, we were investigating different $GdCl_3$ and YCl_3 transport rates. In Runs 2478 and 2481, YGdIG was deposited on TbGaG to give more film substrate data on film cracking, etc. The epitaxial YGdIG films on TbGaG were cracked and the domains were immobile, vertical, single wall and serpentine domains. Certain of the YGdIG films on (111) SmGaG had in-plane domains while some had vertical single-wall and serpentine domains. However, it was difficult to analyze or interpret the films in detail because they were generally of very poor surface quality as shown in figures 18 and 19.

A series of deposition experiments were then performed with the explicit objective of determining if smooth films could be grown, or if there were some unique difficulties in growing smooth films in this mixed-garnet system. First, the conditions were changed to grow pure YIG films on GdGaG since it was know that smooth YIG/GdGaG could be grown. To keep the deposition conditions as near to the YGdIG

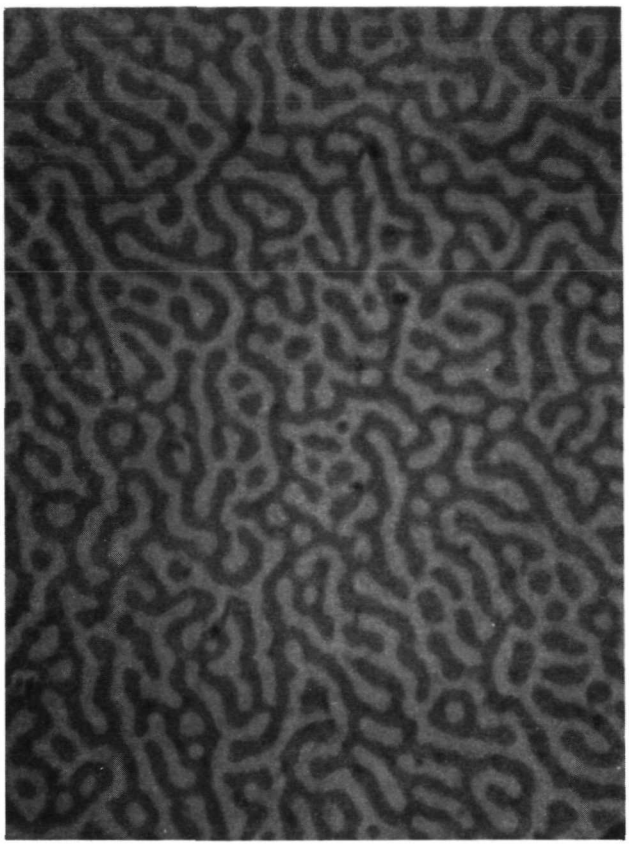

Figure 17. – Typical Domains in YGdIG Films

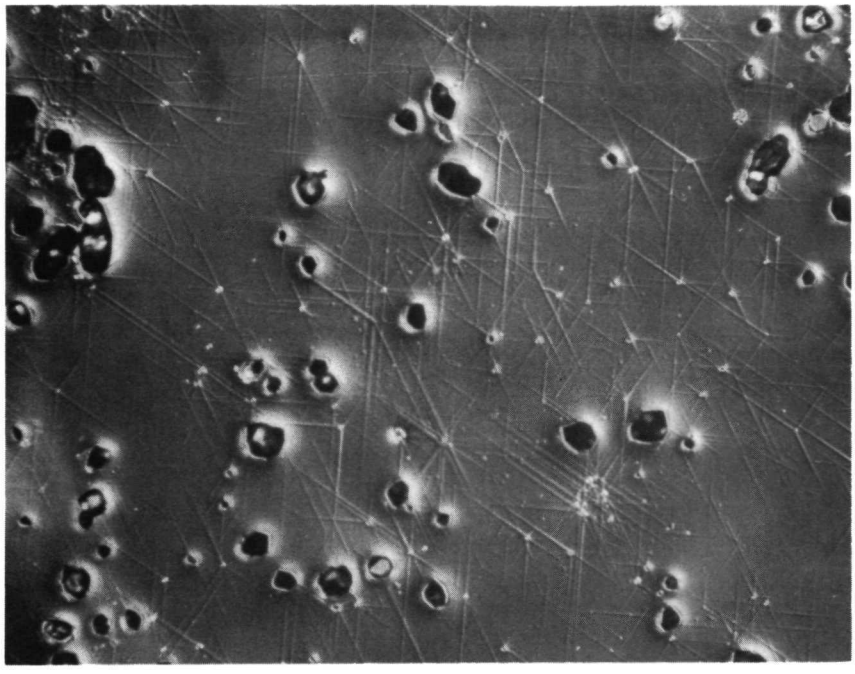

Figure 18. – Typical Rough YGdIG Films on SmGaG Under Previous Growth Conditions (AG-2, Run 484, 111X Magnification)

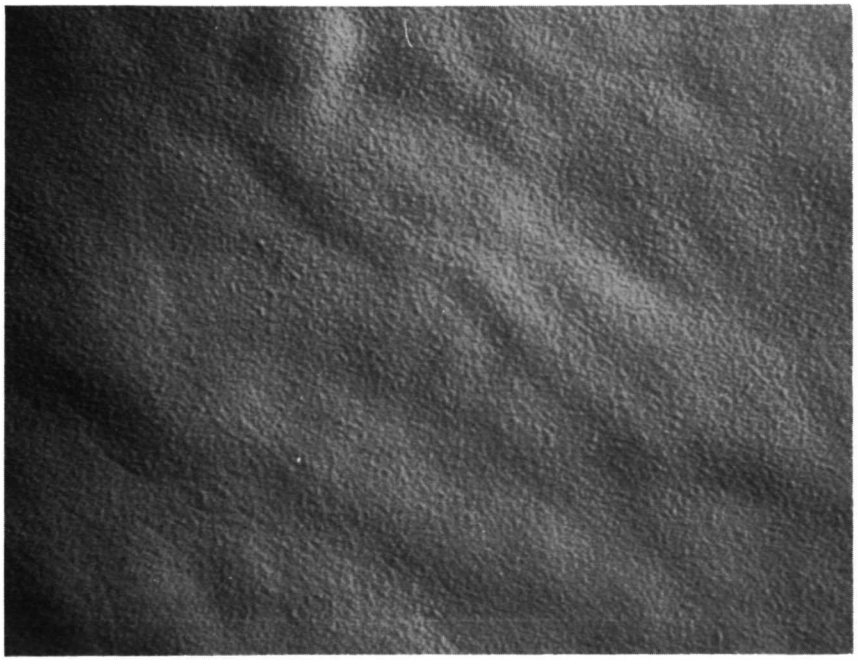

Figure 19. – Best Area in YGdIG Films on SmGaG Under Previous Growth Conditions (AG-2, Run 482, 115X Magnification)

deposition condition as possible, the $GdCl_3$ transport was simply discontinued and the YCl_3 transport rate was increased accordingly. All other run conditions remained the same as before. The run conditions are given in table VI. The resulting YIG deposits were also very coarse despite having a very long YIG zone.

Empirical changes were made in the deposition composition by lowering the $FeCl_2$ transport rate from 10.8 gm/hr to 9.4 gm/hr and also lowering YCl_3 transport rate from 1.18 gm/hr to 0.66 gm/hr (see table VI).

This shifted the YIG zone downstream and also slightly expanded it. There was no $YFeO_3$ on the test plate. The resulting films were generally smoother but still had numerous spurious nuclei on the surface. The oxygen flow was then lowered from 33 cm/min to 25 cc/min (see table VI). This shifted the YIG zone even further downstream and introduced a short $YFeO_3$ zone at the front of the test plates. The films were now smooth with no spurious nuclei.

TABLE VI. – YIG DEPOSITION CONDITIONS

Reactor Deposition Conditions	A	B
Vertical Gasflows		
He	6000 cc/min	6000 cc/min
HCl	78 cc/min	78 cc/min
HCl over YCl_3	144 cc/min	144 cc/min
Horizontal Gasflows		
He	2750 cc/min	2750 cc/min
O_2	33 cc/min	25 cc/min
YCl_3 Transport Rate	1.18 gm/hr	0.66 gms/hr
$FeCl_2$ Transport Rate	10.87 gm/hr	9.4 gms/hr
Deposition Temperature	1175°C	1175°C
Film Description A. Coarse film with numerous spurious nuclei on the surface B. Very smooth film with no spurious nuclei		

Having reestablished the conditions for smooth YIG/G[3], we now returned to the YGdIG depositions. $GdCl_3$ was put back into the reactor and the YCl_3 transport was reduced accordingly. A similar deposition zone was established where there was a short orthoferrite zone at the front of the test plates followed by an extensive YGdIG zone. Three, very smooth YGdIG films were now obtained on SmGaG substrates and a smooth film was even obtained on a multigrained NdGdGaG substrate. Typical run conditions for coarse and smooth films are given in table VII.

TABLE VII. – YGdIG DEPOSITION CONDITIONS

Reactor Deposition Conditions	A	B
Vertical Gasflows		
He	6000 cc/min	6000 cc/min
HCl	62 cc/min	62 cc/min
HCl over YCl_3	20 cc/min	10 cc/min
HCl over $GdCl_3$	215 cc/min	170 cc/min
Horizontal Gasflows		
He	2750 cc/min	2750 cc/min
O_2	32 cc/min	25 cc/min
YCl_3 Transport Rate	0.338 gms/hr	0.212 gms/hr
$GdCl_3$ Transport Rate	0.900 gms/hr	1.21 gms/hr
$FeCl_2$ Transport Rate	11.620 gms/hr	10.4 gms/hr
Deposition Temperature	1175°C	1175°C
Film Description A. Coarse film with numerous spurious nuclei on the surface B. Very smooth film with no spurious nuclei		

The reasons for these results are not clear although we might speculate that the rough deposits were due to spurious nuclei of Fe_2O_3 by being too close to the Fe_2O_3 zone, and/or the higher O_2 flow rates causing too oxidizing conditions such that some nuclei were formed in the gas phase and precipitated onto the growing film surface. Whatever the reason, we have since maintained conditions where there are short oxide and orthoferrite zones at the front of the test plate. Of course the films still have imperfections some of which are due to CVD growth phenomena and some to substrate

imperfections. But generally the film smoothness is quite good, typically as shown in figure 20, and certainly far superior to that shown in figures 18 and 19.

Although the earlier GdIG and YGdIG films on (111) SmGaG were not smooth their domain patterns supported the stress model (ref. 48 and Appendix in this report) first formulated in the GaYIG work on another program. In this program it was observed that unsubstituted GdIG on (111) SmGaG had vertical domains. When a little Y was substituted for part of the Gd, the domains were in-plane.

Since λ_{111} for GdIG and YGdIG is negative, this was interpreted as meaning that the GdIG films were in tension and the low Y containing YGdIG films were in compression. If the stress were just due to thermal expansion mismatch between film and substrate the YGdIG films should also have been in tension. The present stress model correctly predicts that YGdIG films with room temperature lattice constant, a_f slightly greater than that of SmGaG (12.436Å) will be in compression while YGdIG compositions with $a_f < 12.436$Å will be in tension. For films with $a_f > 12.436$Å there is a limiting mismatch between film and substrate so that GdIG films with $a_f = 12.472$Å will again be in tension.

Following the film smoothness experiments a few more epitaxial YGdIG films were deposited on (111) substrates of NdSmGaG with nominal composition $Nd_{0.7}Sm_{2.3}Ga_5O_{12}$ and nominal room temperature lattice constant, a_s of 12.452Å. They were smooth and were not cracked. Most had in-plane domains but film 2512 had narrow serpentine domains with tiny (2 - 3 μm diameter) bubbles near the edges.

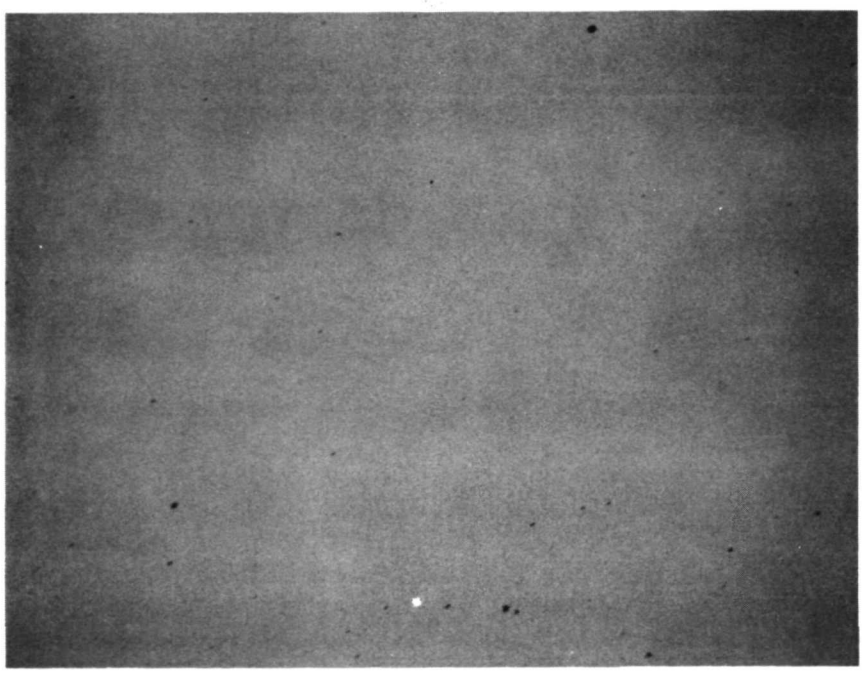

Figure 20. – Typical Area in YGdIG Films on SmGaG Under Present Growth Conditions (AG-2, Run 489, 115 X Magnification) (Photograph taken under same microscope lighting conditions as figure 19.)

Various compositions of GaYGdIG were then deposited epitaxially on (111) substrates of $Nd_{0.7}Sm_{2.3}Ga_5O_{12}$ with a_s = 12.454Å, SmGaG with a_s = 12.436Å, $Sm_{1.88}Gd_{1.12}Ga_5O_{12}$ and $Sm_{0.48}Gd_{2.52}Ga_5O_{12}$ (SmGdGaG) with a_s = 12.409 and 12.389, and GdGaG with a_s = 12.383. Investigation of epitaxial growth by CVD of this four cation bubble garnet system was the major contribution of this program. The results are discussed in the characterization section. The best bubble films were those with low Gd (typically $Y_{2.4}Gd_{0.6}Ga_{1.0}Fe_{4.0}O_{12}$). These, of course, had lower a_f's and the best substrate was GdGaG with a_s = 12.381A. Higher Gd films had good bubbles but were extremely temperature sensitive.

The problems of controlling composition and determining composition were more difficult than in a three component bubble garnet system. Some of the considerations and problems in controlling composition were referred to in the discussions above on reactors and source materials. A major problem was simply changing transport rates. For example, if higher YCl_3 transport was desired the temperature would be raised in the YCl_3 zone. But this in turn would affect the temperature in the $GdCl_3$ zone so a revised temperature profile would have to be established for the entire vertical section.

Also in determining composition, convenient and rapid techniques for "ball-parking" the composition which are commonly used in three component systems such as GaYIG or GaErIG are not as reliable in this system. Nature of domains and presence of cracks in GaYIG films is sufficient to indicate the approximate film lattice constant and thus film composition. This is very useful for quickly deciding if the depositions are under proper control or if adjustments are necessary on the next run. But in GaYGdIG films "ball parking" the lattice constant does not unambigously assign a film composition. For example, a smaller a_f than desired may be due to either excess Y or excess Ga. Then other more exact but also more tedious characterization tools must be employed to assign the film composition (see Section 5). So, if composition adjustments are desired, the next run is either delayed for several days or adjustments are made that are based more on educated intuition than on science.

4.2.6 Composition determination. - Immediately following the deposition, the film is examined in a polarizing microscope equipped with coils to provide a magnetic bias field normal to the plane of the film. For the film composition and substrate orientations investigated, in zero bias field, if the domains are the vertical type the film is in tension and if the domains are the in-plane type the film is in compression or insufficient tension. Knowing the value of a_s, this immediately puts boundaries on the a_f (See the stress model discussion, P 64). If the film is in tension, presence or absence of cracks puts narrower boundaries on the film a_f. If the domains are vertical serpentine and/or bubble domains their size (width or diameter) is an indication of the magnetization (for constant film thickness), and of their probable usefulness as bubble films. Further indication of the approximate magnetization ($4\pi M$) is then obtained by applying a bias field and determining at what field the domains collapse.

Estimates of the gallium concentration are then quickly obtained by observing the "polarity" of the film magnetization, i.e., whether the net magnetization of a domain is parallel or antiparallel to the moment due to the tetrahedral iron sublattice (see pages 15 and 16). By observing the behavior of a Faraday effect domain pattern in response to an external field and comparing this behavior with that of a known or standard sample such as pure or lightly doped YIG, one can determine whether the net magnetization is

positive or negative. Since we want gallium concentrations such that $4\pi M > o$, this quickly indicates if the gallium concentration is in the desired range.

Let us briefly elaborate on the method for determining the sign or polarity of $4\pi M$. Recall from the discussion on page 15 that $4\pi M > o$ if $4\pi M_d > 4\pi M_a + 4\pi M_c$. The Faraday rotation in YGdIG is produced mainly by M_a (ref. 87) and so is little changed by Ga substitution. Consider the Faraday effect domain pattern in a reference sample such as a film of $Y_{2.4}Gd_{0.6}Ga_xFe_{5-x}O_{12}$ with $x < 1$ so that $4\pi M_d > 4\pi M_a + 4\pi M_c$, i.e., $4\pi M > o$. When an external field H, is applied perpendicular to the plane of the film the set of domains which have $4\pi M$ parallel to H will increase in size. Let us say for example, that the light domains increase in size. We then know that, for $4\pi M > o$, the light domains will expand when a field of the given polarity is applied. This indicates that $4\pi M_d$ in the light domains is parallel to H. The unknown sample is then placed in the microscope and the domain pattern observed without changing the polarizer/analyzer settings on the field polarity. If the light domains again expand as the field is increased this sample also has $4\pi M > o$. However, if the dark domains expand this means that $4\pi M < o$ since it is known that $4\pi M_d$ is parallel to H in the light domains. The fact that the dark domains expand indicates that $4\pi M$ is parallel to $4\pi M_a$, i.e., $4\pi M_a + 4\pi M_c > 4\pi M_d$ or $4\pi M < o$.

Simultaneous deposition on two substrates with slightly different a_s's can give fairly accurate film a_f information. For example, in one series we deposited films simultaneously on a SmGdGaG substrate with $a_s = 12.388$Å and a GdGaG substrate with $a_s = 12.383$Å. Films with a_f between 12.388Å and 12.383Å were in compression on GdGaG and in tension on the SmGdGaG, but not in sufficient tension to crack the films. Films with a_f slightly less than 12.383Å were in tension on both substrates and were generally cracked on the SmGdGaG. Films with a_f slightly greater than 12.388Å were in compression on both substrates.

These rapid but approximate techniques are commonly used to give instant feedback on the last deposition run and to provide guidelines for the next run. Selected films are subjected to more rigorous analysis and characterization.

Determination of film composition in $Y_{3-z}Gd_zGa_xFe_{5-x}O_{12}$ films directly by wet chemical analysis or spectroscopic analysis is hampered by the presence of gallium and/or gadolinium in the substrate. Consequently it has been expedient to estimate the composition from the values of other material parameters. There is considerable data in the open literature on the effect of diamagnetic substitutions, such as Ga, on the Neel temperature of the iron garnets. Therefore the value of T_N as measured by ferromagnetic resonance has been utilized to estimate the Ga content of the films. There are also published data on the variation of the lattice parameters with composition for the YGdIG, GaYIG and GaGdIG systems. Therefore if the Ga content is known from a T_N measurement and the film lattice constant is calculated from Δa data the Y:Gd ratio can also be calculated. Although this indirect approach does not provide high accuracy it has been successful in allowing achievement of good bubble films with approximate composition $Y_{2.4}Gd_{0.6}Ga_{1.0}Fe_{4.0}O_{12}$. The compositions of several films obtained in the manner just described are listed in table VIII.

TABLE VIII.– ESTIMATED COMPOSITIONS OF $Y_{3-z}Gd_zGa_xFe_{5-x}O_{12}$ FILMS

Sample	T_N(°C)	X	a_f(Å)	Z
2558	150	1.00	12.377	0.7
2602	133	1.15	12.379	0.82
2606Z4	143	1.05	12.371	0.5
2609Z3	153	0.98	12.378	0.6
2610	172	0.85	12.389	0.95
2614Z3	152	0.99	12.374	0.65

Another check on the approximate film composition is provided by the magnetization of the deposit. There is published data on $4\pi M$ vs Z and X in the system $Y_{3-z}Gd_zAl_x Fe_{5-x}O_{12}$ which is quite similar to the GaYGdIG system. Thus once X and Z are determined for a film, its approximate $4\pi M$ value can be obtained from the literature and compared with the measured value. Conversely from the measured $4\pi M$, the values of x and z can be determined from the literature data.

Towards the end of the program the difference in lattice constant between film and substrate $\Delta a = (a_s - a_f)$ was determined on certain samples using a double crystal x-ray diffractometer (see section on x-ray characterization). If the a_s is known, and stress effects are taken into account, the a_f can be obtained (ref. 51).

The lack of satisfactory, direct measurement of film composition slows the process of material development but does not prevent it. It has been possible with the indirect methods discussed above to estimate the composition well enough to make the deposition changes required to produce films with the desired properties for bubble domain materials. Obviously, the development of a rapid, accurate, nondestructive test for film composition is highly desirable.

4.2.7 Typical run sequence. - This section presents a short run sequence to illustrate typical run considerations, problems, evaluations and results. These runs were performed in the modified AG-2 reactor with the 3-in. diameter tubing. The deposition conditions for these runs are given in tables IX through XII.

4.2.7.1 Run 2611: The film was smooth and uncracked. The domains in the film were serpentines and bubbles that were approximately 9 μm in diameter with no bias field. However, the domain pattern was not uniform. This indicated that one of the chemical transport rates was not held constant during the deposition run. Also, the magnetic polarity of the film was negative, (see pages 15 and 16) indicating that the amount of gallium incorporated in the film was too high. It was also felt that the amount of gadolinium in the film might be too high to allow the desired stress in the film if the gallium was reduced.

4.2.7.2 Run 2612Z4: The gallium chloride transport was reduced from 2.77 gm/hr to 2.36 gm/hr and the $GdCl_3$ was lowered from 0.452 gm/hr to 0.250 gm/hr. The resulting film was also smooth and uncracked but the domains were not serpentine. Instead they were very large, irregular, vertical-type domains having very low magnetization. The magnetic polarity of this film was positive.

TABLE IX. – DEPOSITION CONDITIONS, AG-2, RUN 2611, AUGUST 18, 1971

Chemicals		YCl_3	$GaCl_3$	$FeCl_2$	$GdCl_3$
Weight before	=	105.063	103.717	248.6	119.384
Weight after	=	102.517	97.702	213.3	118.025
gm moved	=	2.546	6.015	35.3	1.359
gm/hr	=	0.848	2.77	11.7	0.452
Moles/hr	=				
cc/hr	=				
Temperature	=				

Chemicals	$GdCl_3$, $FeCl_2$, YCl_3	in 0900	out 1200 = 3 hr
Chemicals	$GaCl_3$	in 0930	out 1140 = 2 hr 10 min
Seeds		in 1035	out 1135 = 1 hr
Seed temp.	= 1175		

Gasses	Flow rates cc/min	Mole rates moles/hr
He vertical	10,370	
HCl vertical	~~0~~	
HCl over $GdCl_3$	170	
HCl over YCl_3	95	
HCl over $GaCl_3$	11.0 - 50	
He horizontal	4,725	
O_2 horizontal	43	

Mole Ratios

$FeCl_2$ +____ /YCl_3 +___ = _____ $FeCl_2/GaCl_3$ = _____

total Chemical/HCl = _____ total Chemical/O_2 = _____

HCl/O_2 = _____

TABLE X. – DEPOSITION CONDITIONS, AG-2, RUN 2612, AUGUST 18, 1971

Chemicals		YCl_3	$GaCl_3$	$FeCl_2$	$GdCl_3$
Weight before	=	106.285	117.680	239.5	117.990
Weight after	=	104.122	112.948	210.9	117.364
gm moved	=	2.163	4.732	28.6	0.626
gm/hr	=	0.865	2.36	11.5	0.250
Moles/hr	=				
cc/hr	=				
Temperature	=	1050°C	161°C	950°C	1015

Chemicals	$GdCl_3$, $FeCl_2$, YCl_3	in 1410	out 1640 = 2 hr 30 min
Chemicals	$GaCl_3$	in 1425	out 1625 = 2 hr
Seeds		in 1525	out 1625 = 1 hr
Seed temp.	= 1175		

Gasses	Flow rates cc/min	Mole rates moles/hr
He vertical	10,370	
HCl vertical	0	
HCl over $GdCl_3$	170	
HCl over YCl_3	95	
HCl over $GaCl_3$	48.8	
He horizontal	4,725	
O_2 horizontal	43	

Mole Ratios

$FeCl_2$ + ___ / YCl_3 + ___ = _____ $FeCl_2/GaCl_3$ = _____

total total total

Chemical/HCl = _____ Chemical/O_2 = _____

HCl/O_2 = _____

TABLE XI. – DEPOSITION CONDITIONS, AG-2, RUN 2613, AUGUST 19, 1971

Chemicals		YCl_3	$GaCl_3$	$FeCl_2$	$GaCl_3$
Weight before	=	108.846	112.952	248.9	117.311
Weight after	=	106.894	109.118	215.3	116.823
gm moved	=	1.952	3.834	33.6	0.488
gm/hr	=	0.618	1.870	10.7	0.153
Moles/hr	=				
cc/hr	=				
Temperature	=			950°C	

Chemicals	$GdCl_3$, $FeCl_2$, YCl_3	in 0930	out 1240 = 3 hr 10 min
Chemicals	$GaCl_3$	in 1000	out 1205 = 2 hr 5 min
Seeds		in 1100	out 1200 = 1 hr
Seed temp.	= 1175°C		

Gasses	Flow rates cc/min	Mole rates moles/hr
He vertical	10, 870	
HCl vertical	~~0~~	
HCl over $GdCl_3$	145	
HCl over YCl_3	95	
HCl over $GaCl_3$	46.6	
He horizontal	4.725	
O_2 horizontal	43	

Mole Ratios

$FeCl_2$ + ___ / YCl_3 + ___ = _____ $FeCl_2/GaCl_3$ = _____

total total total

Chemical/HCl = _____ Chemical/O_2 = _____

HCl/O_2 = _____

TABLE XII. – DEPOSITION CONDITIONS, AG-2, RUN 2614, AUGUST 19, 1971

Chemicals		YCl_3	$GaCl_3$	$FeCl_2$	$GdCl_3$
Weight before	=	108.398	109.118	248.9	116.809
Weight after	=	106.281	104.928	218.6	116.334
gm moved	=	2.117	4.190	30.3	0.475
gm/hr	=	0.793	1.62	11.2	0.178
Moles/hr	=	4.06×10^{-3}	9.20×10^{-3}	8.83×10^{-2}	6.75×10^{-4}
cc/hr	=				
Temperature	=	1055°C	162°C	950°C	972°C

Chemicals	$GdCl_3$, YCl_3, $FeCl_2$	in 1400	out 1640 = 2 hr 40 min
Chemicals	$GaCl_3$	in 1430	out 1620 = 1 hr 50 min
Seeds		in 1520	out 1620 = 1 hr
Seed temp.	= 1175°C		

Gasses	Flow Rates cc/min	Mole Rates moles/hr
He vertical	10,370	
HCl vertical	~~0~~	
HCl over $GdCl_3$	170	
HCl over YCl_3	95	
HCl over $GaCl_3$	48.8	
He horizontal	4,725	
O_2 horizontal	43	

Mole Ratios

$FeCl_2$ +__ /YCl_3 +__ = _____ $FeCl_2/GaCl_3$ = 9.59:1

total total
Chemical/HCl = _____ total Chemical/O_2 = _____

HCl/O_2 = _____

These results indicated that we were close to the desired composition and that all of the transport rates except the $GaCl_3$ should be held constant. The gallium concentration in the film was still too high and had to be lowered.

4.2.7.3 Run 2613Z4: The $GaCl_3$ transport was lowered from 2.36 gm/hr to 1.87 gm/hr for this run but unfortunately all of the other chemical transports also dropped off fractionally during the run due to heating problems in the vertical section of the reactor.

The resulting film deposit was smooth and the domains were large bubbles approximately 8 μm in diameter, but the film was badly cracked due to the mismatch between the film and the substrate. The mismatch had been accentuated by the decrease in the amount of gadolinium in the system.

4.2.7.4 Run 2614: Control of the heat zones in the vertical section was reestablished and then slight adjustments were made on both the $GaCl_3$ and the $GdCl_3$ for this run.

In order to increase the lattice constant of the film and thereby reduce the stress on the film, the $GdCl_3$ transport was increased from 0.153 gm/hr to 0.178 gm/hr. In conjunction with this change the $GaCl_3$ transport rate was lowered from 1.87 gm/hr to 1.62 gm/hr in an attempt to prevent the magnetization of the sample from dropping excessively. The film from this run was very smooth with only a few small cracks at the edge. The domains were bubbles 10.5 μm in diameter without an applied bias field. Areas of the sample were isolated without cracks to be used for bubble-propagation studies.

5.0 MATERIALS CHARACTERIZATION

5.1 Introduction

The characterization of epitaxial films is more difficult than that of bulk samples of the same material. The two main sources of this difficulty are: (1) the thinness ($\sim 4\mu m$) and the small volume of the film, and (2) the presence of the substrate. The problem of adequately characterizing a thin epitaxial layer on a substrate whose crystal structure, chemical constituents, and physical properties are similar or identical to that of the film is discussed in ref. 5. Fortunately, in the case of a ferrimagnetic film on a paramagnetic or diamagnetic substrate, the magnetic characteristics of the two layers are quite different and the magnetic properties of the film can usually be distinguished from those of the substrate. Therefore, epitaxial films of ferrimagnetic oxides, such as iron garnets, are most readily characterized in terms of their magnetic properties. From these magnetic parameters certain of their chemical and physical properties can be inferred as well.

In addition, for iron garnet films grown on rare-earth gallium garnet substrates, certain physical parameters of the film can be determined by optical and X-ray techniques.

The magnetic and physical parameters that determine the bubble-domain properties of a material have been presented in Section 2.0, Introduction. Those properties that have been investigated on this program are listed in table XIII along with the techniques used to determine them. In some cases more than one method has been employed to evaluate a particular parameter. The technique that has so far proved most satisfactory for the epitaxial films is listed first in each case followed by alternate approaches that are enclosed in brackets. The bubble-domain technology has stimulated the development of novel techniques for evaluating some of the magnetic parameters of the material. The basic approach has been to measure certain domain characteristics and then determine the magnetic parameters from theoretical relationships between the domain properties and the material properties. An example of such a method is the measurement of $4\pi M$ and ℓ from the static collapse condition for bubble domains.

The various parameters, measurement techniques, and typical results on the film materials will be discussed individually in the following paragraphs. At the completion of this discussion, a tabulation of data on a representative CVD bubble-domain film of GaYGdIG is presented. There is also a paragraph on thermal expansion measurements on potential substrate garnets and three paragraphs that are more general than those dealing with the evaluation of specific material parameters. These paragraphs cover the film-substrate matching requirements, the effect of heat treatment on film properties, and bubble-domain propagation characteristics.

TABLE XIII. – BUBBLE-DOMAIN FILM PARAMETERS

Property	Symbol	Measurement Technique
Film/substrate crystal quality		X-ray diffraction topography
Film/substrate lattice parameter difference and film lattice parameter	Δa, a_f	X-ray diffraction rocking curves—double-crystal diffractometer
Film thickness	h	Infrared interference (metallographic cross-section.)
Composition	Values of x and z in $Y_{3-z}Gd_zGa_xFe_{5-x}O_{12}$	Determination from data on T_N, T_{comp}, $4\pi M$, a_f, Δa.
Domain structure		Faraday effect—polarizing microscope
Bubble diameter (vs field and temperature)	d (H, T)	Faraday effect domain observations—polarizing microscope with field coils and variable temperature stage
Magnetization	$4\pi M$	Static collapse of bubbles (Vibrating sample magnetometer) (Ferromagnetic resonance)
Characteristic length	ℓ	Static collapse of bubbles
Wall energy	σ_w	Calculation from $\sigma_w = 4\pi M^2 \ell$
Internal field (bubble stability condition)	$H_A - 4\pi M$	Ferromagnetic resonance
Neel temperature and compensation temperature	T_N, T_{comp}	Variable temperature ferromagnetic resonance and domain observations
Anistropy field	H_A	Ferromagnetic resonance (Domain observations with in-plane magnetic field)
Wall coercive force	H_c	Bubble repulsion—equilibrium spacing
Domain wall mobility	μ_w	Dynamic collapse of bubbles

5.2 Thermal Expansion

Generation of stress in homoepitaxial thin films can influence the physical characteristics of the film. In the case of certain magnetic garnet thin films, in-plane stress has the effect of inducing uniaxial magnetic anisotropy. It has been shown that the state of stress is markedly affected by the lattice mismatch between the substrate and the film (ref. 48 and Appendix), for the case in which the mismatch is very small, as for the garnets. A less variable but still significant parameter in stress generation is the difference in thermal expansion between the film and the substrate. As the composite cools from deposition temperature to room temperature, the differential contraction causes the film to be strained. (The substrate is thick enough that it can be considered to be essentially nonyielding.)

Data on thermal expansion of several garnets was generated by Geller, et al. (ref. 56), using X-ray diffraction techniques. The samples were prepared by chemical reaction between mixed metal oxide powders of suitable proportions. From these data (shown in figure 21), it was apparent that, in general, the YIG material had greater expansivity than did any of the nonmagnetic samples. This relative expansivity should lead to placing the epitaxial YIG film in tension when cooled. Since this program is concerned with films other than just YIG and with nonmagnetic garnet materials not investigated by Geller (ref. 56), an effort was undertaken to measure the coefficient of thermal expansion (α) for the garnets of interest here. These measurements were made at Atomics International under Autonetics direction.

5.2.1 Apparatus. – A quartz dilatometer, employing a linear variable differential transformer (LVDT) as tne linear displacement transducer, was used (see figure 22). The quartz tube normally used in this apparatus is nominally 0.125 in. i.d. by approximately 14 in. long. One-eighth diameter by 2-in. length is the normal sample size used. The sample is placed in the bottom of the quartz tube and its expansion is transmitted to the LVDT through an 0.125-in. diameter quartz push rod.

Because of the irregular shapes of the garnet samples, however, the quartz tube was modified to accept either the boule or disk samples. For the boules the diameter of the quartz tube was enlarged to about 0.5 in. at the bottom 1.5 in. of the tube, and the expansion along the axial length of the boule was measured. For the disk samples, the bottom 1 in. of the quartz tube was enlarged to about 0.5 in. diameter and the bottom was sealed with a 0.25-in. thick quartz rod. A narrow slot cut in the bottom allowed the sample disk to stand on its edge so that the expansion across its diameter could be measured. A small opening in either quartz tube located approximately midway along the length of the samples was used to insert a chromel-alumel thermocouple into the tube, so that the measuring junction was nearly in contact with the sample. To ensure uniform temperature in the sample and to minimize temperature differential between sample and thermocouple, dry helium gas was introduced at the top of the quartz tube and was allowed to flow out at the bottom. An electric muffle furnace was used, with a massive heat sink surrounding the quartz tube, to give the furnace added thermal stability.

The LVDT was calibrated with a micrometer with the dial reading directly to 50 μ in. Readings are estimated to 25 μ in. The micrometer was in turn calibrated at the Atomics International instrument laboratory against an electronic gauge,

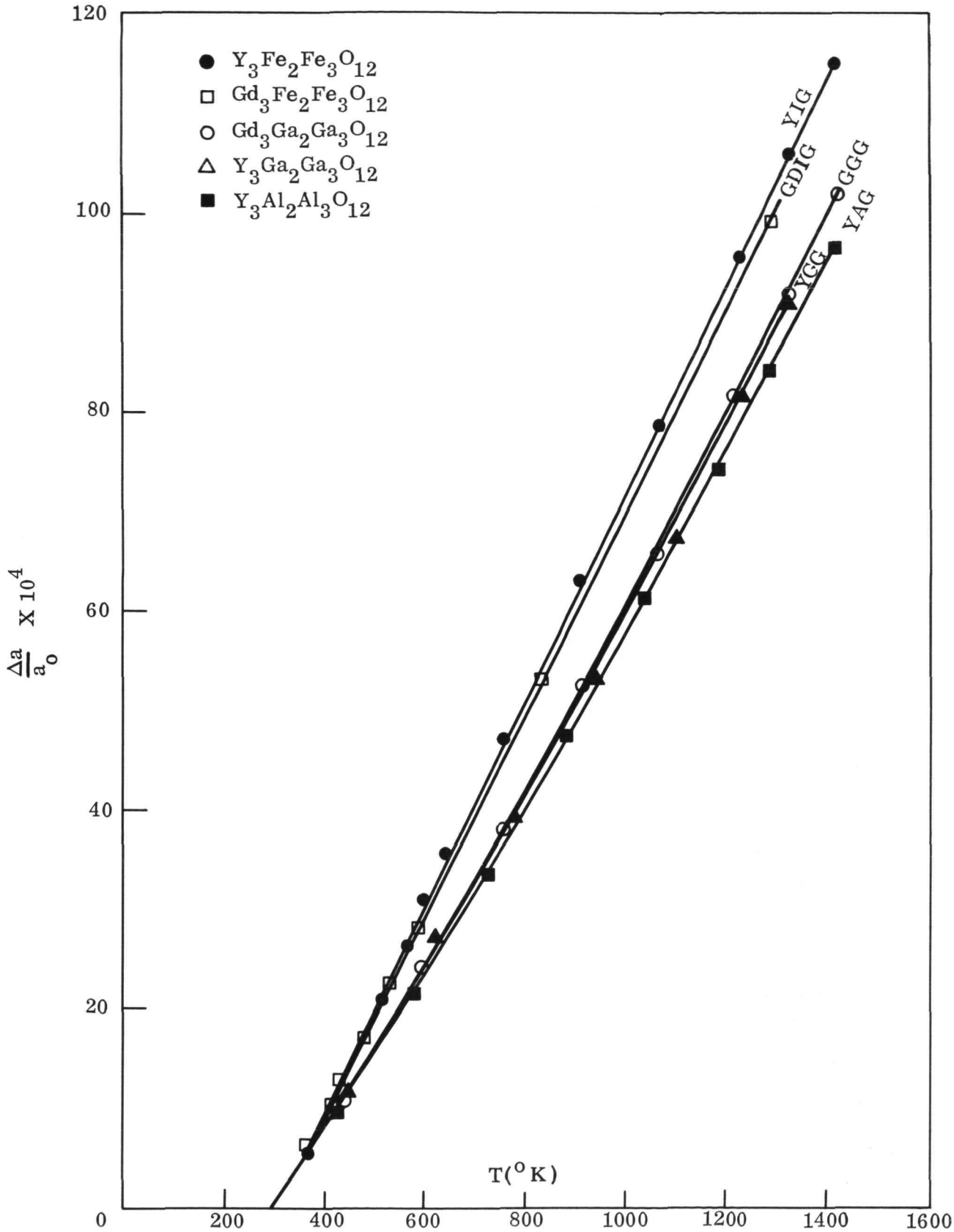

Figure 21. $\Delta a_o/a_o$ vs Absolute Temperature

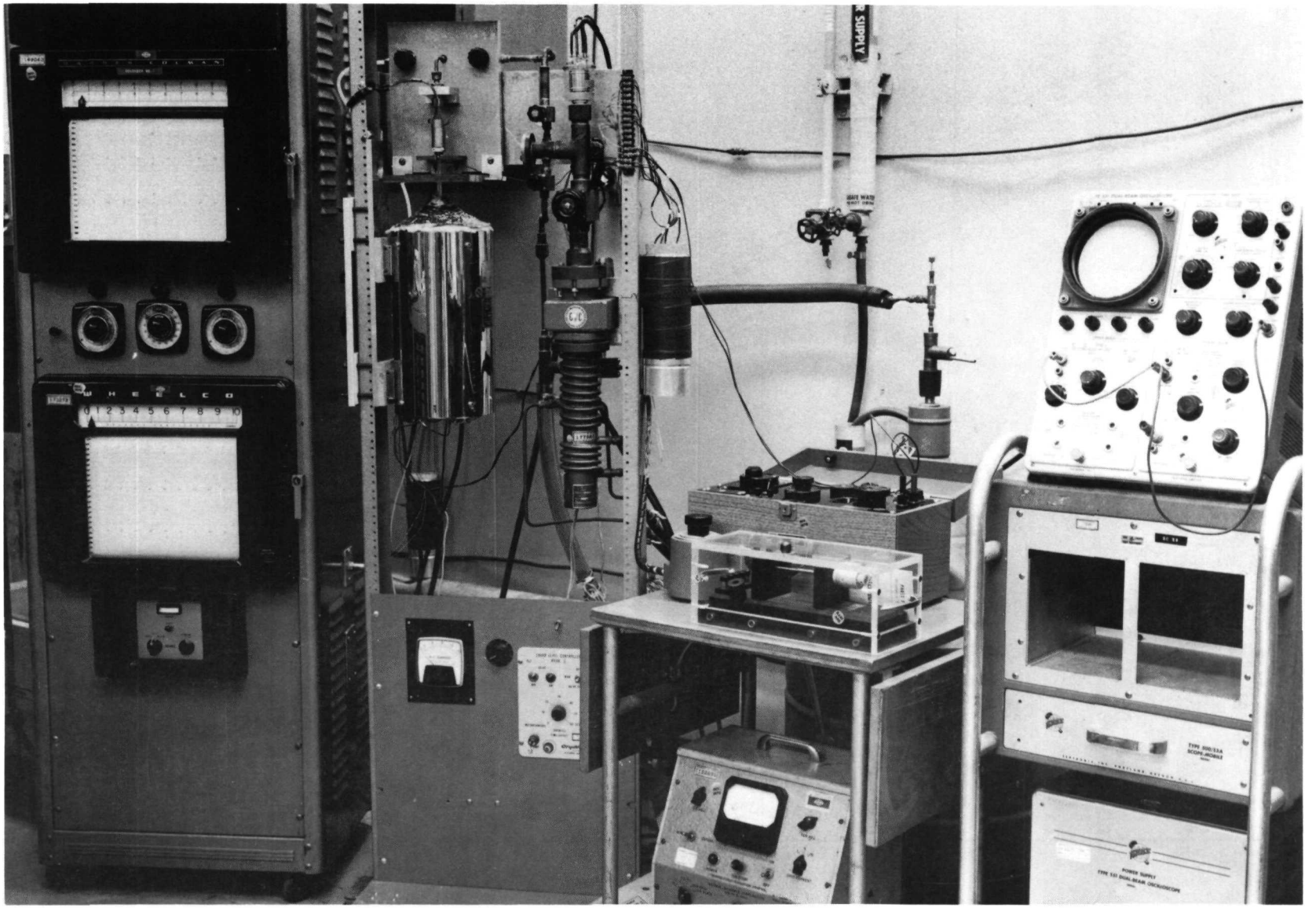

Figure 22. – Thermal Expansion Apparatus

accurate to < 10 μ in. Before expansion measurements were made on the garnet samples, a quartz-on-quartz run was made using a procedure identical to those used in the garnet runs to determine the correction required for the expansion differential between the quartz tube and quartz push rod. This correction (maximum of +45 μ in. at about 600°C), and the correction for quartz expansion (equivalent to sample length) were applied to all measurements.

The sample length at room temperature was measured with a micrometer reading directly to 0.0001 in. Expansion measurements were taken at each temperature after allowing the sample temperature and LVDT output to stabilize. Heating rate of about 4°/min was used between measurements.

The uncertainty in the measurements is due to the following:

Micrometer accuracy	±50 μ in.
Recorder accuracy	±50 μ in.
Temperature differential correction (quartz tube vs rod)	±10 μ in.
Quartz correction	±4 percent of ΔL

The linear thermal expansion data of quartz was obtained from the TPRC data handbook (ref. 57) and the ±4-percent uncertainty represents the uncertainty due to the spread in the literature values reported in the handbook. Temperature readings are believed accurate to < ±5°C.

5.2.2 Thermal expansion data. - The results of the measurements made on seven garnet samples are given in tables XIV through XX. It appears that the expansion curves of all of the samples might be represented by the average for the samples, since the scatter is within experimental error. An anomalous data point at 484°C, for $Sm_{1.88}Gd_{1.12}Ga_5O_{12}$ is believed to be due either to a momentary electrical disturbance or mechanical vibration (earth tremor?) since the LVDT output was found to be very erratic just before and after the reading was taken. A data point for $Nd_3Ga_5O_{12}$ at 932°C, which falls below the curve, is believed to be due to shifting of the sample. These data can be summarized best by expressing the coefficient of expansion averaged over the range between room temperature and about 930°C. The calculation for this is based on the total temperature span and the total expansion for each crystal. Attention to the data at intermediate temperatures does not lead to any differing conclusion. The average coefficients are shown in table XXI. The standard deviation ($\pm 0.16 \times 10^{-6}$) derived from these data is qualitatively consistent with the uncertainty placed on the individual values of α, which averages $\pm 0.21 \times 10^{-6}$.

From these data it is not apparent that there is a clear-cut trend in α with composition. Whatever change in α may exist, it is small enough to be obscured by experimental uncertainty. It can be concluded, therefore, that the variations in α with compositional changes are less than 2 percent within the compositional region investigated, which is important new information. To obtain more definitive data, it will be necessary to achieve a higher measurement precision in measurement techniques.

TABLE XIV. – THERMAL EXPANSION DATA FOR $Gd_3Ga_5O_{12}$

T (°C)	$\Delta L \times 10^3$ (in.)	Expansion (percent)
25	0	0
238	1.591	0.166
410	2.961	0.308
595	4.537	0.472
780	6.097	0.634
934	7.374	0.767
Uncertainty at 934° = ±1.7 percent L = 0.9610 in. at room temperature		

TABLE XV. – THERMAL EXPANSION DATA FOR $Gd_3Ga_5O_{12}$

T (°C)	$\Delta L \times 10^3$ (in.)	Expansion (percent)
25	0	0
204	1.559	0.142
334	2.792	0.254
478	4.154	0.378
614	5.449	0.495
768	6.959	0.633
938	8.638	0.785
Uncertainty at 938° = ±1.5 percent L = 1.1002 in. at room temperature		

TABLE XVI. – THERMAL EXPANSION DATA FOR $Sm_{0.48}Gd_{2.52}Ga_5O_{12}$

T (°C)	$\Delta L \times 10^3$ (in.)	Expansion (percent)
26	0	0
195	0.925	0.119
328	1.796	0.232
456	2.623	0.338
610	3.683	0.475
760	4.664	0.602
930	5.790	0.747
Uncertainty at 930° = ±2.2 percent L = 0.7752 in. at room temperature		

TABLE XVII. – THERMAL EXPANSION DATA FOR $Sm_{1.88}Gd_{1.12}Ga_5O_{12}$

T (°C)	$\Delta L \times 10^3$ (in.)	Expansion (percent)
33	0	0
207	0.686	0.135
309	1.145	0.225
484	2.120	0.417
619	2.534	0.498
766	3.296	0.648
934	4.017	0.790
Uncertainty at 934° = ±3.0 percent L = 0.5086 in. at room temperature Note: Initial temperature was 8° above ambient temperature.		

TABLE XVIII. – THERMAL EXPANSION DATA FOR $Nd_{1.76}Gd_{1.24}Ga_5O_{12}$

T (°C)	$\Delta L \times 10^3$ (in.)	Expansion (percent)
26	0	0
209	0.630	0.145
328	1.061	0.245
470	1.587	0.366
619	2.175	0.501
774	2.767	0.638
939	3.391	0.782

Uncertainty at 939° = ±3.5 percent
L = 4337 in. at room temperature

TABLE XIX. – THERMAL EXPANSION DATA FOR $Nd_3Ga_5O_{12}$

T (°C)	$\Delta L \times 10^3$ (in.)	Expansion (percent)
24	0	0
254	1.091	0.172
341	1.566	0.248
452	2.237	0.354
620	3.105	0.491
761	3.916	0.619
932	4.722	0.747 *0.785

Uncertainty at 932° = ±2.6 percent
L = 0.6325 in. at room temperature

*Extrapolated from data at lower temperature

TABLE XX. – THERMAL EXPANSION DATA FOR $Sm_3Ga_5O_{12}$

T (°C)	$\Delta L \times 10^3$ (in.)	Expansion (percent)
25	0	0
192	0.743	0.123
320	1.394	0.230
472	2.219	0.367
614	2.960	0.489
765	3.736	0.617
928	4.595	0.759
Uncertainty at 928° = ±2.7 percent L = 0.6054 in. at room temperature		

TABLE XXI. – AVERAGE THERMAL EXPANSION COEFFICIENTS

$Gd_3Ga_5O_{12}$	8.60×10^{-6}
$Sm_{0.48}Gd_{2.52}Ga_5O_{12}$	8.25×10^{-6}
$Sm_{1.88}Gd_{1.12}Ga_5O_{12}$	8.69×10^{-6}
$Sm_3Ga_5O_{12}$	8.39×10^{-6}
$Nd_{1.76}Gd_{1.24}Ga_5O_{12}$	8.58×10^{-6}
$Nd_3Ga_5O_{12}$	8.67×10^{-6}

Average of all values: ($8.53 \times 10^{-6}/^{o}C$)

Of greater concern is the discrepancy between the data presented here and that published earlier. Geller, et al. (ref. 56), reported data for $Gd_3Ga_5O_{12}$ that yields $\alpha = 9.0 \times 10^{-6}$ over the same temperature range for which we obtained 8.53×10^{-6} (see preceding paragraphs), or a discrepancy slightly in excess of 5 percent. It is not known yet whether this discrepancy is due to instrumental effects (since the methods were quite different in Geller's work and ours), or is due to real material differences. Work is underway currently to improve accuracy and precision of thermal expansion measurements, and to resolve this discrepancy.

5.3 Stress Model

This brief subsection is included in this part of the report because the film/substrate mismatch characteristics can be evaluated by comparing domain observations and X-ray measurements of the strained lattice spacings with the predictions of the stress model.

In epitaxial garnet films grown by CVD, the uniaxial magnetic anisotropy required for bubble-domain formation is stress-induced (ref. 22). The stress results from the film-substrate lattice constant difference, $\Delta a = a_s - a_f$, and the thermal expansion difference, $\Delta\alpha = \alpha_s - \alpha_f$. To obtain uncrazed deposits with suitable anisotropy, it is necessary to have a means of predicting and controlling both the sign and the magnitude of the film stress.

A simple physical model has been developed, which predicts the film stress from a knowledge of $\Delta\alpha$ and the room temperature Δa. The stress model is described in ref. 48, which is included as the Appendix to this report. This model has been successfully used to develop several useful epitaxial garnet combinations for bubble-domain applications. One of these combinations, $Y_{3-z}Gd_zGa_xFe_{5-x}O_{12}/Gd_3Ga_5O_{12}$ (GaYGdIG/GdGaG), is the material studied on this contract. By proper selection of the sign and magnitude of Δa and $\Delta\alpha$, it is possible to place the garnet films in either tension or compression and to eliminate film crazing. Experimental results on domain structure, anisotropy, and crazing in bubble-domain compositions of iron garnet films on rare-earth gallium garnet substrates are consistent with the model. Examples of such results for films of GaYGdIG on various substrates are presented in Section 5-7. Since the discussions on stress and anisotropy in CVD magnetic oxide films are spread throughout several papers (refs. 5, 22, 48, 51, and 58), the results germane to bubble-domain formation in GaYGdIG films are summarized below:

(1) Epitaxial magnetic films are normally in a state of mechanical stress, σ, due to mismatch between the lattice constants and the thermal expansions of the film and substrate.

(2) If the film is magnetostrictive, this stress produces a uniaxial magnetic anisotropy that is superimposed on the bulk, unstrained anisotropy.

(3) For a material with negative magnetostriction constants (λ_{100}, $\lambda_{111} < 0$) the magnetostrictive contribution tends to make the normal-to-the-film plane an easy axis if the film is in tension ($\sigma > 0$) and a hard axis if the

film is in compression ($\sigma < 0$). The magnetostrictive effect can therefore be used to provide a uniaxial magnetic anisotropy in materials whose crystal structure is nearly cubic.

(4) For iron garnet films on rare-earth gallium garnet substrates the film stress is linearly dependent on Δa and independent of $\Delta\alpha$ for small values of Δa (~ 0.05 Å), and $\Delta\alpha$ ($\sim 1 - 2 \times 10^{-6}$). Under these conditions the films are in tension for $\Delta a > 0$ and in compression for $\Delta a < 0$.

(5) Since GaYGdIG has negative magnetostriction the films must be in tension to support bubble domains.

(6) For films ~ 5-μm thick in tension, crazing usually occurs if $\Delta a > +0.010$ Å. Therefore this value of Δa represents a practical limit for obtaining uncrazed bubble domain films in GaYGdIG.

5.4 Film/Substrate Crystal Quality

5.4.1 X-ray diffraction topography. - X-ray diffraction topography provides a means of obtaining photographic images of crystalline materials. The resolution is comparable to that seen in optical micrographs. However, since X-rays have much shorter wavelength than visible light and since topographic images are produced by diffraction of the X-rays, topography is considerably more sensitive to small strains than is optical microscopy. The contrast in X-ray diffraction topographs is a manifestation of the deviations of the atomic arrangement of the specimen from the perfectly periodic arrangement of an ideal crystal.

A number of different topographic techniques have been developed (ref. 59). These techniques share certain common features. An X-ray beam is incident on the specimen. Usually the specimen is a single crystal and is oriented to satisfy the conditions for diffraction from a particular set of atomic planes having Miller indices ($hk\ell$). The diffracted beam is recorded on a photographic film or plate to form the topographic image. Assuming the kinematical diffraction theory to hold, a perfect crystal would give rise to a topograph having a uniformly grey appearance. The contrast effects observed in topographs are attributable to the presence of crystal imperfections in the specimen.

5.4.2 Experimental procedure and results. -

5.4.2.1 Lang technique: One of the best known topographic methods is the one developed by Lang (ref. 60). The apparatus is shown schematically in figure 23. The X-ray beam from a geometrically small source is collimated by slit S_1 and impinges upon the specimen crystal. $K\alpha$ characteristic radiation is generally used and the specimen is set to diffract this radiation in transmission; i.e., the incident beam enters one face of the wafer-like specimen and the diffracted beam exits through

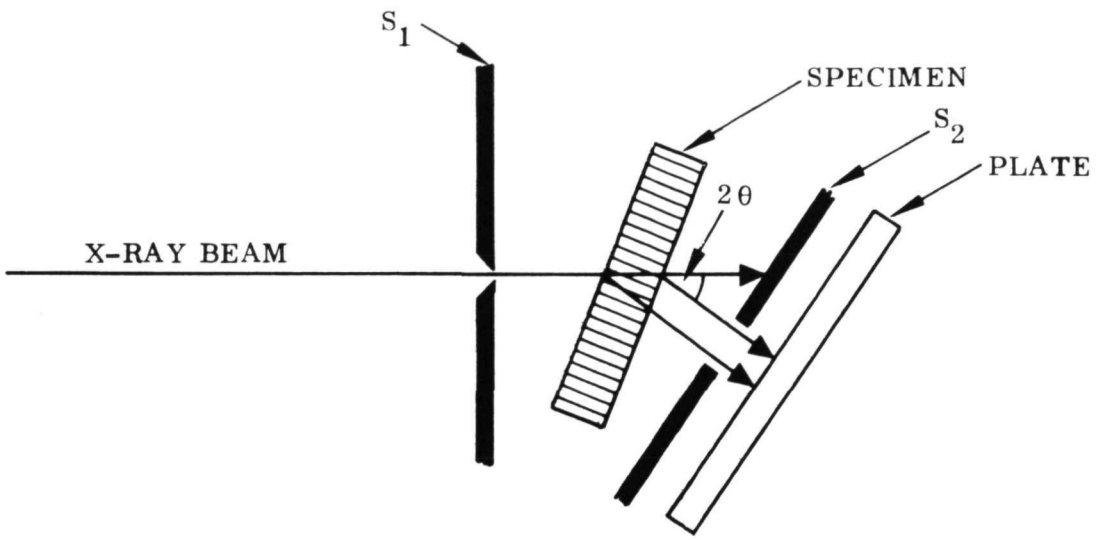

Figure 23. – Lang Topographic Technique

the opposite face. In figure 23, the diffracting planes are perpendicular to the specimen faces. This is the symmetric case in which the incident and the diffracted beams make equal angles with the specimen faces.

In order to limit absorption, and, therefore, have sufficient intensity in the emergent diffracted beam, it is necessary that the specimen be thin and that penetrating radiation be employed. For AgKα X-rays, GdGaG wafers 100 μm in thickness are suitable, the absorption factor being about e^{-2}.

The Kα spectral line is a doublet. In order to achieve high resolution, slit S_1 provides a high degree of collimation. This makes it possible to set the specimen so that the (hkℓ) planes diffract the stronger Kα_1 component but not the Kα_2.

The diffracted beam is recorded on the photographic plate. Since the X-rays do not provide any magnification (there is usually some geometrical foreshortening), the plate must be very fine grained to allow for subsequent magnification by optical means. The beam that is incident on the crystal is very narrow. To record a topographic image from a large area of the specimen, the Lang camera includes a mechanism for translation of specimen and plate. Slit S_2 between specimen and plate prevents the transmitted primary beam from obliterating the topographic image during scanning. With fine-grained plates, exposure times for thin GdGaG wafers are about 1 hr/mm of scan.

Figures 24 to 28 are examples of Lang topographs of garnet substrate crystals (cut from three different boules, designated A, B and C.) All of these specimens were wafers about 100-μm thick and all topographs were made with AgKα_1 radiation using (hkℓ) diffracting planes perpendicular to the wafer surface. With the exception of figure 28, the wafers were all (111) oriented slices cut across the boule axis. The wafer of figure 28 was a (210) slice cut nearly parallel to the boule axis.

All of the substrate wafers thus far examined by the Lang method exhibit distinctive band structures similar to those seen in figures 24 to 28. The bands approximate conic sections. At low magnifications the bands appear to be rather coarse with one or two bands per millimeter. At higher magnifications, however, it is seen that a finer band structure exists having 10 to 20 bands per millimeter. The coarse bands seen at low magnifications are due to fluctuations in the density of fine bands.

In addition to the band structure, the transverse (across-boule axis) slices also exhibit central cores. In some wafers, such as the one shown in figure 24, the cores have a pronounced three-lobed form, while other wafers have nearly circular or elliptical cores. Other features also appear in the topographs. Some of these are artifacts (such as the fine emulsion scratches at A and the ghost reflections at B in figure 24), but most represent various types of crystal defects. Referring again to figure 24, the dark line at C is probably a scratch on the crystal surface, the large spot at D is probably an inclusion, while the group of small spots near E may be dislocations. While the appearance of these other defects varies from one specimen to another, the core and band structures are common to all. Therefore, attention was focused on developing techniques suitable for investigation of the cores and bands in the substrates and their effects on CVD films. Analysis of other defects was deferred.

The Lang method is an excellent technique for observing defects in the interiors of crystals. In the present investigation, however, it has some drawbacks. The principal shortcoming is the necessity of using extremely thin wafers. These are somewhat difficult to prepare and are extremely fragile. The wafer used for the topograph in figure 24 was accidentally broken several times and the figure shows only a fragment of the original specimen. In addition to fragility, their thinness renders such wafers unsuitable for use as seeds in CVD.

5.4.2.2 Scanning reflection technique: To overcome the difficulties associated with the use of thin wafers, reflection topography may be employed. Figure 29 illustrates a method for obtaining scanning reflection topographs. The Lang apparatus is used but the specimen is oriented in such a way that both the incident beam and the emergent diffracted beam pass through the same face. A symmetric reflection is shown in the figure; i.e., the diffracting planes are parallel to the specimen surface. Slit S-2 is no longer necessary since the primary beam does not strike the plate.

In reflection topography thick specimens may be used. However, due to absorption, only the volume of crystal lying near the irradiated surface contributes to the topographic image. The effective volume may be very thin particularly since it is generally advantageous to use less penetrating radiation such as CuKα or FeKα. Although only the top few microns of the specimen may be observable, this region is of paramount interest in the study of epitaxy.

Figures 30 to 34 are scanning reflection topographs of the same specimens shown in figures 24 to 28. All were obtained using symmetric reflections with FeKα_1

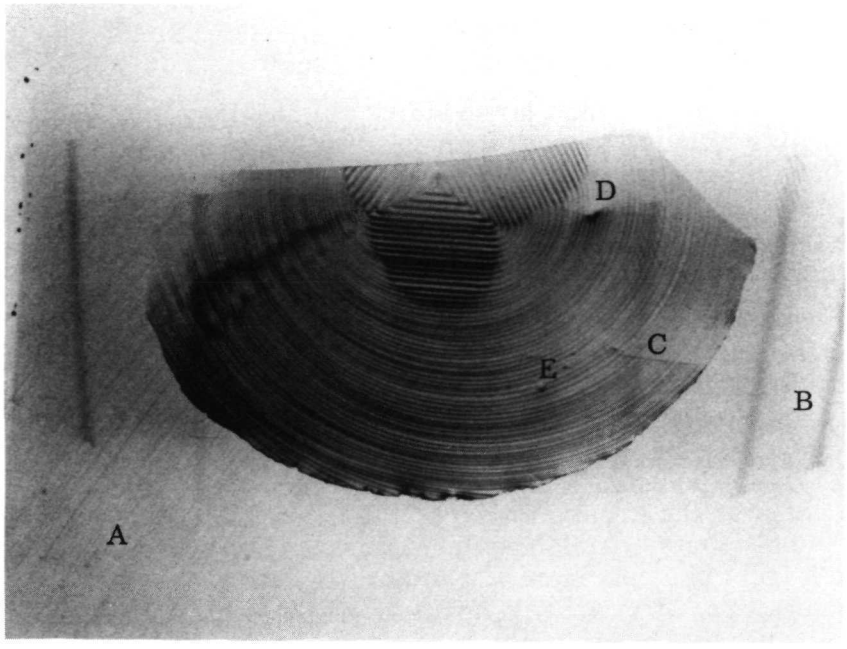

Figure 24. – Lang Transmission Topograph of Thin (111) GdGaG Wafer; Boule A, AgKα_1 Radiation, (044) Reflection, 7.3X Magnification

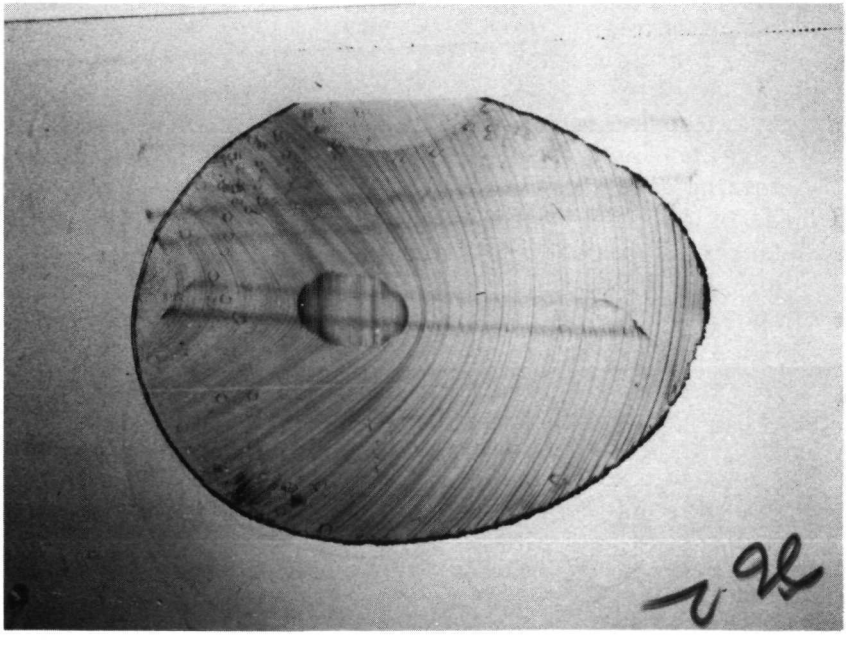

Figure 25. – Lang Transmission Topograph of Thin (111) GdGaG Wafer; Boule B, AgKα_1 Radiation, ($\bar{4}22$) Reflection, 3.5X Magnification

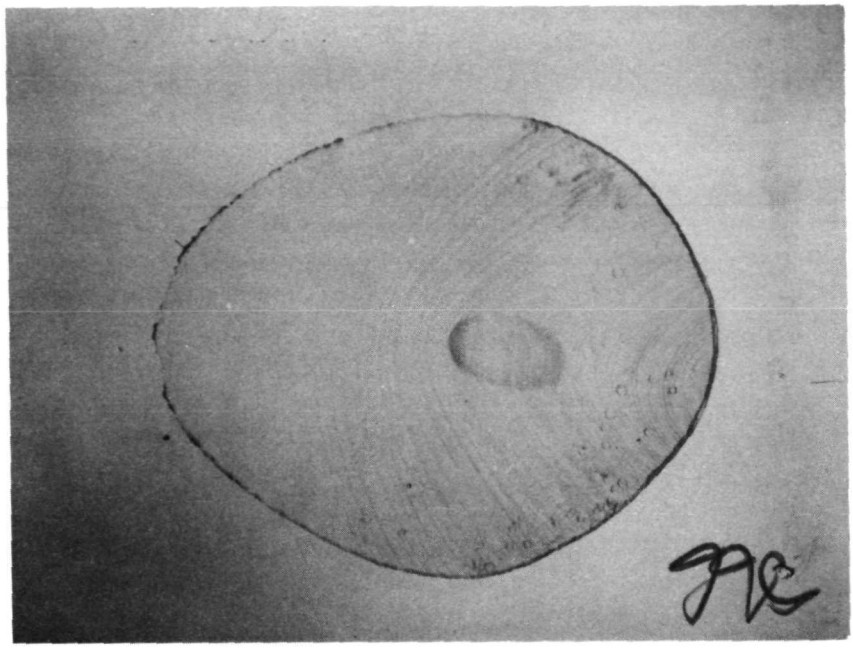

Figure 26. – Lang Transmission Topograph of Thin (111) GdGaG Wafer; Boule B AgKα_1 Radiation ($4\bar{2}\bar{2}$) Reflection, 3.8X Magnification. Slice adjacent to that shown in figure 25.

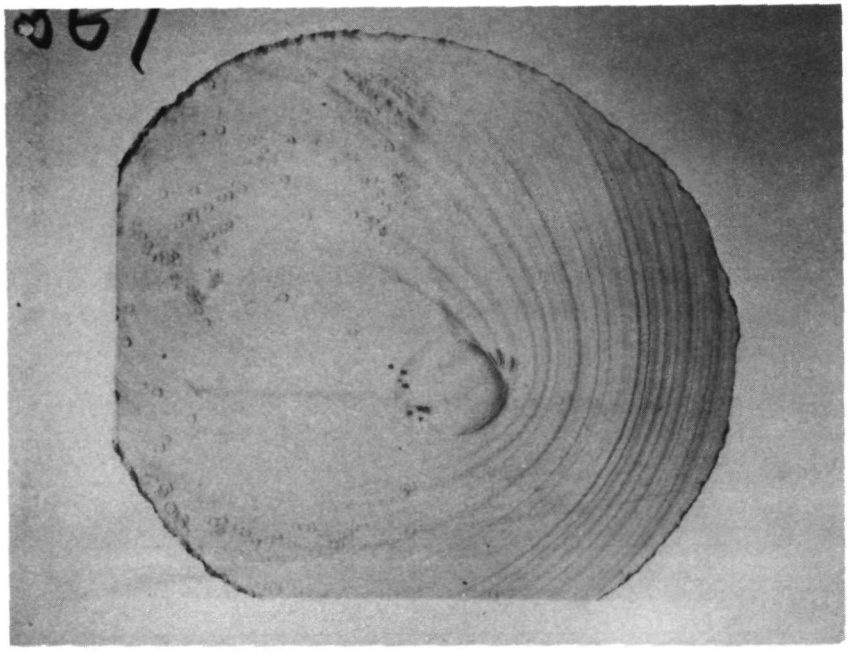

Figure 27. – Lang Transmission Topograph of Thin (111) GdGaG Wafer; Boule C AgKα_1 Radiation ($\bar{4}22$) Reflection, 3.9X Magnification

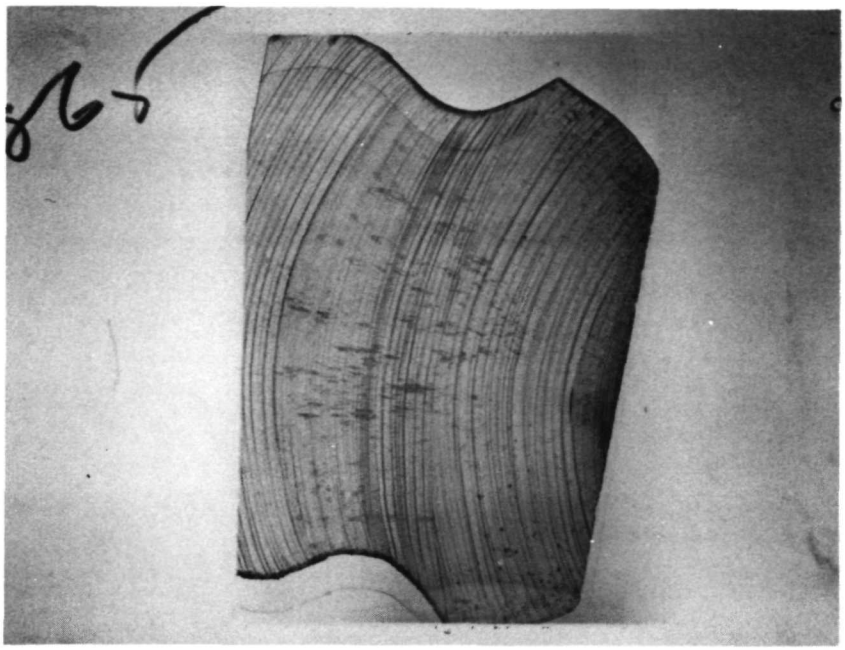

Figure 28. – Lang Transmission Topograph of Thin (012) GdGaG Wafer; Boule C
AgKα_1 Radiation (24$\bar{2}$) Reflection, 3.5X Magnification

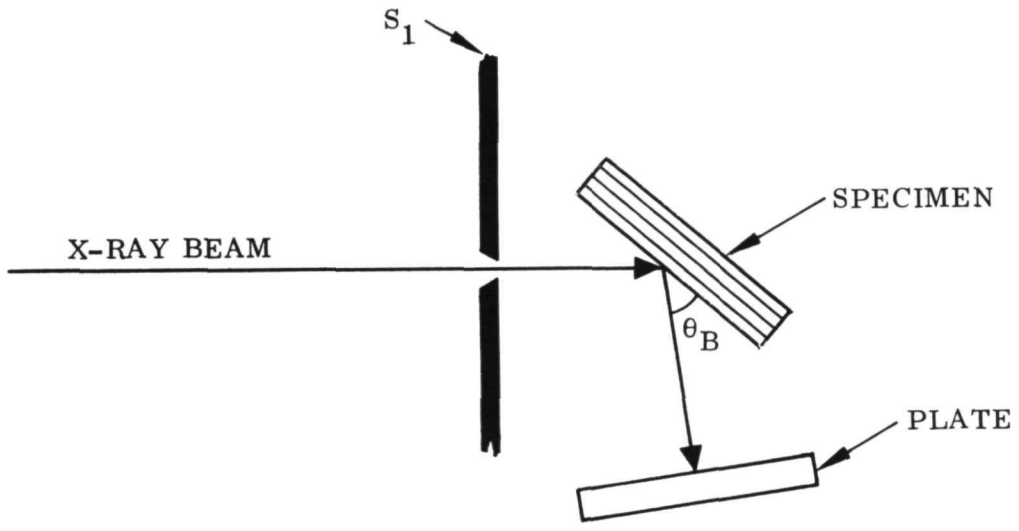

Figure 29. – Reflection Topography on Lang Camera

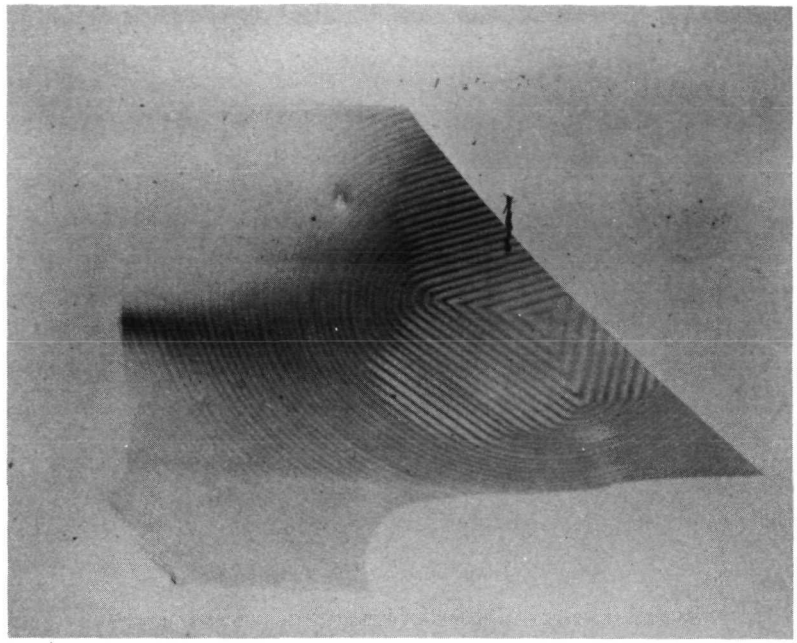

Figure 30. — Scanning Reflection Topograph of Thin (111) GdGaG Wafer; Boule A, CuKα_1 Radiation, (888) Reflection, 12X Magnification

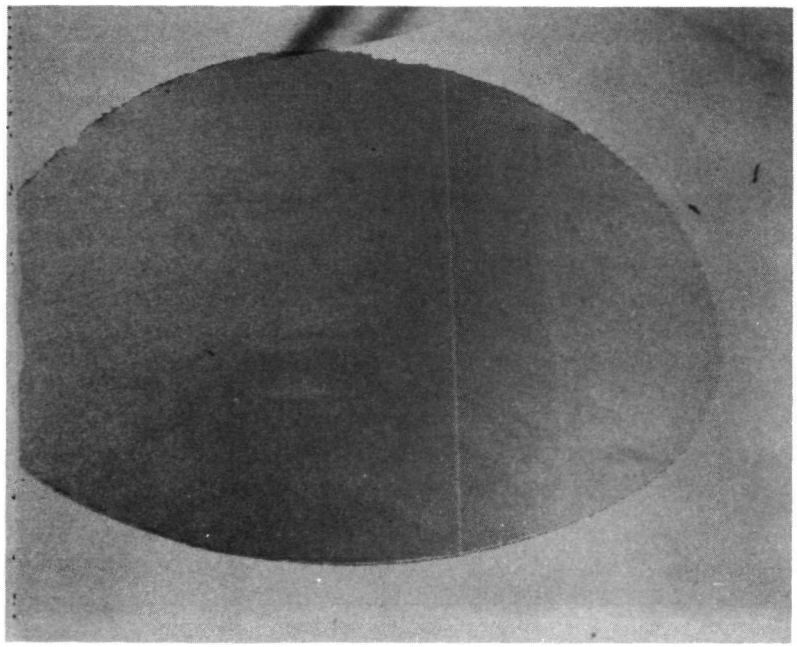

Figure 31. — Scanning Reflection Topograph of Thin (111) GdGaG Wafer; Boule B, FeKα_1 Radiation, (444) Reflection, 5.8X Magnification

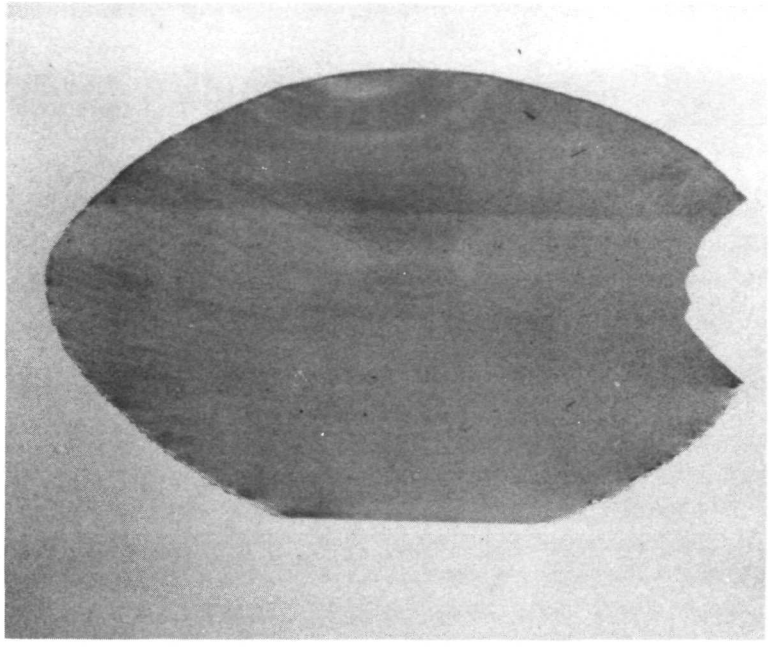

Figure 32. — Scanning Reflection Topograph of Thin (111) GdGaG Wafer; Boule B, FeKα_1 Radiation, (444) Reflection, 5.3X Magnification

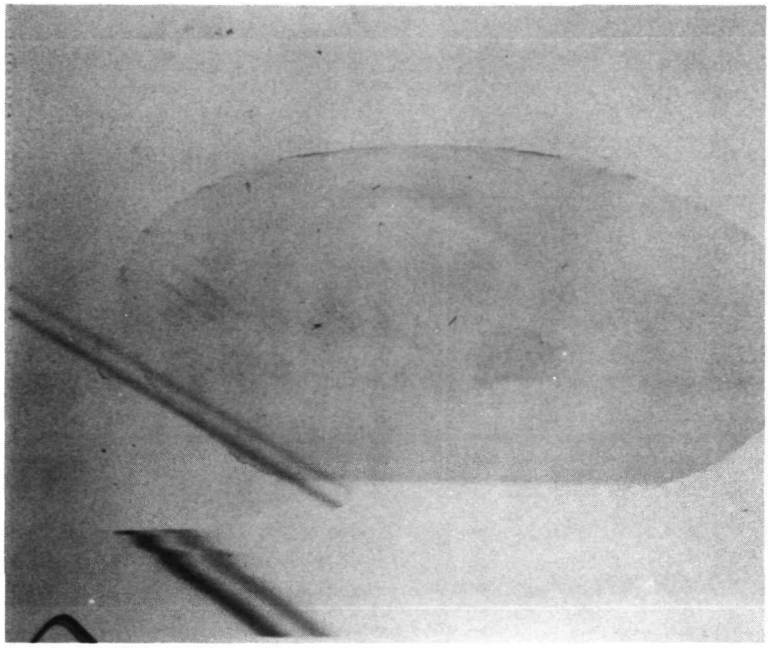

Figure 33. — Scanning Reflection Topograph of Thin (111) GdGaG Wafer; Boule C FeKα_1 Radiation, (444) Reflection, 4.5X Magnification

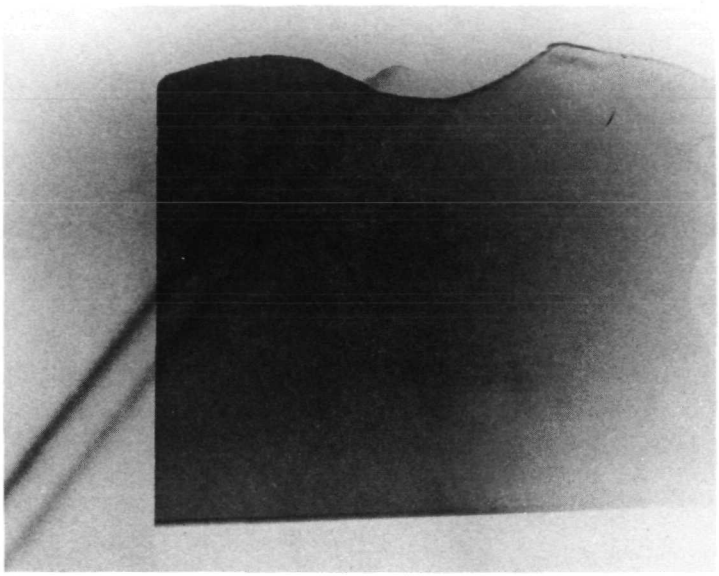

Figure 34. — Scanning Reflection Topograph of Thin (012) GdGaG Wafer; Boule C
FeKα_1 Radiation, (048) Reflection, 4.8X Magnification

radiation, except that CuKα_1 was used for figure 30. Also, due to specimen breakage, figure 30 shows only a portion of the specimen seen in figure 24. All of these topographs suffer from a pronounced foreshortening in the horizontal direction. (Vertical directions in the figures.) This is a consequence of the oblique angle between the diffracted beam and the specimen surface. The horizontal compression is about 30 percent for figures 31 to 33 but less for the other two figures. The core and band structures are present in all of these reflection topographs. However, in most cases the visibility of these features is lower in the reflection topographs than in transmission.

Scanning reflection topographs of other garnet specimens are shown in figures 35 to 41. These specimens, in contrast to the previous ones, were sufficiently thick for use as CVD seeds. All of these topographs, except for figures 35 and 41, are (444) symmetric reflections made with FeKα_1 radiation. Figure 35 is an (888) symmetric reflection with CuKα_1 radiation. Foreshortening is considerably reduced under these conditions. Foreshortening is completely negligible in the case of figure 41, an asymmetric (480) reflection with FeKα_1 radiation for which the diffracted beam emerges nearly normal to the specimen (11$\bar{1}$) surface. This is the same specimen as seen in figure 40.

These reflection topographs reveal core and band structures of various configurations similar to those of the previous topographs. Again it is seen that the visibility of these structures is, in general, not as good for reflection as for

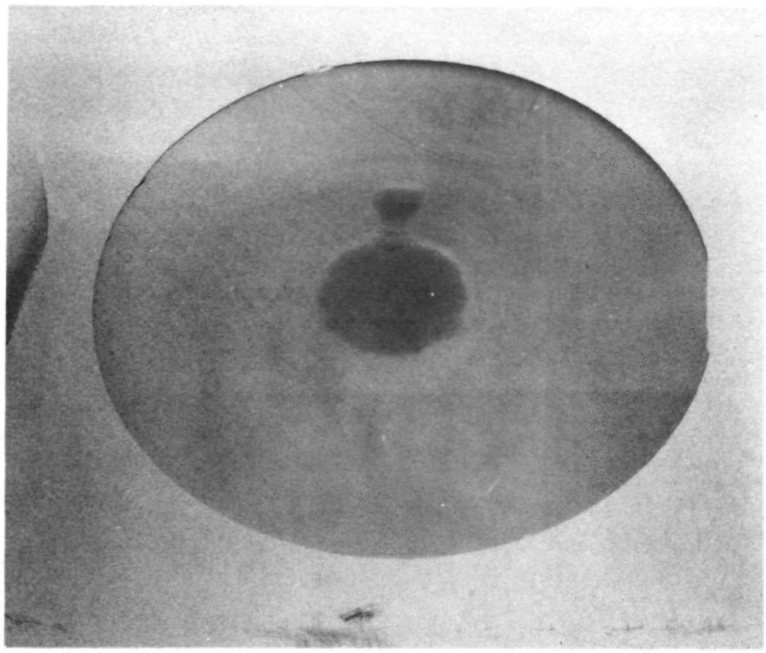

Figure 35. — Scanning Reflection Topograph of Thick (111) GdGaG Wafer; Boule D, $CuK\alpha_1$ Radiation, (888) Reflection, 5.4X Magnification

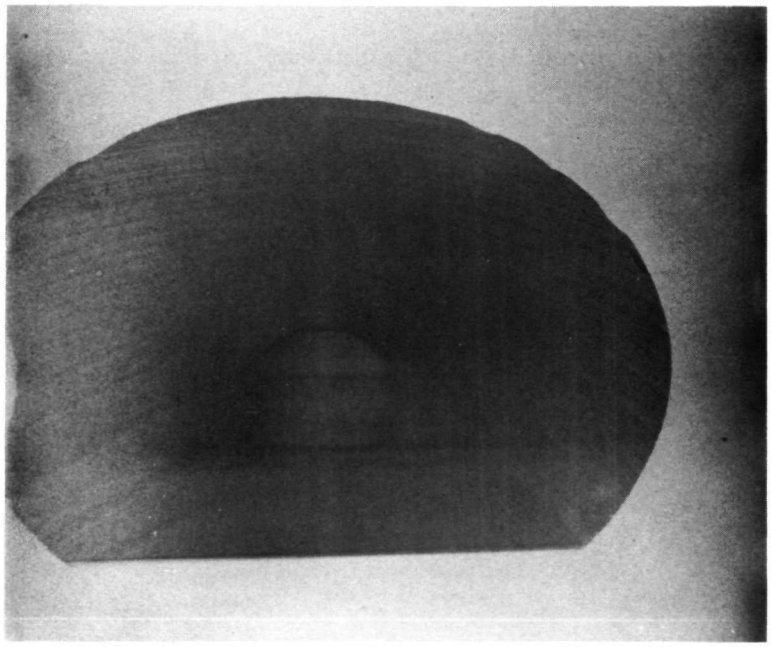

Figure 36. — Scanning Reflection Topograph of Thick (111) GdGaG Wafer; Boule B $CrK\alpha_1$ Radiation, (444) Reflection, 4.5X Magnification

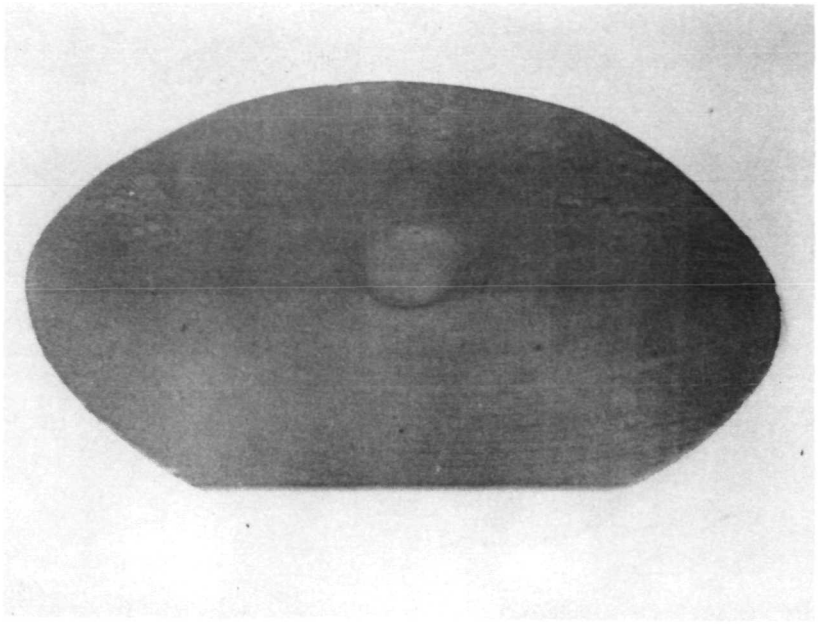

Figure 37. — Scanning Reflection Topograph of Thick (111) GdGaG Wafer; Boule B, $FeK\alpha_1$ Radiation, (444) Reflection, 5.7X Magnification

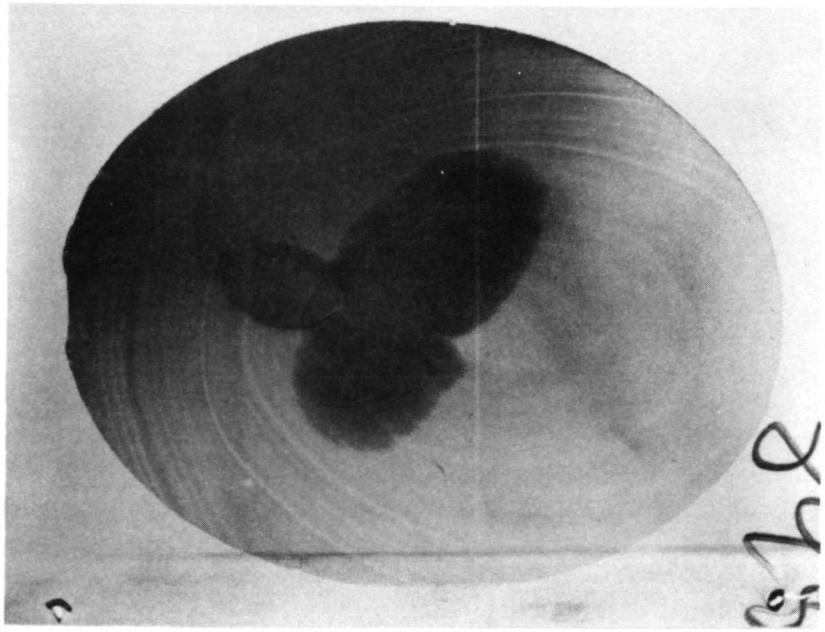

Figure 38. — Scanning Reflection Topograph of Thick (111) DyGdGaG Wafer; Boule E, $CuK\alpha_1$ Radiation, (888) Reflection, 4.9X Magnification

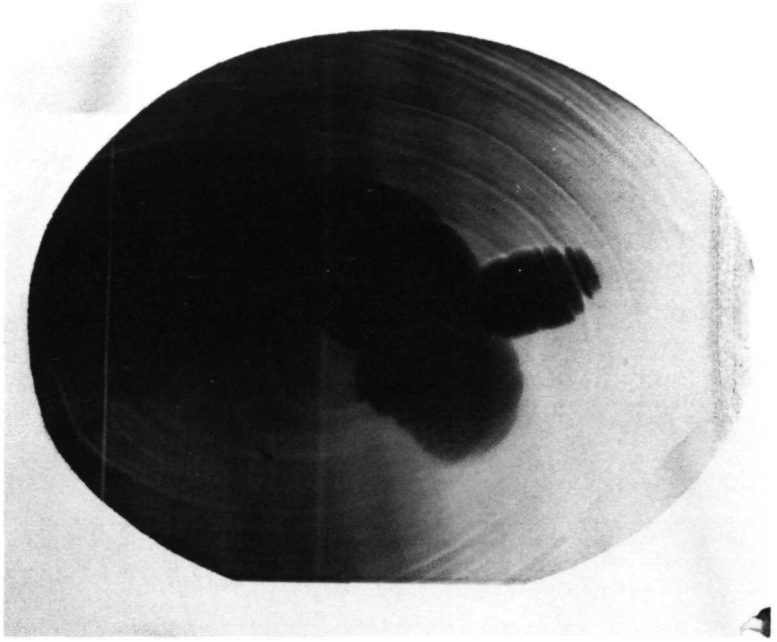

Figure 39. — Scanning Reflection Topograph of Thick (111) DyGdGaG Wafer; Boule E, $CuK\alpha_1$ Radiation, $(\bar{8}\bar{8}\bar{8})$ Reflection, 4.9X Magnification

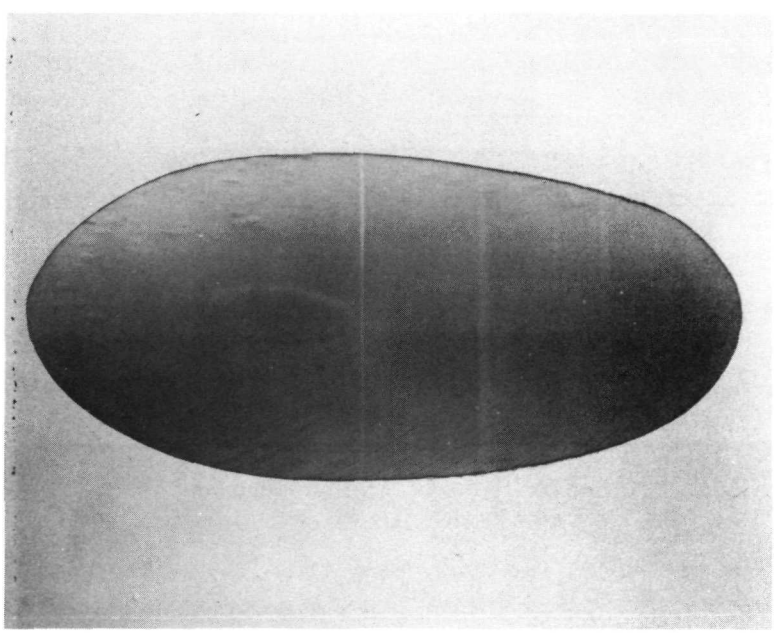

Figure 40. — Scanning Reflection Topograph of Thick (111) GdGaG Wafer; Boule B, $FeK\alpha_1$ Radiation, (444) Reflection, 4.9X Magnification

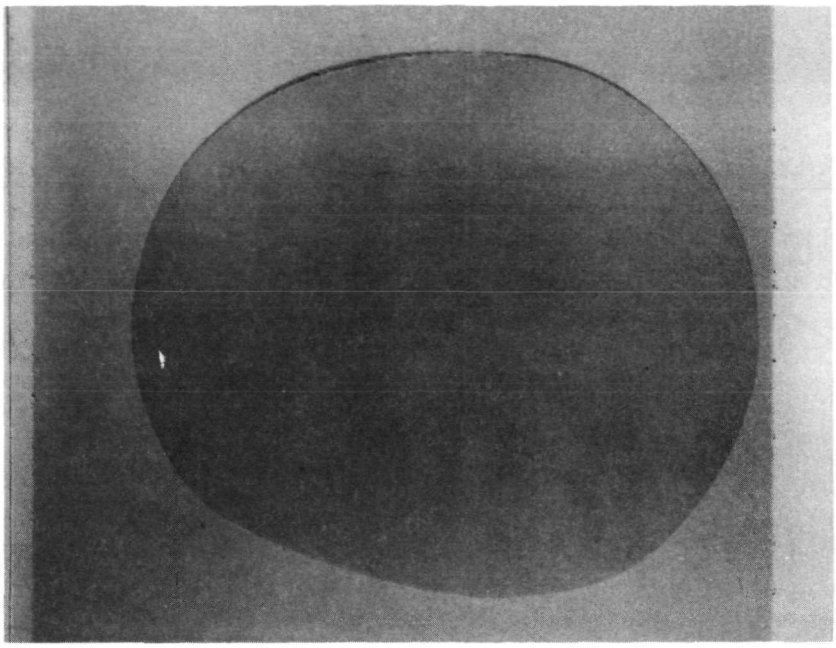

Figure 41. – Scanning Asymmetric Reflection Topograph of Wafer shown in Figure 40; $FeK\alpha_1$ Radiation. (480) Reflection, 4.4X Magnification

transmission. The core and bands are not discernible at all in figure 41 although they can be seen in the topograph of the same specimen in figure 40.

The above described topographic methods are quite suitable for revealing the defect structures of bare substrates. However, they are not entirely satisfactory for investigating substrates with epitaxial films. In the garnet system the film/substrate combinations that are of interest are those for which there is a small lattice parameter difference (Δa) between film and substrate. Consequently, it is difficult to orient these specimens in such a way that the substrate diffracts but the film does not (or vice versa). Using the above techniques it is not possible to obtain a topograph of the substrate which is free of contributions from the film. Similarly it is difficult to obtain a topograph of the film and be certain that it does not contain contributions from the substrate.

5.4.2.3 Double-crystal topography: An instrument that permits a separation of the diffracted beams of film and substrate is the double-crystal diffractometer (ref. 61). This apparatus, which is employed routinely for measurements of Δa, is shown schematically in figure 42. The X-ray beam from the source inpinges upon the nearly perfect first crystal (reference crystal), which is set at the Bragg angle for diffraction of the characteristic radiation by (hkl) planes parallel to the surface. The diffracted beam from the reference crystal is incident on the second crystal (specimen). The specimen is slowly rotated about an axis normal to the plane of the figure.

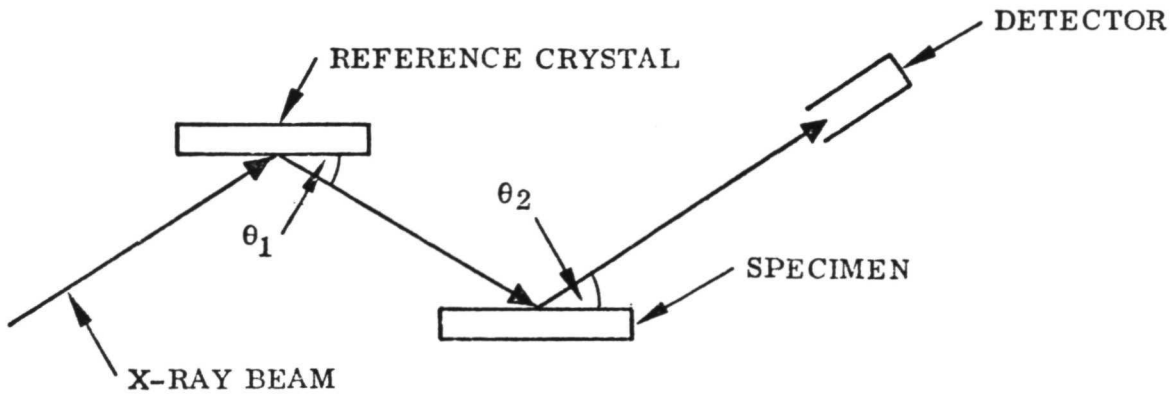

Figure 42. – Double-Crystal Diffractometer (Specimen is rotated around axis normal to plane of paper)

As the specimen rotates through its Bragg angle, a diffracted beam is generated, which is picked up by the detector. The detector output, a plot of diffracted intensity versus rotation angle of the specimen, is known as a rocking curve.

If the Bragg angles of the reference crystal and specimen are nearly equal, the double-crystal diffractometer has nearly zero chromatic dispersion; i.e., the finite wavelength spread in the X-ray spectral line does not produce angular broadening of the diffracted beam. Thus, the rocking curves may be considerably sharper than diffraction profiles obtained without the use of a reference crystal. This increased sharpness permits an angular resolution of the film and substrate diffracted beams. The rocking curve then consists of two peaks with the peak separation being a direct measure of Δa.

Unlike the Lang camera, the double-crystal diffractometer employed in this investigation does not have a mechanism for translational scanning of the specimen. To overcome this deficiency, an asymmetric (hkl) reflection is chosen so that at the Bragg angle the incident beam makes a small angle with the specimen surface. This is shown in figure 43. As a result of the near-grazing incidence, the incident beam width has a large projection on the specimen surface and a large area can be imaged. Furthermore, by appropriate choice of (hkl) and X-ray wavelength, the diffracted beam can emerge nearly normal to the specimen surface so that foreshortening is negligible.

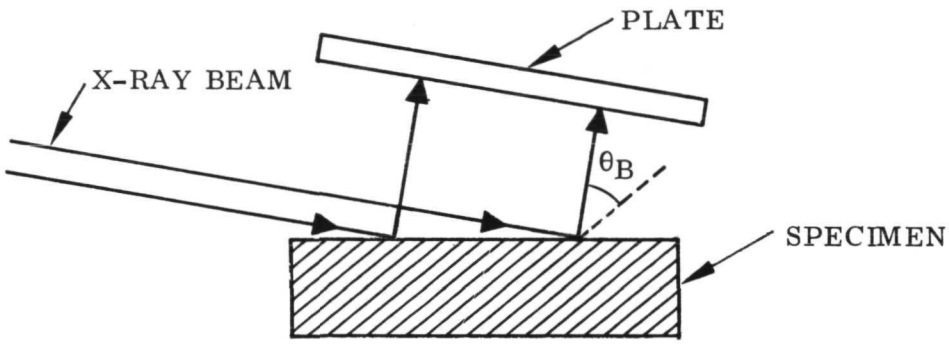

Figure 43. – Asymmetric Reflection Topography

In the case of (111) oriented garnets, FeKα radiation and reflecting planes of the form {840} satisfy the above conditions. A suitable choice of reference crystal is Si (400). This gives a good Bragg angle match so that chromatic dispersion is negligible. Highly perfect Si crystals are readily available.

In the double-crystal diffractometer it is not always convenient to separate the Kα_1 and Kα_2 radiations by means of slits. In the absence of chromatic dispersion, however, both wavelengths are diffracted simultaneously. Consequently, when a photographic plate is placed close to the specimen to intercept the diffracted beam and record the topograph, two slightly displaced images are formed. However, the resolution remains sufficiently good for observation of the core and band structures and of most of the other defects as well. Since the core and band structures are of principal interest, high-speed X-ray film can be used in place of fine-grained plates. The attendant loss in resolution is often an acceptable tradeoff in return for a significant reduction in exposure time.

Figure 44 shows a series of four asymmetric reflection topographs obtained using the double-crystal diffractometer. The specimen was a YIG film on a GdGaG substrate. The topographs were recorded at four different points along the film peak of the rocking curve. From one topograph to the next, the specimen was rotated through an angle of approximately 25 sec of arc. It is noteworthy that the entire film was not imaged in any one topograph. As the specimen was rotated, successive areas came into view.

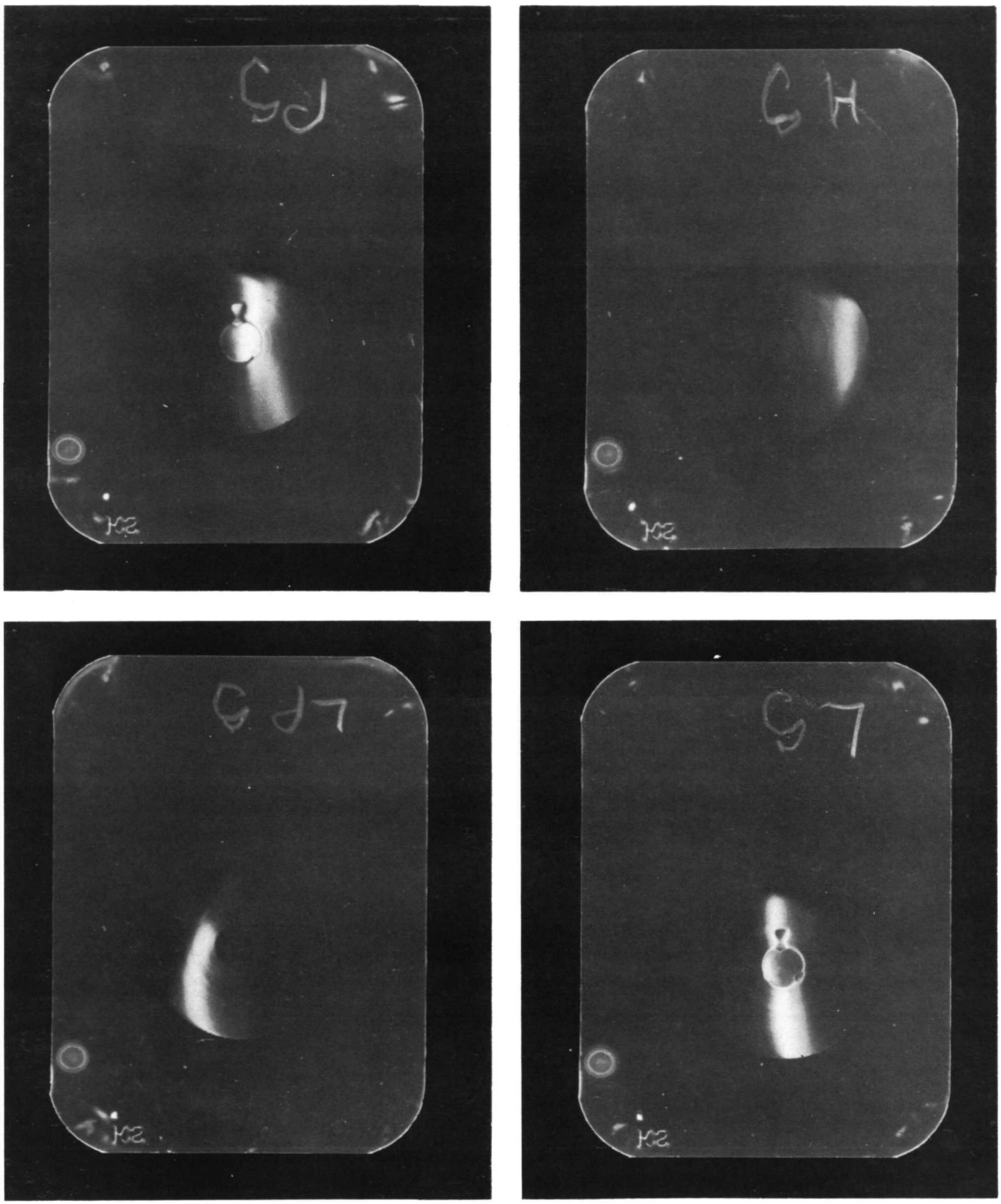

Figure 44. – Double-Crystal Asymmetric Reflection Topographs of YIG Film on GdGaG Substrate; FeKα Radiation, (480) Reflection, 2.1X Magnification

The topographs of figure 44 clearly show that the film possesses core and band structures. These structures closely correspond to the core and band structures of the substrate seen in the topograph of figure 45. This topograph was obtained by rotating the specimen to the peak position of the rocking-curve substrate peak. A scanning reflection topograph of the same substrate prior to deposition was seen in figure 35.

Figure 46 shows another series of double-crystal topographs. In this case the specimen was GaYGdIG/GdGaG, and the specimen rotation between topographs was about 50 sec of arc. Only topographs of the film were obtained. The rocking-curve substrate peak was weak and could not be isolated from the broad tails of the film peak. However, prior to deposition the substrate was imaged by the scanning reflection method, figure 37. Again it is seen that the film possesses core and band structures similar to those of the substrate.

5.4.3 Discussion. - All of the substrate crystals that have been examined by X-ray diffraction topography contain core and band structures. Such features are quite common in crystals grown by the Czochralski technique and have been reported in the case of doped and undoped YAG (yttrium aluminum garnet) (ref. 62). The core structure is attributed to the development of facets on the solid/liquid interface during growth. In the case of <111> grown YAG, faceting was found to occur primarily on {211} planes and secondarily on {110} planes. The present observations on cores in gallium garnets are consistent with the YAG results..

The band structures are believed to represent sections through successive solid/liquid interfaces. The variations in diffraction contrast, which make the bands (and cores) visible in topographs are probably associated with fluctuations in lattice parameters; i.e., the lattice parameter fluctuates about some mean value as the crystal grows from the melt. These fluctuations could arise from changes in the incorporation of impurities or from deviations of the principal constituents from the stoichiometric ratio. It is significant that in the present work core and band structures have been observed in supposedly stoichiometric GdGaG as well as in rare-earth-substituted GdGaG. Rocking curves of GdGaG substrates indicate that the lattice parameter fluctuation is on the order of 10^{-3} A.

The substrate core and band structures are generally less visible in reflection topography than in transmission. This is undoubtedly associated with the fact that while transmission topographs image the full specimen thickness (about 100 μm) the reflection topographs image only a relatively thin surface layer. This suggests that the substrates possess some sort of surface damage, probably as a residue from mechanical polishing.

An estimate of the thickness of the damaged surface layer can be made by comparison of the topographs of figures 40 and 41. Figure 41 is an asymmetric reflection topograph in which the incident beam makes a very small angle with the specimen surface. The X-ray penetration depth, defined as the depth beneath the surface for which absorption causes an attenuation in the diffracted beam of e^{-1}, is about 0.81 μm. For figure 40, a symmetric reflection from the same surface, the penetration depth is about 2.7 μm. Core and bands are visible in the symmetric case but not in the asymmetric case. Hence, it may be concluded that the surface damage extends approximately 1 μm below the surface. The nature of this damaged layer, however, has not been determined.

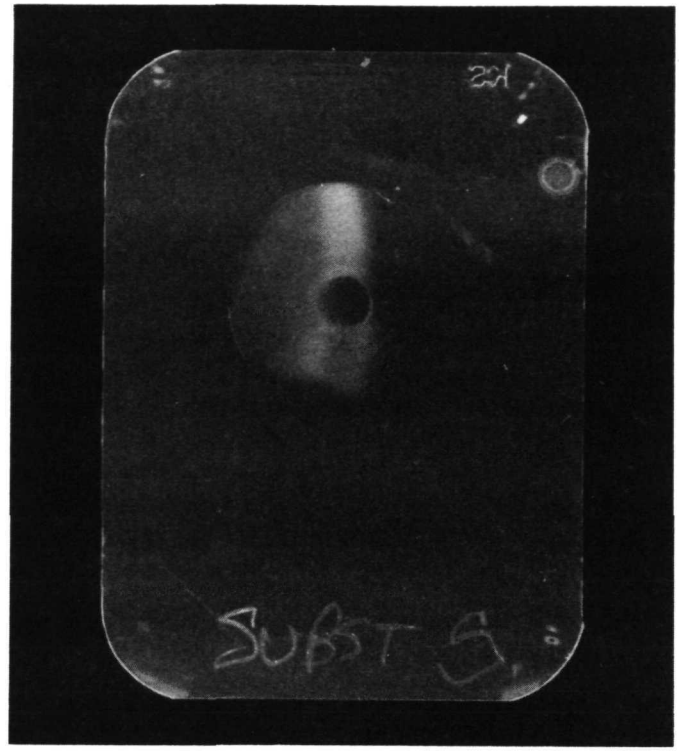

Figure 45. – Double-Crystal Asymmetric Reflection Topograph of Substrate Underlying Film of Figure 44; FeKα Radiation, (480) Reflection, 2.1X Magnification

The topographs of figures 44 and 46 clearly demonstrate that the films develop core and band structures very similar to those of the underlying substrates. This is an extremely significant finding that demonstrates the ability of the CVD process to reproduce the substrate structure in detail. The contrast mechanism that renders the core and band structures visible in the film topographs is probably the same as that in the substrate topographs: variations in lattice parameter. However, the CVD process differs considerably from the Czochralski process so that the method by which lattice parameter variations develop should be different for the two cases.

The effect of the core and bands on bubble propagation has not been fully determined There is some evidence of an effect in the case of GaErIG films on DyGdGaG substrates. If necessary, the development of core and bands in the substrate can be controlled to some extent by adjustment of the growth parameters.

The ability of the film to reproduce the defect structure of the substrate in spite of the existence of a relatively thick layer of substrate surface damage can not be adequately explained at present. It is possible that the surface damage is removed during the early stages of CVD (annealing or etching) or that the depositing film can diffuse through the damaged layer. Yet another possibility is that the short-range disorder introduced by the surface damage does not destroy the long-range strain fields of the core and band structures. Thus the core and bands may be invisible to the X-rays yet remain "visible" to the depositing film.

Another feature of the film topographs in figures 44 and 46 is that, as the specimen is rotated, successive areas are imaged. This effect is also observed, though to

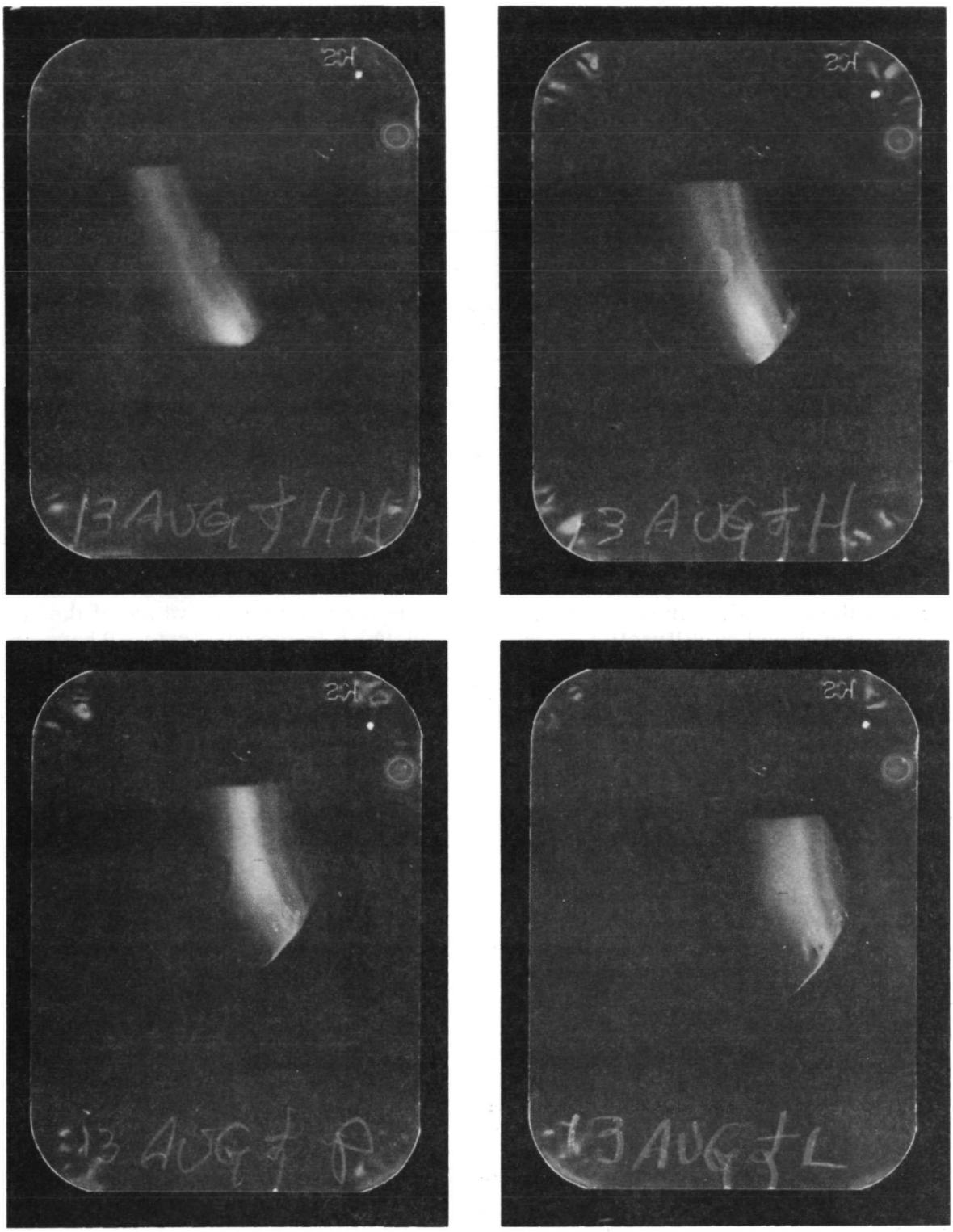

Figure 46. — Double-Crystal Asymmetric Reflection Topographs of GaYGdIG Film on GdGaG Substrate; FeKα Radiation, (480) Reflection, 2.1X Magnification

a lesser degree, in the substrate topograph of figure 45, and is indicative of the presence of long-range strain, probably elastic curvature. It is not clear whether this curvature was present in the original substrate or whether it is a manifestation of the stresses set up between substrate and film. The curvature is not apparent in the scanning reflection topographs of bare substrates, figures 35 to 41. However, that topographic technique is less sensitive to such effects than is double-crystal topography.

5.5 Film-Substrate Lattice Parameter Difference and Film Lattice Parameter

The difference in lattice parameter (Δa) between film and substrate is measured by X-ray diffraction. In view of the relatively small value of Δa, a high-resolution diffraction technique having minimal instrumental aberration is required. The instrument employed is the double-crystal diffractometer described in paragraph 5.4.2.3.

The rocking curves obtained from the crystals used in this program are sufficiently sharp to permit the resolution of two peaks: one peak corresponding to the film, and one to the substrate. The angular separation of these two peaks is a measure of the absolute value of Δa. The sign of Δa may be ascertained once the identities of the two peaks are established; i.e., one must determine which of the two peaks is produced by diffraction in the film and which in the substrate. There are several ways of making this determination. One method involves the use of a photographic plate to record a double exposure with the specimen set at each of the two peak positions. This makes it possible to see which of the two peaks is produced by diffraction near the surface of the specimen (film) and which from the interior of the specimen (substrate). A second method is to compare the areas under the two peaks. The ratio of the areas is a function of film thickness, film and substrate composition, X-ray wavelength, and diffraction geometry. Although these parameters may be sufficiently well known to permit a calculation of the ratio and thus identify the peaks, a simpler method is to compare the rocking curves obtained under two different sets of diffraction conditions; e.g., rocking curves may be recorded with MoK_α and with FeK_α radiations. Since these two wavelengths have markedly different penetrating powers, the peak identities can be ascertained by a simple inspection of the relative peak heights.

The diffracting planes of the specimen are those that are parallel to the surface of the film so that the interplanar spacings that are measured by the rocking curve technique are perpendicular to the film surface. Therefore, the lattice constant differences measured in this way are designated by $\Delta a^{\perp}$. For the heteroepitaxial nucleation and growth of a film on a substrate, the lattice dimensions parallel to the film surface are the ones that must be compared. In the unstrained condition, the lattice spacings parallel and perpendicular to the film surface would be identical in a cubic system, but since there is a strain, they are unequal. By using the relationship between parallel and perpendicular strain and a Poisson's ratio of 0.29, the

rocking curve $\Delta a^{\perp}$ may be expressed in terms of the unstrained film and substrate lattice parameters, a_f and a_s as

$$\Delta a^{\perp} = 1.82 (a_s - a_f) = 1.82 \Delta a \quad (1)$$

Thus, the rocking-curve technique provides a means for measuring the lattice parameter of the film when the substrate lattice parameter is known.

Values of $\Delta a^{\perp}$ have been measured for several films of GaYGdIG/GdGaG for comparison with domain structure and crazing observations. These values are listed in table XXII along with Δa and a_f values calculated from equation (1) using a value of a_s of 12.383 Å. Because of the definition of Δa, it is positive if $a_s > a_f$ and negative if $a_f > a_s$. It is also indicated in table XXII whether or not the film is crazed. This type of information has been used to establish the useful limits on Δa to avoid crazing.

From these results it is evident that films 3- to 6-μm thick begin to crack for values of $\Delta a^{\perp}$ somewhere between 0.010 and 0.017 Å. It has been found experimentally that: (1) the allowable value of $\Delta a^{\perp}$ decreases as the film thickness increases, and (2) the cracks initiate from the edge of the film where the film thickness is somewhat greater than in the center. In order to ensure sound films in the 3- to 6-μm range, it is required to keep $\Delta a^{\perp} < \sim +0.010$ Å ($\Delta a < \sim +0.005$ Å).

TABLE XXII. – LATTICE MATCHING AND CRAZING DATA FOR GaYGdIG/GdGaG

Sample	$\Delta a^{\perp}$ (Å)	Δa (Å)	a_f (Å)	Approximate Composition Z	Composition X	Thickness (μm)	Film Integrity
2558	+0.010	+0.0055	12.377	0.63	1.02	3.50	Uncrazed
2602	+0.003	+0.0016	12.381	0.82	1.10	5.42	Uncrazed
2606Z3	+0.023	+0.0127	12.370	0.47	1.10	3.88	Crazed
2606Z4	+0.024	+0.0132	12.370	0.44	1.05	3.23	Crazed
2608Z3	+0.022	+0.0121	12.371	0.47	1.05	4.30	Crazed
2609Z3	+0.009	+0.0050	12.378	0.66	1.00	4.77	Uncrazed
2610Z3	-0.010	-0.0055	12.389	0.92	0.85	~4.00	Uncrazed
2614Z3	+0.017	+0.0094	12.374	0.55	1.00	3.42	Partially Crazed

5.6 Film Thickness

The diameter and the static stability range of bubble domains depend on the film thickness. Also, in order to calculate $4\pi M$ and ℓ from data on bubble diameter vs field, it is necessary to know the film thickness. Metallographic angle lapping and infrared interference have been used to determine the thicknesses and good agreement is obtained between the two methods. The interference method is preferable in that it is rapid and nondestructive. However, it requires that the back side of the substrate be polished and thereby demands additional work during substrate preparation.

The optical transmission spectrum of a gallium-substituted iron garnet film is shown in figure 47. It consists of the normal spectrum characteristic of ferric oxides with a superimposed interference pattern resulting from the difference in refractive indices of the film and the substrate. The refractive index of the substrate is 1.70 in the wavelength region of interest. Assuming the infrared refractive index of the film to be identical to that of bulk YIG (ref. 63); e.g., 2.19 at a wavelength of 2.0 microns, the film thickness calculated from the interference pattern is identical with that obtained by metallographic sectioning.

The occurrence of a well-defined set of interference peaks in the transmission spectrum of the epitaxial films is evidence of the good surface quality of the film and the sharpness of the film-substrate interface. Such interference patterns are not observed in epitaxial deposits with rough surfaces or those in which there is substantial interdiffusion between film and substrate (ref. 64).

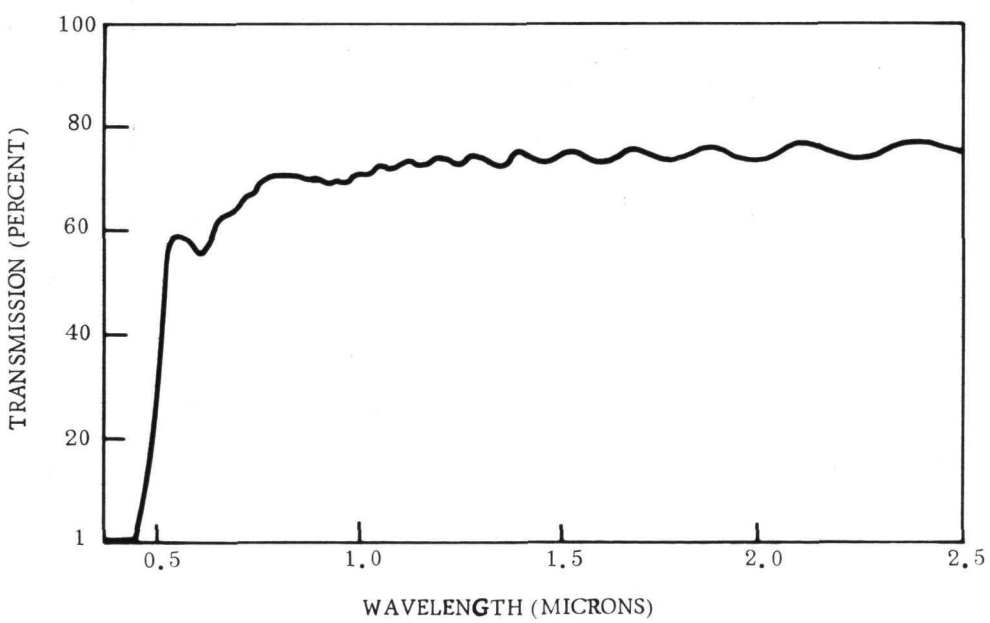

Figure 47. – Optical Transmission Spectrum of a Magnetic Garnet Film on a Nonmagnetic Garnet Substrate

The agreement between the thicknesses measured by metallographic cross-sections and those obtained from the interference peaks shows that the substituted garnet film has essentially the same refractive index as YIG. Since this is the case, such transmission spectra provide a convenient nondestructive measurement of film thickness. Most of the film thickness values listed in this report were obtained by infrared interference.

5.7 Domain Structure and Film Crazing Observations

The equilibrium domain structure that exists in a magnetic material results from a balance between different contributions to the total magnetic energy of the sample. The magnitudes of the various energy terms vary with material parameters and sample shape. The magnetization of a magnetic thin film will ordinarily tend to lie in the plane of the film because of the demagnetization energy or "shape anisotropy" effects. If the magnetization were perpendicular to the plane of the film it would produce equal and opposite magnetic pole densities on the opposite surfaces of the film. These pole densities give rise to an internal field of magnitude $\sim 4\pi M$ with a polarity that tends to force the magnetization into the plane. The domain magnetizations may, however, still be perpendicular to the film plane if the magnetic easy axis is along the normal to the film and if the crystallographic anisotropy energy is comparable in magnitude to the demagnetization energy. This requirement may be stated in the form

$$\bar{H}_A = \frac{K_u}{2\pi M^2} > 1 \qquad (2)$$

where $\bar{H}_A$ is called the reduced anisotropy field and K_u is the uniaxial anisotropy energy constant.

Since the magnetic parameters such as K_u and $4\pi M$ change with composition, the domain patterns in a given sample are sensitive to the composition. In the epitaxial CVD magnetic oxides the domain patterns in a material of given composition are also strongly influenced by the film-substrate mismatch, as a consequence of magnetostriction. This program has investigated a range of film compositions in the system $Y_{3-z}Gd_zGa_xFe_{5-x}O_{12}$ ranging from $z = 3$, $x = 0$ to $z \approx 0.5$, $x \approx 1.1$. Additionally, several different substrates have been used during the course of the program. Many deposition runs have been made on the bubble-domain portion of this contract and domain observations are performed on each run. Thus considerable data on domain structures in these films has been obtained during the course of the contract. In this subsection typical examples of the domains observed in the films will be presented and the influence of material composition and film/substrate matching on the domain patterns will be shown and discussed. Observations on film crazing will also be presented and the domain structure and crazing results will be discussed in relation to the stress model (ref. 48). The order of presentation of data is roughly chronological, paralleling the development of the film/substrate combination to the present $Y_{2.4}Gd_{0.6}Ga_{1.0}Fe_{4.0}O_{12}/Gd_3Ga_5O_{12}$.

The domains are viewed by magneto-optical effects using transmitted light and a polarizing microscope (ref. 65). When the domains have a component of magnetization perpendicular to the plane of the film, the magnetic Faraday effect produces a large contrast between adjacent domains. For domain magnetizations lying in the plane of the film, the contrast between domains arises from the magnetic birefringence and the contrast is much less. Since viewing is normally done with the film plane horizontal, domains perpendicular to the film plane were referred to as "vertical" domains and those in the plane as "in-plane" or "horizontal" domains.

The lattice constants of the various substrates used in this program and of the end members of the GaYIG and GaGdIG systems are listed in table XXIII for future reference in this and following subsections.

The material samples 4 to 10 were grown in-house as described in Section III and their lattice parameters were determined experimentally. The lattice constants of samples 1 to 3 are literature values.

The initial samples on the bubble-domain work were films of GdIG/GdGaG. Although it was recognized that this material would probably have too low a magnetization ($4\pi M \approx 40$ gauss at 300°K) and too large a temperature sensitivity (T_{comp} = 14°C) for eventual bubble-material goals, there were several motivations for beginning here. Reasonably mobile single-walled domains had been reported in bulk

TABLE XXIII. – LATTICE CONSTANTS OF SUBSTRATES AND END MEMBERS OF FILM COMPOSITIONS

Material	Lattice Parameter (Å)
1. YIG	12.376
2. GdIG	12.472
3. YGaG	12.276
4. GdGaG	12.383
5. NdGaG	12.506
6. SmGaG	12.436
7. NdGdGaG	12.452
8. NdSmGaG	12.452
9. SmGdGaG No. 1	12.409
10. SmGdGaG No. 2	12.389

GdIG (refs. 66 and 67). The uniaxial anisotropy required for their formation was attributed to stress resulting from mechanical polishing. It was felt that in the CVD films the film/substrate mismatch would provide the required stress. Also, as discussed earlier, GdIG films had been successfully grown in this laboratory in 1967.

Single-walled vertical domains were indeed observed in (111) GdIG/GdGaG. An example of the domain pattern in such a sample is shown in figure 48. However, these domains were relatively immobile to the extent that no change occurred in the pattern until the perpendicular bias field was increased to ~30 to 40 Oe. They are also very irregular in shape as is evident in figure 48. Films of GdIG/GdGaG are usually crazed if the film thickness exceeds 2 or 3 μm. Several film cracks are evident in area shown in the figure.

The characteristic circular and smooth serpentine domains observed in good bubble-domain materials do not occur in such samples. The apparent cause of the irregular shape and immobility is a high wall coercivity. It has been found that samples with a large mismatch between film and substrate lattice constant generally have a high wall coercivity, hence relatively immobile domains. The coercivity of the epitaxial films is discussed further in paragraph 5.14. Since $a_f > a_s$ for GdIG/GdGaG the stress model predicts that the film would be in compression if it were in Region I (see Appendix). However, the occurrence of vertical domains shows that the film is in tension. Therefore, the lattice mismatch for GdIG/GdGaG must be greater than the limiting value for compression, Δa_2, and the combination corresponds to Region II where $|a_s - a_f| > |\Delta a_2|$.

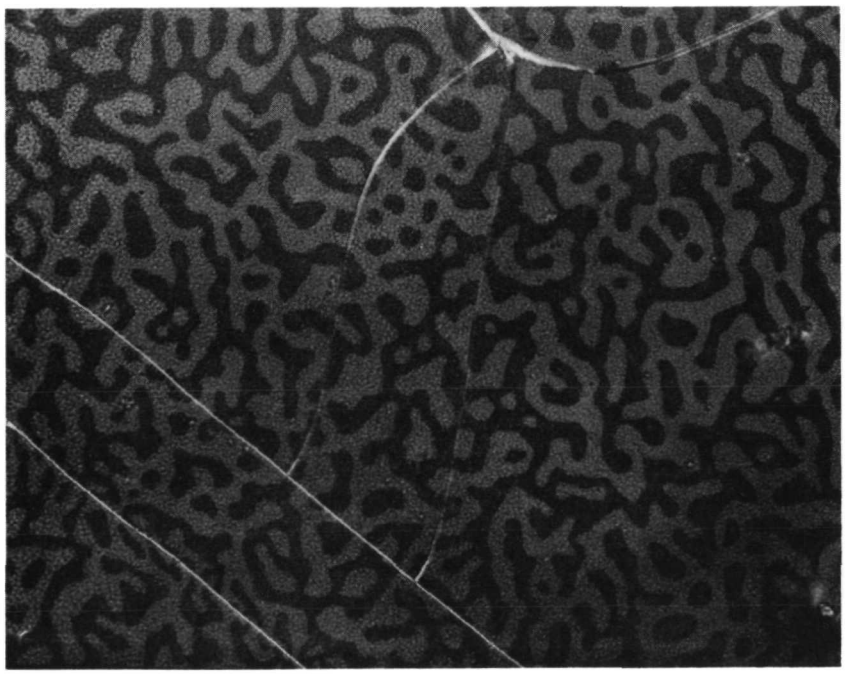

Figure 48. – Magnetic Domain Pattern in (111) GdIG/GdGaG (~200X Magnification)

Additionally, deposits thicker than ~3 μm are crazed in agreement with observations that crazing occurs for samples 3- to 5-μm thick in Region II combinations for the iron garnet/gallium garnet system (ref. 48 and Appendix). The thermal expansion mismatch between the iron and gallium garnets is apparently large enough to cause crazing in films of this thickness.

In an attempt to provide a better match to the lattice constant of GdIG, substrates of SmGG and NdGdGG were grown. The values of Δa for GdIG and the three substrates on which it was grown are shown in table XXIV.

Deposits of GdIG/SmGaG exhibited vertical single-walled domains. However, the films were crazed, the domains were essentially immobile, and the domain walls were irregular. A typical domain pattern is shown in figure 49. Many of the films grown at this time had rather poor surface quality, which is evident in the photograph. This roughness may also have contributed to the domain-wall pinning and high coercivity.

Since Δa is negative and the film is in tension, it appears that this combination also lies in Region II of the stress model.

Small mobile bubble domains and smooth serpentines were observed in certain areas of films of GdIG/NdGdGaG. An example of such an area is shown in figure 50. Other areas of films on NdGdGaG had irregular, high-coercivity domains similar to those shown in figures 48 and 49. This substrate material was poor in quality and the composition varied across the substrate wafers with the core region being higher in Nd. The Δa value in table XXIV thus represents an average value. In general the films grown on this substrate were poor in quality.

The interpretation of domain results on the NdGdGaG substrates is not completely clear. The crazing and high coercivity in some areas are what would be expected if Δa is ~ -0.030 Å since this is close to the case of GdIG/SmGaG. Other areas, however, are typical of what would be expected if the substrate lattice constant were closer to that of the film. The mobile bubbles shown in figure 50 are typical of those observed in samples where $0 < \Delta a < +0.010$ Å. It may be that these regions are Nd rich and the substrate lattice constant in this area is actually slightly larger than that of GdIG. In any event the poor quality of this substrate and most of the films grown on it clouds the interpretation of the domain structures. However, the

TABLE XXIV. – COMPARISON OF LATTICE CONSTANT MISMATCH FOR GdIG ON VARIOUS GALLIUM GARNET SUBSTRATES

Substrate	Δa (Å)
GdGaG	-0.088
SmGaG	-0.035
NdGdGaG	-0.030

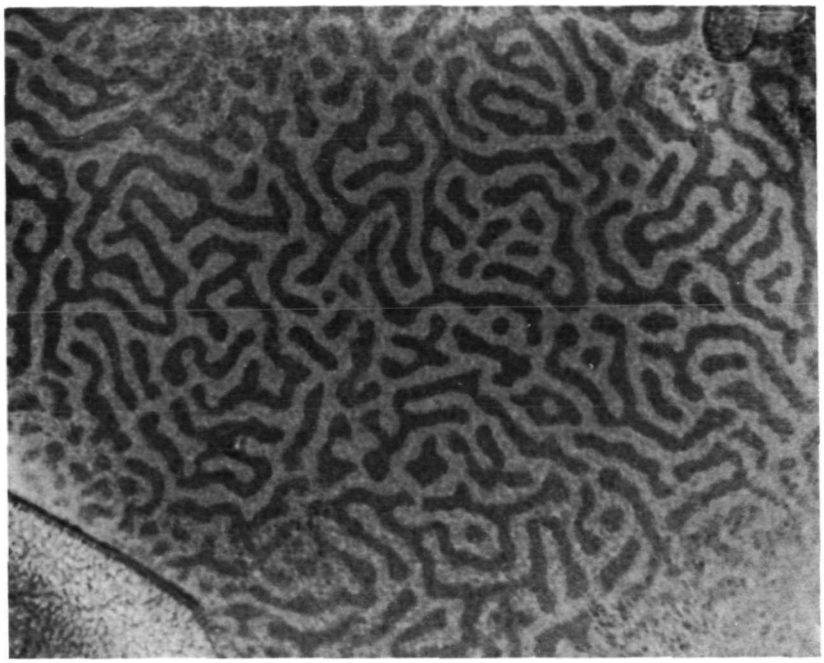

Figure 49. – Domain Pattern of (111) GdIG/SmGaG (~200X Magnification)

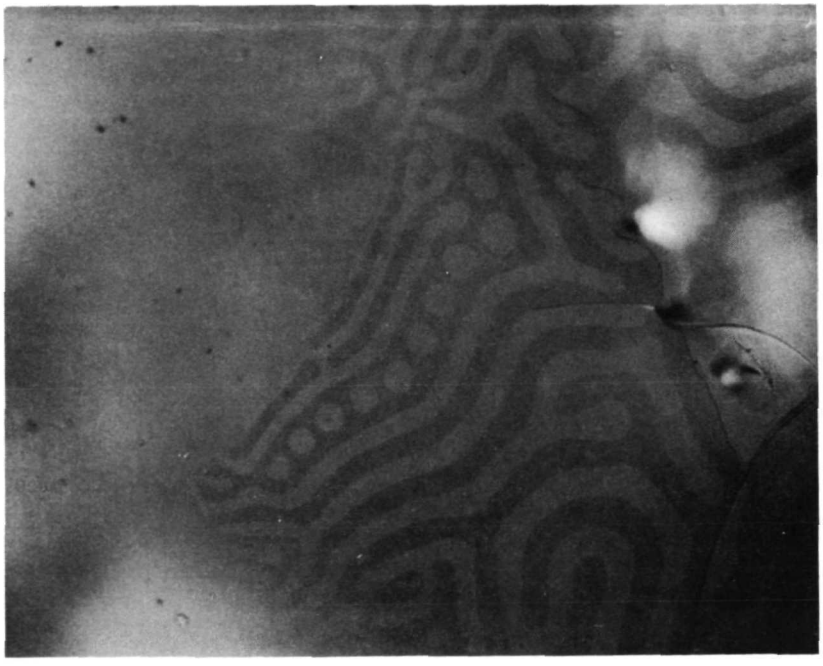

Figure 50. – Domain Pattern in Low-Coercivity Region of (111) GdIG/NdGdGaG (~200X Magnification)

observation of mobile bubbles and smooth serpentines in GdIG/NdGdGaG proved that low-coercivity epitaxial GdIG suitable for bubble domains could be attained if the film/substrate matching and quality could be improved.

The next step in the material development was the growth of mixed YGdIG films. Adding a small amount of Y to GdIG increases $4\pi M$, bringing it into a more desirable range for bubble domain requirements. Films of YGdIG were grown on substrates of GdGaG, NdSmGaG, SmGaG and TbGaG. These samples provide further support for the validity of the stress model for the garnet system.

The case of YGdIG on SmGaG will be discussed first since it illustrates best the transition from Region II to Region I, which is predicted by the model. For pure GdIG/SmGaG, $\Delta a = -0.035$Å and the vertical domains and film crazing in this system indicated $|\Delta a_2| < 0.035$Å. Since $a_f = 12.376$ for YIG, adding enough Y to GdIG will make $|\Delta a|$ less than $|\Delta a_2|$ and place the film in the compressive range of Region I. This, however, would result in in-plane domains. Further increase in Y content would bring the film into the tensile range of Region I and result in vertical domains once again. For low concentrations of Y in $Y_{3-z}Gd_zFe_5O_{12}$ ($z \approx 2.5$), the films on SmGaG were no longer crazed and the domains were horizontal or nearly so. This indicated that the films were either in compression or in insufficient tension. An example of in-plane type of domains seen in such samples is shown in figure 51.

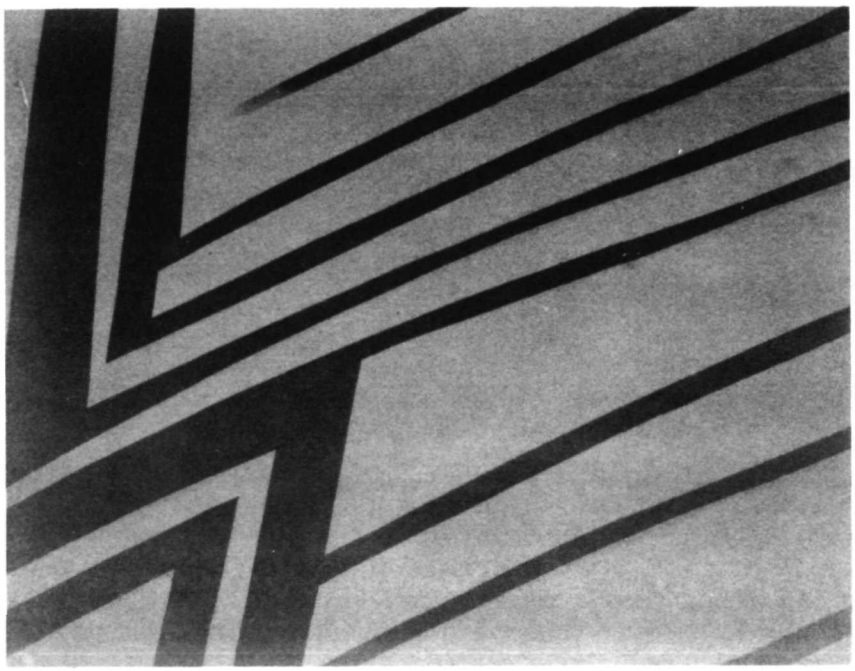

Figure 51. – Nearly In-Plane Domains in (111) YGdIG/SmGaG (~200X Magnification)

For films of the same composition on GdGaG, the deposits were crazed and high-coercivity vertical domains were present. These results are also consistent with the model. For a typical deposit with $z \approx 2.4$, $a_f = \approx 12.452$Å and $\Delta a = -0.069$Å on GdGaG and -0.019Å on SmGaG. The deposits on SmGaG are apparently in the compressive range of Region I while those on GdGaG still had $|\Delta a| > |\Delta a_2|$.

The YGdIG/NdSmGaG films were uncrazed and had mobile domains that were nearly in-plane. This is a result of the near-perfect match in lattice constants, $a_s \approx a_f \approx 12.452$ Å. The YGdIG/TbGaG deposits were badly crazed and had vertical, irregular domains with high coercivity. Since $\Delta a \approx -0.106$ for this combination it is undoubtedly in Region II.

These results on YGdIG films provided additional support for the validity of the model and indicated that it would be necessary to make Δa positive and relatively small ($< \sim +0.010$Å) to avoid crazing and have low-coercivity deposits with vertical domains.

However, ferromagnetic resonance measurements on YGdIG with $z \approx 2.4$ had confirmed the expectations that the material parameters of this composition were highly temperature sensitive. This sensitivity is primarily due to the proximity of T_{comp} to room temperature and the large positive $d(4\pi M)/dT$ at room temperature. Therefore, to reduce the temperature sensitivity the next step was to attempt the growth of the more complex composition $Y_{3-z}Gd_zGa_xFe_{5-x}O_{12}$ with $z \approx 0.6$ and $x \approx 1.0$. An additional motivation for this composition was that it might be possible to use GdGaG as a substrate.

Deposits of GaYGdIG were begun with the goal of achieving $z = 0.6$, $x = 1.0$. Substrates used during this portion of the work were SmGaG, SmGdGaG, and GdGaG and NdSmGaG.

The film compositions that gave uncrazed deposits with mobile bubbles on the NdSmGaG substrate were still too low in Y and the domain size was quite temperature sensitive.

The Ga and Y content were both increased through a series of runs. During this phase of the program, two or more different substrates were used in each run. By comparing domain structure and crazing observations of the same film on these different substrates an estimate of the film lattice constant could be obtained. (The double-crystal diffractometer was not yet available.) Measurement of T_{comp} and T_N by FMR then provided an estimate of film composition from which further deposition condition adjustments could be made.

This interrelation of deposition conditions, domain structure, film crazing and film-substrate lattice mismatch can be best illustrated by considering examples from three runs, Nos. 2531, 2546, and 2556.

In 2531 the GaYGdIG films were grown on two different SmGdGG substrates, SmGdGG-1 and SmGdGG-2, with $a_s = 12.409$Å and 12.389Å respectively. The deposit on substrate No. 1 had vertical domains and was crazed while that on substrate No. 2

had horizontal domains and was uncrazed. This indicated that a_f was less than 12.409Å but no smaller than 12.389Å.

The fact that the film on No. 1 was crazed indicated that $|\Delta a| \geq 0.010$ Å so an approximate value of a_f was taken as 12.394 Å. FMR data on these films gave T_N = 113°C from which a gallium content of x = 1.3 was determined. Assuming a Vegard's law variation of lattice constant with composition for the GaYGdIG system, the film composition is estimated to be $Y_{1.6}Gd_{1.4}Ga_{1.3}Fe_{3.7}O_{12}$. This composition is too low in Y and too high in Ga so deposition changes were made to correct this. In run 2546 two substrates were also used, SmGdGG-2, and GdGG. The films on both substrates were uncrazed and had vertical domains with serpentines and bubbles. However, the domains on the GdGG were smaller than those on SmGdGG as a consequence of the lower stress induced anisotropy on the GdGG due to the smaller Δa.

The vertical domains and lack of crazing indicated $a_f \approx 12.379$ Å. The Y and Ga transports were increased further in an attempt to reduce a_f to ≈12.375 Å, which would provide a good fit to GdGaG.

In run 2556 the film on SmGdG-2 was crazed with vertical domains but the deposit on GdGG was uncrazed and had large mobile bubble domains. The Y:Gd ratio was about right but the Ga content was too high. At this point attempts were made to make small adjustments in transports to get suitable bubble-domain material on GdGG. A few promising deposits were obtained, notably 2558 whose zero field domain structure is shown in figure 52. This sample is uncrazed and has bubble domains with diameters of ~4 μm just before collapse. At this time the changeover of the reactor to a 3-in. diameter T took place. After resumption of deposits, adjustments of deposition conditions were made to produce GaYGdIG deposits in the vicinity of $Y_{2.4}Gd_{0.6}Ga_{1.0}Fe_{4.0}O_{12}$ on GdGaG.

Two of the typical deposits were 2606Z4 and 2614Z3. The zero field domain patterns of the former sample is shown in figure 53. Sample 2606Z4 was apparently too small in lattice constant for the GdGaG substrate and was crazed although it had excellent domain size for bubble applications. By increasing the Gd content and decreasing the Ga content $4\pi M$ was maintained near ~150 gauss and a_f was increased. These changes resulted in sample 2614Z3, which is an excellent epitaxial bubble-domain sample. This sample is apparently quite near the maximum lattice mismatch that can be tolerated. Cracks started to propagate into the sample from the edges that are somewhat thicker than the central area. By removing these edge regions the crazing was stopped and a large crack-free area (~1 cm^2) was obtained. The magnetic and physical properties of this sample are quite close to the optimal target values for bubble-domain material as will be evident from the results presented in the remaining parts of this subsection.

5.8 Bubble Diameter as a Function of Bias Field and Temperature

The bubble diameter as a function of the static bias field is determined by Faraday effect domain observations using a polarizing microscope with field coils

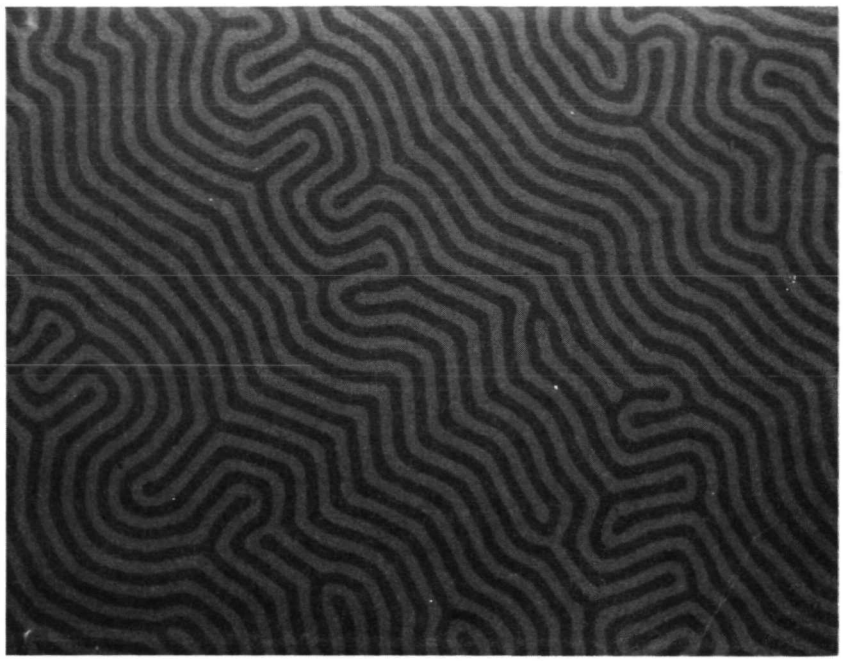

Figure 52. – Smooth Serpentine Domains in Sample 2558, (111) GaYGdIG/GdGaG (~200X Magnification)

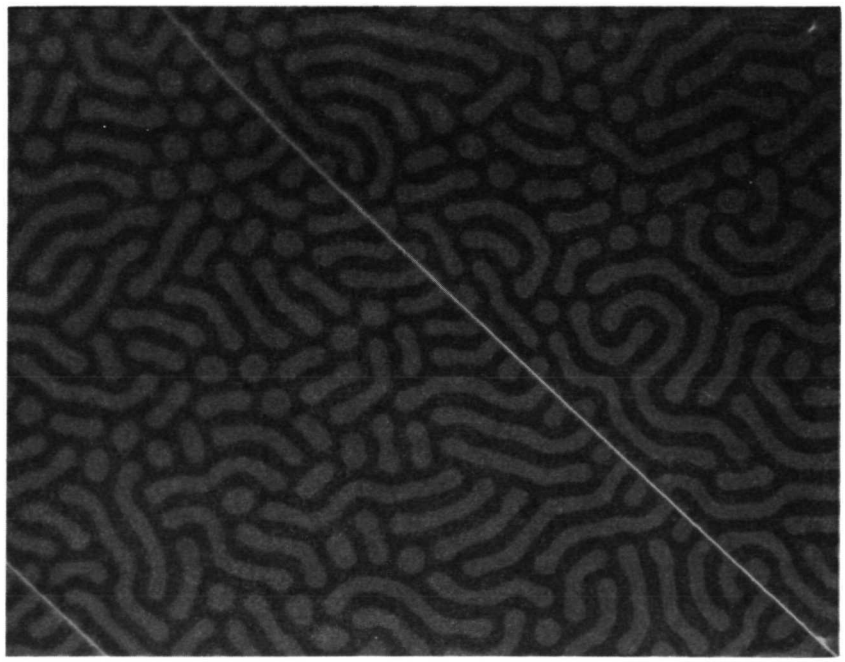

Figure 53. – Zero-Field Domain Pattern in Sample 2606Z4 (111) GaYGdIG/GdGaG (~200X Magnification)

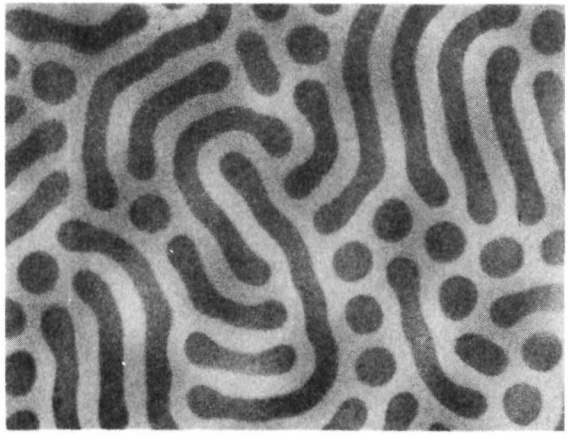

(a) H = O

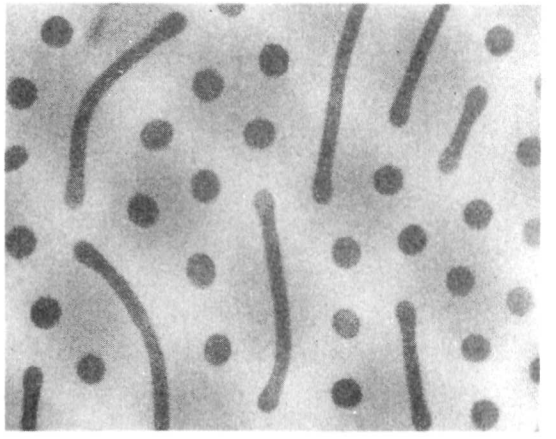

(b) H = 28.3 Oe

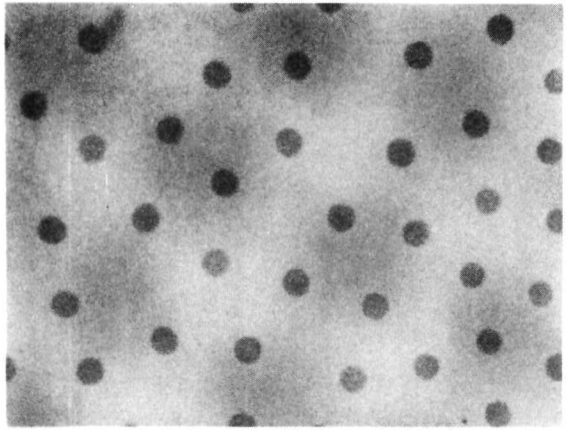

(c) H = 29.4 Oe

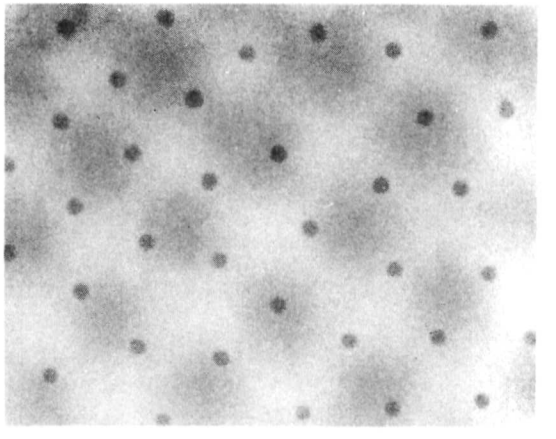

(d) H = 35.1 Oe

Figure 54. – Magnetic Domain Pattern as a Function of Bias Field in GaYGdIG Film

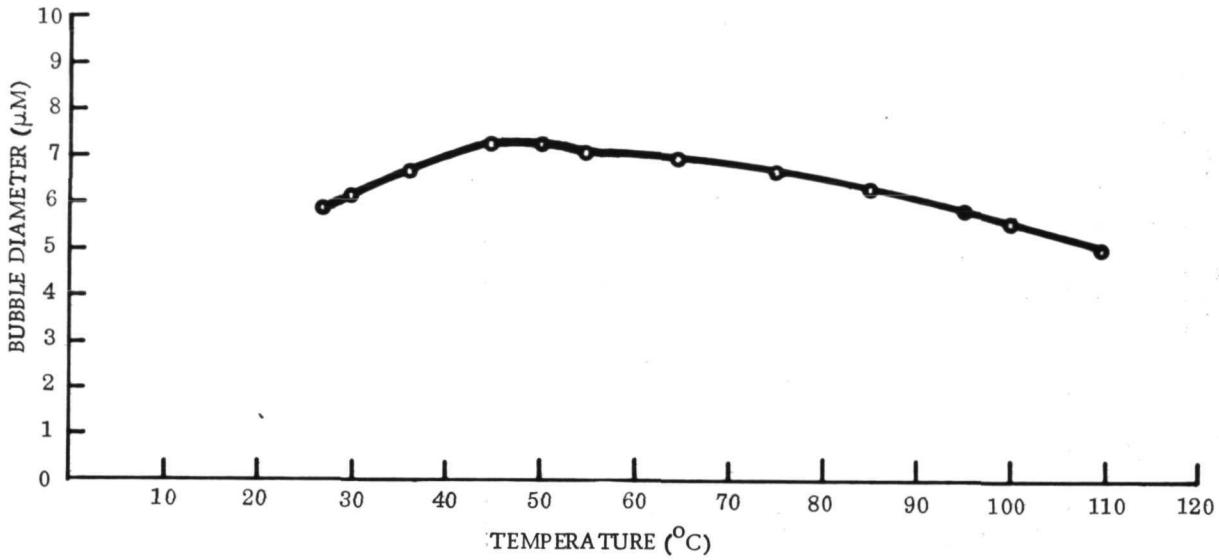

Figure 55. — Temperature Dependence of Domain Diameter in Epitaxial GaYGdIG - Sample 2614Z3 under Constant Bias Field.

attached. The domain diameter is measured either from a photograph of the domain or by the use of a calibrated filar eyepiece.

Although it is difficult to show in still photographs, the magnetic bubble domains in the present GaYGdIG films move readily in response to magnetic field gradients or due to interaction with other bubble or serpentine domains. Figure 54 shows magnetic domain patterns in sample 2614Z3. With no bias field, the pattern consists of a mixture of serpentine and bubble domains. As the bias field is increased, the domains contract so that only bubbles exist at magnetic fields greater than the runout field. Further increase in the bias field causes the bubbles to shrink until at a critical field, H_{col}, they collapse. The last photograph of the sequence was taken near H_{col}.

In this sample the bubble diameter at collapse is 4.9 μm. In an operating device the bubble diameter is ~1.5 to 2 times the collapse diameter. Thus, allowing a minimum spacing of 3 or 4 bubble diameters between bubbles, this film would provide a bit density on the order of $10^6/in^2$. Collapse fields and collapse diameters for several epitaxial samples are listed in table XXV along with certain other material parameters.

In any device that makes use of the movement of bubble domains, the patterns employed for generation, manipulation, and detection must be in proportion to the size of the domain diameter. Thus, a metal pattern used for bubble manipulation has a

TABLE XXV. – CHARACTERISTICS OF TYPICAL EPITAXIAL GaYGdIG FILMS

Sample	h (μm)	H_{col} (Oe)	d_{col} (μm)	ℓ (μm)	$4\pi M$ (gauss)		H_A (Oe)	$H_A - 4\pi M$
					a	b		
2558	3.5	32	4.0	1.0	110			
2587	3.6	75	2.8	0.7	187			
2588	2.6	37	2.8	0.7	125			
2602	5.4	32	5.0	1.3	93	100	130	30
2606Z4	3.2	30	4.8	1.2	130	130	470	340
2614Z3	3.4	37	4.9	1.3	115	160	420	260

a From bubble collapse
b From FMR and H_A data

specific spacing that will function for a limited range of domain diameters. If a bubble-domain device is to operate in an environment that permits temperature excursions, the influence of these changes on the domain diameter must be established to determine the temperature limits for reliable performance.

The temperature dependence of the bubble diameter in the garnet films at constant bias was determined by photographing the domain pattern at various temperatures. Data on a GaYGdIG film is shown in figure 55. In contrast to the results on $YFeO_3$ and films of GaYIG (ref. 22) this material shows an initial increase in domain diameter as the temperature is raised.

The temperature dependence of the domain diameter, d, can be related to the temperature dependence of the magnetization and the wall energy. The stability equation for bubble domains is

$$\frac{\ell}{h} + \frac{H}{4\pi M}\left(\frac{d}{h}\right) = F\left(\frac{d}{h}\right) \tag{3}$$

where $F(d/h)$ is the magnetostatic force function derived by Thiele (ref. 37). Making the substitution $\ell = \sigma_w/4\pi M^2$ and taking the temperature derivative of equation (3) gives

$$\frac{\partial d}{\partial T} = \frac{1}{(4\pi M^2)\left[\frac{dF}{d\left(\frac{d}{n}\right)} - \frac{H}{4\pi M}\right]}\left\{4\pi \frac{d\sigma_w}{dT} - \left(\frac{2\sigma_w}{M} + Hd\right)\frac{d(4\pi M)}{dT}\right\} \tag{4}$$

Consideration of the graphical solution of equation (3) shows that $H/4\pi M$ is always greater than the slope of F at the stable equilibrium diameter. Thus the factor multiplying the temperature derivative of σ_w and $4\pi M$ is negative and equation (4) can be written as

$$\frac{\partial d}{\partial T} = -\left|G\,(H,\ M,\ d)\right|\left\{4\pi \frac{d\sigma_w}{dT} - \left(\frac{2\sigma_w}{M} + Hd\right)\frac{d(4\pi M)}{dT}\right\} \tag{5}$$

where

$$G(H,\ M,\ d) = \frac{1}{(4\pi M^2)\left[\frac{dF}{d\left(\frac{d}{h}\right)} - \frac{H}{4\pi M}\right]}$$

Since $\sigma_w = 4(AK_u)^{1/2}$ for 180° walls in uniaxial materials $d\sigma_w/dT$ is negative because both the exchange constant and the anisotropy constant decrease with increasing temperature. Additionally, σ_w, M, H, and d are all positive quantities so the sign of the temperature dependence can be changed only by the $d(4\pi M)/dT$ term.

If $d(4\pi M)/dT$ is positive or zero, $\partial d/\partial T > 0$ and the domain diameter will increase with increasing temperature at constant bias.

If $d(4\pi M)/dT < 0$, $\partial d/\partial T$ can be either positive or negative depending on the relative magnitudes of $d\sigma_w/dT$ and $d(4\pi M)/dT$. The point at which $\partial d/\partial T = 0$ is given by

$$\frac{d(4\pi M)}{dT} = \frac{4\pi}{\frac{2\sigma_w}{M} + Hd}\left(\frac{d\sigma_w}{dT}\right) \tag{6}$$

For values of $d(4\pi M)/dT$ more positive than this, the domain diameter will increase with T, while for more negative values it will decrease.

For typical values of $H = 0.3(4\pi M)$, $d = 8\ell$, $4\pi M = 130$ gauss and $\sigma_w = 0.25$ erg/cm^2, equation (4) reduces to

$$\frac{d(4\pi M)}{dT} \approx 120\,\frac{d\sigma_w}{dT} \tag{7}$$

Assuming a linear decrease in σ_w between room temperature and T_N, and a T_N of 150°C, (7) gives $d(4\pi M)/dT = 120 \times (-0.25/125) = -0.24$ gauss/°C.

This is a very gradual negative temperature coefficient of magnetization. Thus, the magnetization vs temperature characteristic must be nearly flat in the device operating range if the bubble diameter is to remain reasonably constant.

The diameter vs temperature characteristic for the GaYGdIG sample shown in figure 55 shows a positive slope at room temperature indicating that $d(4\pi M)/dT$ is more positive than the value of equation (7).

The slope of the curve at a given temperature, normalized by the bubble diameter, can be used to define a figure of merit, the temperature coefficient, TC, as

$$TC = \frac{\Delta d}{\Delta T}\,\frac{1}{d} \times 100 \quad \%/°C$$

where d is the diameter at temperature T.

For the sample of figure 55, TC = +1.6%/C° at 25°C and TC = 0 at 45°C. The optimum situation would be to have TC ≈ 0 over the operating temperature range of the material.

The temperature stability of the film sample 2614Z3 of figure 55 seems to be adequate for device operation around room temperature as evidenced by the excellent stable domain propagation characteristics that it exhibited. These results will be described later.

5.9 Magnetization

It was initially planned that the saturation magnetization of the bubble-domain films would be obtained directly with the vibrating sample magnetometer (VSM) used on the lithium ferrite portion of the contract work. The magnetometer has been calibrated with high-purity (99.9-percent) Ni samples and has been used to measure the magnetization of epitaxial ferrite and garnet films. Since the magnetometer measures the total magnetic moment of the sample, it is necessary to know the sample volume in order to determine the saturation magnetization. Photolithographic techniques developed at Autonetics allow the etching of the films into geometries, such as disks, with well defined areas. The film thicknesses are determined by metallographic cross section and/or optical interference.

The $4\pi M$ values of YIG on GdGaG obtained by the magnetometer are in good agreement with those determined from microwave resonance results on the films and with literature values for bulk YIG.

However, the magnetizations required for bubble-domain materials (100 to 200 gauss) are an order of magnitude smaller than that of pure YIG (1780 gauss), leading to low values of film moment. These moment values are near the limit of sensitivity of the present VSM that was constructed in-house. Consequently, the magnetization data obtained from it shows considerable scatter and is of questionable accuracy. A commercial VSM with greater sensitivity was purchased but was not operational in time for use on this program.

The variation of bubble diameter with field can be used in conjunction with the theory of Thiele (ref. 37) to determine the magnetization and the characteristic length of bubble-domain materials. The stability condition for bubble domains is given by

$$\frac{\ell}{h} + \frac{H}{4\pi M}\left(\frac{d}{h}\right) - F\left(\frac{d}{h}\right) = 0 \qquad (8)$$

where F (d/h) is the magnetostatic force function derived by Thiele, and d is the domain diameter in a film of thickness h under a bias field H. Since graphs of F have been published (ref. 37), solutions of the above equation can be obtained by graphical construction using measured values of H, d, and h. With two unknowns ℓ and $4\pi M$, at least two separate measurements of d and H are required to determine the magnetization and the characteristic length. An alternative means that requires only a single value of H and d is the measurement of the collapse field H_{col} and diameter d_{col}. If the tangent to F is constructed at this value of (d/h), the slope of the tangent gives $4\pi M$, and its intercept determines ℓ.

Almost all of the magnetization data obtained on GaYGdIG films was obtained by the bubble-collapse method. Values of $4\pi M$ obtained in this manner are listed in table XXV.

It is also possible to determine $4\pi M$ from ferromagnetic resonance data if enough independent measurements can be made to evaluate the other unknowns in the resonance equations, such as the gyromagnetic ratio and the anisotropy field. This method is discussed further in paragraph 5.12. Good agreement has been obtained between

magnetization measured by the collapse technique and that obtained from FMR and anisotropy field measurements. These results are also included in table XXV for comparison with the data from bubble collapse.

5.10 Characteristic Length

The characteristic length is given by

$$\ell = \frac{\sigma_w}{4\pi M^2} = \frac{(AK_u)^{1/2}}{\pi M^2} \tag{9}$$

where A is the exchange constant and K_u the uniaxial anisotropy constant. Thus, ℓ can be calculated if the other parameters are known. However, since ℓ can be determined directly from the field variation of the bubble diameter, as discussed in paragraph 5.9, it has been obtained in this fashion for GaYGdIG films. Typical results for ℓ are included in table XXV.

5.11 Wall Energy

The wall energy of a 180° wall in a uniaxial material can be calculated from the relation

$$\sigma_w = 4\ (AK_u)^{1/2} \tag{10}$$

If A and K_u are known. However, direct and accurate measurement of A is a difficult task. Since the parameters ℓ and $4\pi M$ are obtained from bubble-collapse data, σ_w has been calculated from equation (9).

For CVD films of GaYGdIG/GdGaG the wall energy is typically 0.1 to 0.3 ergs/cm^2.

5.12 Ferromagnetic Resonance

One of the most important static parameters for the evaluation of potential bubble-domain materials is the difference between H_A and $4\pi M$. A convenient method for obtaining this difference directly is ferromagnetic resonance (FMR). If the static field H_o is applied perpendicular to the plane of a thin-film ($\perp$ resonance)

with uniaxial anisotropy, the resonance condition is given by

$$\frac{\omega}{\gamma} - H_o^{\perp} = H_A - 4\pi M \tag{11}$$

Here ω is the frequency of the microwave field, γ is the gyromagnetic ratio, and the superscript on H_o denotes $\perp$ resonance. When the applied field is in the plane of the sample ($\parallel$ resonance) the resonance condition is

$$\left(\frac{\omega}{\gamma}\right)^2 = H_o^{\parallel} \left(H_o^{\parallel} + 4\pi M - H_A\right) \tag{12}$$

Expressions (11) and (12) are valid for samples in which the contributions of the exchange energy and the magnetostatic energy to the frequency of the main resonance can be neglected. These conditions are generally well satisfied in epitaxial films of bubble-domain materials with $4\pi M \lesssim 500$ gauss and film thicknesses from 3 to 6 μm. By performing $\perp$ and $\parallel$ resonance measurements, the values of ω/γ and $H_A - 4\pi M$ can be determined. The measurements give an immediate indication of whether the static stability condition for bubble domains is satisfied; i.e., if $H_A - 4\pi M > 0$. X-band FMR measurements have been used to determine the sign and magnitude of $H_A - 4\pi M$ for various epitaxial film-substrate combinations studied on this contract. The values have been correlated with domain observations, mobility measurements, and deposition conditions to determine the optimum film-substrate combination.

If the anisotropy field, H_A, is determined independently, the magnetization can be obtained from the resonance data. Anisotropy field measurements have been made on film samples using the in-plane field technique of ref. 68. These results are described in more detail in paragraph 5.13. The data obtained from the FMR and H_A measurements are listed in table XXV for three samples near the target composition. It can be seen that the $4\pi M$ values obtained by the collapse method agree well with those obtained from FMR and H_A data.

Excellent agreement is obtained between the FMR results and Faraday effect domain observations. Those deposits having $H_A - 4\pi M << 0$ have nearly horizontal domains. Conversely, those deposits with $H_A - 4\ M >> 0$ have vertical domains and stable bubbles can be formed and propagated. In those samples in which $H_A \approx 4\pi M$ bubbles and serpentine domains are frequently observed in zero external field. However, the bubbles distort from their cylindrical shape as the perpendicular bias field is increased.

The Neel temperature, T_N, and the compensation temperature, T_{comp}, of the films can also be determined from FMR measurements as a function of temperature (ref. 1). Values of T_N obtained from resonance measurements on films of YIG and GdIG agree well with reported values for bulk crystals. Measurement of $4\pi M$, T_N, and T_{comp} for the GaYGdIG films allows the approximate composition to be determined from published data (ref. 69). However, it is not essential to determine the exact composition if the goal is merely to establish deposition conditions and substrates that produce good bubble-domain material. It is sufficient, at least in the development stage, to relate deposition conditions, $4\pi M$, T_N, and T_{comp} to the bubble properties and make adjustments to improve these properties.

5.13 Anisotropy Field

It was pointed out in paragraph 5.12 that if H_A is known, $4\pi M$ can be determined from FMR data. Conversely, if $4\pi M$ is determined by the VSM or bubble collapse, H_A can be evaluated from the resonance results.

A simple technique described by Kurtzig and Hagedorn (ref. 68) has been used to provide a more direct measurement of H_A. The method consists of applying an in-plane dc magnetic field to a bubble-domain sample while observing the domain pattern by the Faraday effect. The anisotropy field is taken to be the field required to drive the domain magnetizations into the film plane.

The Faraday effect vanishes for the in-plane condition and so the domains disappear as the field reaches the value H_A. This technique has been used to measure H_A in the recent GaYGdIG films. The values of H_A shown in table XXV were obtained by this method. An additional benefit of this method is that it provides a check on the film uniformity. In the best deposits all the domains vanish in a field range that varies by only a few percent about the center value. In poorer samples considerable nonuniformity in H_A is observed over the area of the film. Thus, this method is useful as a qualitative evaluation of uniformity in the plane of the film.

5.14 Wall Coercive Force

A convenient method for measuring the coercive force, H_c, in bubble-domain materials is to determine the equilibrium spacing of two isolated bubble domains (ref. 70). A magnetic probe is used to push one bubble toward the other until the second one moves as a result of being repelled by the dipole-dipole interaction with the first. The coercive force is then calculated from the expression

$$H_c = 3\pi r_o^3 \, h \, (4\pi M)/8\ell_{12}^4 \qquad (13)$$

where r_o is the bubble radius, h is the plate thickness and ℓ_{12} is the equilibrium spacing. Coercivities of ~ 0.20 oe have been determined in the GaYGdIG films from measurements of the equilibrium spacing of bubbles. This method has the advantage that it can measure the local or microscopic coercivity rather than the average of the sample as is normally obtained from M-H loop tracers.

Samples that have very high wall coercivity are readily identified by the irregular shape of the domains as shown in figures 48 and 49. In such deposits the domains are essentially immobile unless bias fields or field gradients of several tens of oersteds are applied. Experimental evidence indicates that this high wall coercivity is a result of a large mismatch in the film substrate lattice constants; i.e., samples lying in Region II of the stress vs Δa plot (see Appendix) have high wall coercivities. Stein (ref. 71) has also observed a correlation between H_c in epitaxial GdIG and lattice constant mismatch between film and substrate. However, it is not clear that the coercivity that he measures is a wall coercivity since Comstock, et al, found good

agreement between experiment and a rotational coercivity model for epitaxial GdTbIG and GdIG on YAG (ref. 72).

The results on this contract and company-sponsored programs have shown conclusively that the domain wall coercivity in epitaxial films is affected by the magnitude of Δa.

5.15 Domain Wall Mobility

The propagation velocity of a ferromagnetic domain wall and the mechanisms that limit this velocity have been subjects of both fundamental and practical interest for many years. The recently demonstrated device potential of propagating cylindrical domains has produced an increased interest and activity in the study of wall motion. The equation of motion for a unit area of a 180-deg wall separating two antiparallel domains may be written as

$$m \frac{d^2x}{dt^2} + \beta \frac{dx}{dt} + \alpha x = 2MH(t) \tag{14}$$

for small amplitudes of the applied field H. Here x is the wall displacement along its normal, m is its effective mass per unit area, β is a damping constant, and α is a restoring force constant. The driving term H(t) is usually either a pulsed dc or a sinusoidally varying ac magnetic field that is applied along the directions of the antiparallel domains. If the effective mass and/or acceleration of the wall are/is small, the leading term on the left side of (14) can be neglected giving

$$\beta \frac{dx}{dt} + \alpha x = 2MH(t) \tag{15}$$

Wall motion described by equation (14) is called a resonance type, while that corresponding to equation (15) is referred to as a simple relaxation type of motion or viscously damped motion. If the applied field is larger than the wall coercive force, the wall motion is irreversible and it is no longer appropriate to retain the restoring force term αx. Further, if the wall velocity is essentially constant, the equation of motion reduces to

$$\frac{dx}{dt} = v = \frac{2M}{\beta} (H-H_o) \equiv \mu_w (H-H_o) \tag{16}$$

The threshold field H_o is essentially the coercive force. The constant μ_w is called the wall mobility and is expressed in units of cm-sec^{-1} Oe^{-1}. In general, the mobility μ_w is defined as the slope of the velocity vs drive-field curve; i.e., taking the field derivative of either equation (15) or equation (16) gives

$$\mu_w = \frac{dv}{dH} \tag{17}$$

Values of mobility are thus determined experimentally from the slope of the velocity-vs-field curves.

A variety of experimental techniques have been employed to obtain wall velocities and mobilities. In bubble-domain materials, mobilities have been measured primarily by two methods: (1) modulation of the equilibrium position of straight walls or of the equilibrium diameter of bubble domains (ref. 73), and (2) by dynamic collapse of bubble domains (ref. 74). The second method is considerably simpler experimentally than the first, but one must resort to the theoretical results of Thiele (ref. 37) to obtain the mobility from the experimental results. The procedure consists of applying a pulsed magnetic field superimposed on the static bias field. The magnitude and duration of the field pulse required to just collapse the bubble are the measured quantities.

In materials where the domain wall motion is well described by a simple relaxation or viscous damping model such that the velocity is a linear function of H as in equation (16), the mobility can be obtained quite simply from the theory. However, if there are nonlinearities in the velocity-field relationship, the determination of μ_w becomes a more complex problem.

In spite of the possible sources of difficulty in the bubble-collapse techniques, it is the most nearly standard mobility measurement technique for bubble-domain materials because of the simplicity of the experimental procedure. The wall mobility measurements performed on the GaYGdIG films have been obtained by this method.

A wall mobility of 1300 cm sec^{-1} Oe^{-1} has been measured in uncrazed films of (111) GaYGdIG/GdGaG of the approximate composition $Y_{2.4}Gd_{0.6}Ga_{1.0}Fe_{4.0}O_{12}$. This mobility is comparable to the highest values reported for either bulk or epitaxial garnets. (See Table II, ref. 82 for a comprehensive compilation of mobilities in bubble domain materials.) The wall velocity in the GaYGdIG also shows saturation effects similar to those observed in GaYIG at velocities above ~3000 cm/sec. One of the motivating forces for considering GaYGdIG for a bubble-material candidate was that it should have a high mobility. This expectation was based on the fact that both YIG and GaYIG have very low ferromagnetic damping losses as measured by FMR. Also, Gd^{3+} is one of the least damped rare-earth ions in the garnet structure. Thus, the magnetic damping losses in GaYGdIG should be less than in other bubble garnets containing ions such as Er^{3+}, Tb^{3+}, and Dy^{3+}, which have large damping constants.

The high μ_w value obtained in GaYGdIG, compared to garnets with heavily damped rare-earth ions, supports the above viewpoint.

5.16 Heat Treatment of Films

The distribution of gallium on tetrahedral and octahedral lattice sites in iron garnets has been shown to be quite sensitive to the thermal history of a sample (refs. 76 and 77). Although gallium preferentially occupies tetrahedral sites at low

temperatures, at higher temperatures there is an increasing tendency for gallium to shift from tetrahedral onto octahedral sites. A sample quenched from an elevated temperature carries the frozen-in high-temperature distribution, while one cooled slowly to below 500°C contains a maximum number of gallium atoms on tetrahedral sites. Since CVD films are normally cooled from the deposition temperature of ≈1200°C to ~600°C in 15 to 30 minutes, it was felt that the room-temperature magnetization might be characteristic of the high-temperature gallium distribution and that it could be altered by annealing and slow cooling. This would have the effect of decreasing the magnetization and increasing the domain size if the magnetization is dominated by the tetrahedral iron sublattice.

In order to evaluate the amount of quenching in our present growth procedure one-half of sample 2558 (the other half has been delivered to LRC) was held at 1300°C for 4 hr, then cooled at ~50°/hr to 500°C. The domain size increased dramatically as a consequence of this heat treatment, indicating a reduction in $4\pi M$, presumably as a consequence of the change in the gallium site distribution. The stripe domain width at zero field increased from 5 μm to 45 μm. Since the redistribution had been reported to be reversible in GaYIG the sample was subsequently raised to the film deposition temperature, held there for 2 hr, and then quenched in air to room temperature. The domain pattern was observed to have reverted to its original form, which it had prior to the slow cooling.

A limited number of additional experiments have shown that not all of the as-grown deposits have the quenched distribution. Heating and slow cooling of some deposits produces little or no change in the domain pattern, while others show changes considerably less dramatic than in 2558.

More extensive and systematic studies are required to adequately understand the effects of heat treating. However, the changes that have been observed indicate that it may be possible to eventually adjust the bubble diameter by controlled heat treatment.

5.17 Characteristics of a Typical Bubble-Domain Film of $Y_{3-z}Gd_zGa_xFe_{5-x}O_{12}$

The results of the characterization of a sample of (111) GaYGdIG/GdGaG, No. 2614Z3 are shown in table XXVI. This composition has excellent bubble-domain material parameters. The bubble diameter is in a range that provides bit densities of $\sim 10^6/in^2$. The magnetization is large enough so that detection problems should be reduced and the mobility is high enough to provide data rates in the MHz range. The only parameters that may require adjustment are the film/substrate lattice mismatch and the temperature coefficient. The $\Delta a^{\perp}$ value of +0.017Å is perhaps a little too large in view of the observations that crazing begins between $\Delta a^{\perp}$'s of +0.010Å and +0.020Å.

If it is desired to maintain GdGaG as the substrate, then a_f must be increased to reduce $\Delta a^{\perp}$. This will require an increase in z and/or a decrease in x. This composition change will also affect the temperature coefficient.

TABLE XXVI. – PARAMETERS OF AN EPITAXIAL {111} FILM OF $Y_{3-z}Gd_zGa_xFe_{5-x}O_{12}$ ON $Gd_3Ga_5O_{12}$

Parameter	Symbol	Value
Strained Lattice Mismatch	$\Delta a^{\perp}$	+0.017Å
Lattice Constant	a_f	12.374Å
Composition	$Y_{3-z}Gd_zGa_xFe_{5-x}O_{12}$	$z \simeq 0.6 \quad x \simeq 1.0$
Thickness	h	3.42μm
Collapse diameter	d_{col}	4.9μm
Collapse field	H_{col}	37 oe
Magnetization	$4\pi M_s$	160 gauss
Characteristic Length	ℓ	1.3μm
Wall energy	σ_w	0.26 ergs/cm^2
Neel Temperature	T_N	152°C
Compensation Temperature	T_{comp}	-150°C
Internal Field	$H_A - 4\pi M$	260 oe
Anisotropy Field	H_A	420 oe
Reduced Anisotropy Field	$\overline{H}_A = H_A/4\pi M$	2.6
Temperature Coefficient	TC	+1.6%/C°
Wall Mobility	μ_w	1300 cm sec^{-1} Oe^{-1}
Effective Anisotropy Constant	K_u	2700 ergs/cm^3
Wall Coercivity	H_c	0.2 Oe

It is encouraging that sample 2614Z3 which has higher z and lower x than 2606Z4, also has better temperature stability. Therefore, further increase in z and reduction of x may improve the temperature stability as well as reducing Δa. In any event, compositions close to 2614Z3 seem very promising at this time. If it is found that a significant shift in film composition is necessary to further reduce the temperature variation of d, it will be necessary to go to a different substrate such as DyGdGaG.

5.18 Bubble Propagation

Magnetic bubble-domain propagation has been demonstrated in several GaYGdIG films by using the field-access technique, which in this case employed a permalloy Y-bar pattern.

In order to understand how propagation is achieved, it is necessary to reexamine the basic bubble-material characteristics in conjunction with the permalloy pattern. When a bias field is applied normal to the bubble-domain film, the serpentine domains that exist at zero field will contract into cylindrical domains as the bias field increases. If the bias field is further increased, the cylindrical domains will contract and collapse. Bubble-domain devices are operated between the collapse and runout fields. Figure 54 shows the variation in the magnetic-domain pattern as a function of bias field. When a gradient is introduced in the bias field, the bubble domain will experience a force attempting to move it toward a position of reduced bias. Thus, bubbles tend to run down the field gradient, getting larger as they move. This movement across a gradient provides the basis for domain propagation. The rate of propagation is determined by the size of the gradient and the mobility of the bubble, measured in units of velocity per unit field gradient. The required field gradients may be created by current loops or by inducing magnetic poles in a soft magnetic overlay (refs. 31, 78). For garnet materials the small bubble diameters make loop fabrication extremely difficult if not impractical. Thus the best present propagation scheme consists of the Y-bar permalloy pattern.

Permalloy is a high-permeability material with a low coercive force, which makes it ideal for the propagation structure. The zero magnetostriction composition of 80-percent nickel and 20-percent iron (80/20 permalloy) is used in order to eliminate the effects of strain on the magnetic properties of the permalloy film. Adequate field gradients may be generated for bubble-domain motion by the application of small, in-plane magnetic fields with a permalloy film about 0.2 μm thick. Figure 56 shows the Y-bar pattern and propagation scheme. With this pattern, bubble-domain motion is achieved by means of a rotating magnetic field in the plane of the film. The magnetic field, as indicated by the arrows in the figure, polarizes the permalloy, causing field gradients that attract the domain from one position to the next. As a result, the bubble advances one repeat distance of the pattern with each 360° rotation of the field.

Standard photolithographic techniques were used to define the Y-bar pattern in permalloy films deposited by rf sputtering. To facilitate testing, an overlay technique was used in which the Y-bar pattern was fabricated on a glass slide and overlayed on the magnetic film. In some cases a drop of oil was used to hold the overlay close to the film surface. The GaYGdIG films had several regions that displayed no-error propagation on 1023 bit Y-bar patterns (10^6 bits/in^2 bit capacity), which covered an area of 33 by 33 mils. Data rates were limited to less than 60 Hz so that propagation characteristics over the entire pattern could be monitored visually.

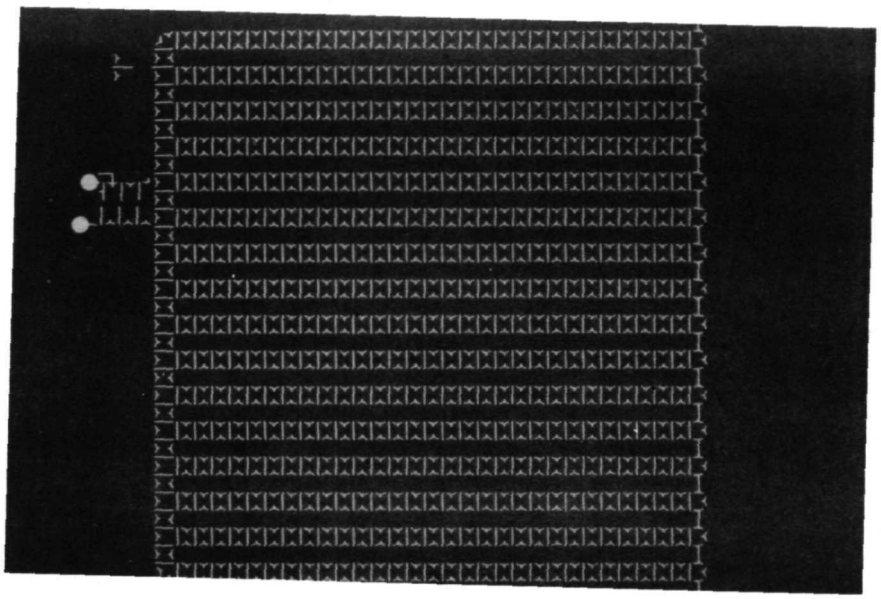

Figure 56. – Y-Bar Propagation Pattern

6.0 CONCLUSIONS

6.1 Program Results

The major accomplishment of this program was the achievement of epitaxial films of GaYGdIG that display good bubble-domain characteristics. The best film composition was $Y_{2.4}Gd_{0.6}Fe_{4.0}Ga_{1.0}O_{12}$. Epitaxial films of GdIG, YGdIG, and other GaYGdIG compositions were also grown; but their bubble properties were generally inferior to those in the $Y_{2.4}Gd_{0.6}Fe_{4.0}Ga_{1.0}O_{12}$ films. The major problem with these other compositions was extreme temperature sensitivity of the bubble diameter.

The best GaYGdIG films compare very favorably with other expitaxial bubble garnets prepared by CVD as shown in table XXVII. GaYIG has an excellent mobility and temperature coefficient but the magnetization is low and the bubbles are slightly small for the present state of the art for fabricating device structures such as Y-bar permalloy patterns. GaYIG compositions with higher magnetization have been grown, but then the bubbles are even smaller. Similarly, compositions with larger bubbles but lower magnetizations have been grown. GaErIG films, on the other hand, have very desirable magnetizations and bubble size but the bubbles have lower mobility and are more sensitive to temperature than those in GaYIG and GaYGdIG.

GaYGdIG is excellent in all categories except the temperature coefficient, but even here it appears to be adequate as judged by actual operation in the Y-bar shift register mode. Also, it is possible that the temperature coefficient can be improved by slightly modifying the composition to lower the compensation temperature. This is still being investigated. It has been more difficult to reproducibly achieve an exact desired composition for GaYGdIG than GaYIG and GaErIG. There are two reasons for this. The first is that it is more difficult to control the relative and absolute transport rates of four source materials (YCl_3, $GdCl_3$, $FeCl_2$, and $GaCl_3$) than three source materials (YCl_3, $FeCl_2$, and $GaCl_3$; or $ErCl_3$, $FeCl_2$, and $GaCl_3$). The second is that it is more difficult and time consuming to determine the exact film composition. Hence, fewer deposition runs are performed, or adjustments in deposition conditions are made, which are based on incomplete information.

Another achievement in the deposition portion of the program was the establishment of the necessary deposition conditions that produce smooth films. Solving the problem of film roughness was not only important to this program but to the entire garnet CVD technology. However, it would be even more satisfying to know what deposition mechanisms cause film roughness.

In the substrate work there were two major contributions. First, single crystals of several gallium garnets were grown, which had not been reported, at least when the program started. They were the unsubstituted garnets NdGaG and SmGaG and the mixed garnets NdGdGaG, NdSmGaG, and SmGdGaG. The Czochralski growth

TABLE XXVII. – A COMPARISON BETWEEN CVD BUBBLE GARNET FILMS

Parameters	GaYIG	GaErIG	GaYGdIG
Thickness	6.8 μm	4.0 μm	3.4 μm
Collapse diameter	3.4 μm	4.0 μm	4.9 μm
Collapse field	49 Oe	77 Oe	37 Oe
Magnetization	90 GAUSS	175 GAUSS	160 GAUSS
Characteristic Length	0.7 μ m	0.9 μm	1.3 μm
Wall energy	0.04 ergs/cm^2	0.2 ergs/cm^2	0.26 ergs/cm^2
Anisotropy Field	~600 - 700 Oe	660 Oe	420 Oe
Temperature Coefficient	-0.074%/C°	+3.7%/C°	+1.6%/C°
Wall Mobility	1500cm sec^{-1} Oe^{-1}	200 cm sec^{-1} Oe^{-1}	1300 cm sec^{-1} Oe^{-1}
Wall Coercivity	~0.1 Oe	~0.3 Oe	~0.2 Oe

of NdGaG was recently announced by Nielsen (ref. 34) although no experimental details were given. The mixed NdGdGaG work was important in that it revealed that it is difficult to grow good-quality crystals in mixed garnets where the rare earths (in this case Nd and Gd) are widely separated in the periodic table. Good-quality crystals can be obtained when the rare earths are adjacent or nearly adjacent as in the NdSmGaG and SmGdGaG crystals in this program and as in the DyGdGaG crystals (ref. 79).

Secondly, the thermal expansion data shows that variations in thermal expansion coefficient with gallium garnet compositions is less than 2 percent for the compositions investigated. This is important information in its own right and for applying the stress model.

In the characterization work, systematic procedures have been established (in conjunction with other programs) for evaluation of the substrates and for evaluation of the critical bubble-domain material parameters of the epitaxial garnet films. The X-ray measurements of film-substrate lattice mismatch and film evaluation by FMR techniques have proved to be extremely useful and powerful characterization tools. Through a combination of magnetic, X-ray, and optical measurements and theoretical results, it was possible to obtain a rather complete evaluation of the film characteristics, as was shown in table XXV.

The important substrate and film topography work has been done almost exclusively on this program. In particular the film-only topographs are believed to be the first reported for epitaxial bubble garnet films.

Although the stress model was first derived to explain GaYIG results, the validity and utility, of the stress model for CVD films has been clearly demonstrated on this program. It had been anticipated that the model would also apply to LPE films and this has now been confirmed experimentally by us as well as other investigators (Ref 86). Starting with the model and a set of material requirements it is possible to predict a film/substrate combination that will produce the required results. The material development then proceeds in a closed-loop sequence of film deposition, film characterization, deposition condition adjustment, and further deposition/characterization until the goal is reached. The film evaluation includes interpretation of results in terms of the model and provides data for decisions as to required deposition changes.

Finally, as proof of the device quality of the GaYGdIG films, it is important to note that bubbles were successfully propagated on a 1023-bit Y-bar permalloy shift register track.

6.2 Discussion of Bubble-Material Technology

To understand the significance of this work, we must look at the entire bubble-material technology. The following discussion is not intended as an exhaustive review but rather a brief survey and analysis of recent important bubble-material developments.

When this program started, it was apparent that the bubble technology was materials limited. Orthoferrites were inadequate for realizing the ultimate potential for low-cost, mass bubble memories. This should not detract from the historical role of orthoferrites in the outstanding original conception and development of the bubble technology by Bobeck, et al.

Then, at the Intermag Conference in April 1970, Bell Labs first announced that certain garnets were superior to the orthoferrites in their bubble properties. In particular, the bubble diameters of ~6 μm were much more attractive than the 25 to 100-μm diameter orthoferrite bubbles. These first bubble-domain garnet samples were obtained from bulk garnet crystals, grown by a flux technique (ref. 36), which were sliced and polished to approximately 25-μm thick wafers. It was of considerable practical and theoretical interest that a strong uniaxial anisotropy existed in these supposedly cubic garnets. However, bubble theory (ref. 37) specifies that the preferred wafer thickness should be ~1/2 the bubble diameter. For the ~6-μm bubbles observed in the garnets, this meant wafers only a few microns thick. This requirement was not too practical for unsupported wafers. The obvious solution would be epitaxial films if they could be fabricated with sufficient quality. The major concerns were to obtain epitaxial films of compositions with good bubble properties and with homogeneous composition and low defects.

Meanwhile at Autonetics we had already obtained the first epitaxial gallium-substituted yttrium iron garnet (GaYIG) films that had small "mobile" (paragraph 2.1) bubbles. Good-quality epitaxial films of bubble-domain material were first grown by the CVD method. As mentioned earlier (paragraph 2.1) the first announcement of this breakthrough was in May 1970 at the Symposium on Materials for Information Storage at the 137th National Meeting of the Electrochemical Society. A more complete account was given in November 1970, at the 3M Conference (ref. 22).

At the same 3M Conference, Shick, et al reported the first liquid-phase epitaxy (LPE) growth of epitaxial bubble garnets using a "tipping" technique (ref. 27). These first films apparently had severe composition gradients. However, at the Intermag Conference in April 1971, Levinstein, Landorf, and Licht (ref. 28) reported achieving high-quality LPE films by a "dipping" method; and, more recently, Geusic, et al (ref. 29) have reported on LPE films with low defect density.

The situation at this time is that both CVD and LPE films can apparently be grown with good bubble properties and sufficient quality to produce bubble devices. The only reservation in this statement is that more data is needed from dynamic testing of bubble nucleation and propagation behavior in the films. This may rule out compositions that appear to be acceptable, based on static property studies. In this regard, preliminary studies in this laboratory show that the GaYGdIG bubbles perform well, not only in their propagation behavior, but also in their nucleation (or generation) characteristics.

Which material and which growth technique will be used will depend partly on specific device requirements and design, partly on further developments of CVD and LPE toward mass production methods, and partly on further developments in other aspects of the bubble technology.

For example, GaErIG films have lower mobilities than GaYIG or GaYGdIG films. Therefore, their use in specific devices will depend on rate requirements, design of major/minor loop organization, or other design tradeoffs such as shift register length versus number of detectors and detector sense amplifiers.

We have already indicated that GaYGdIG films appear to be quite satisfactory in all categories, although more detailed studies of composition uniformity and defect density are still needed. However, to reproducibly produce films with strict composition control, certain modifications in reactor design willbe required.

There is one other significant difference between CVD and LPE films besides the fabrication techniques themselves. That is in the nature and source of anisotropy in the films. In the CVD films the anisotropy is stress induced as has been discussed in this report and elsewhere (ref. 22 and 48). Hence, it was very important to establish the stress model and to determine the film/substrate matching that would give a controlled amount of stress without producing cracked films. This anisotropy is not lost when the films are annealed. The anisotropy in the LPE films is partially growth induced and this contribution is reduced or removed entirely if the films are annealed at high temperatures (ref. 68). It is apparently the same mechanism that produces the uniaxial anisotropy in the bulk crystals grown by the flux method (ref. 42-44). In some of the as-grown materials the growth-induced anisotropy is almost an order of magnitude greater than presently reported stress-induced anisotropy (ref. 68). However, there appears to be a correlation between the magnitude of the growth-induced anisotropy and the domain wall mobility, even apart from the theoretical dependence of μw an $Ku^{-1/2}$. Those ions which give rise to a large growth-induced anisotropy also tend to have large ferromagnetic damping constants and hence low mobility. Thus in order to obtain high mobility LPE films it may be necessary to utilize a combination of growth- and stress-induced anisotropy.

The major requirement to obtain a significant anisotropy in the flux or LPE bubble materials is that they contain at least two rare-earth elements (or yttrium and one rare earth) in the dodecahedral sites although Axelrad and Callen have recently reported observing a growth-induced noncubic anisotropy arising from substitution on the tetrahedral sites in garnets (ref. 80). This has implications with respect to composition control just as in the more complex CVD compositions.

In a mood of speculation it would be interesting to see if the growth-induced anisotropy would be observed in CVD films if the deposition temperatures could be considerably lowered. As mentioned previously, the stress-induced anisotropy and other aspects (film cracking) of the stress model are applicable to LPE films as well as to CVD films.

6.3 Future Work

It has been demonstrated that epitaxial CVD garnet films can meet most or all bubble-domain material requirements. In particular the feasibility of GaYGdIG/GdGaG has been shown and further development of this material should be pursued.

Although the progress and accomplishments to date have been very promising, there are still problems that must be solved and new areas to be investigated before the bubble-domain technology can be fully realized.

In film fabrication, solution of the problem of process control will require certain modifications in reactor design and operation. These changes include accomodations for larger constant-temperature zones for each source material; and, possibly, a means of direct monitoring of transport rates rather than before-and-after weighings.

The other major area for future materials work is for more detailed studies of defects including:

(1) Observing domain nucleation and motion over large film areas to determine where there are defects that affect bubble properties.

(2) Mapping the defects observed in 1.

(3) Investigating the nature of these defects. For example, are they crystal defects such as bands, cores, or dislocations; are they gross point defects due to spurious nuclei or incorporation of particulate matter during deposition; or are they areas of local composition variation?

(4) Determining the source of the film defects. Are they due to defects in the substrate, to substrate polishing procedures, or to occurrences during the deposition?

(5) Further investigating and improving substrate growth, substrate polishing, and film growth processes to eliminate or minimize defects.

An example of one type of substrate imperfection propagated into the film is shown in figure 57a. When the polarizing microscope is focussed on the film so that the domains are observed by the Faraday effect, one can also see a number of either inclusions or voids that appear as the light and dark spots running diagonally across the photo. Some of these spots are in focus in figure 57a indicating they are in the film. Others, however, are out of focus, suggesting that they lie down in the substrate. If the microscope focus is changed slowly, these spots can be followed down into the substrate as shown in figure 57b. They lie along a plane that intersects the surface at a small angle and slopes downward toward the top of the photo. This plane is thought to be a low-angle grain boundary.

This region in the film acts as a barrier to domain motion and holds or "pins" portions of domains, which contact it. These effects are shown in figures 58a and 58b. At zero field, figure 58a, it can be seen that one serpentine domain is flattened against the defect line instead of crossing it and having its normal curved shape. As the field is increased (figure 58b) certain of the domains are pinned at the imperfection line and do not collapse into bubbles as they do away from this region. The field of view is moved slightly to the right in going from figure 58a to figure 58b. The longest strip domain in figure 58b has its ends pinned at the defect boundary and is thus prevented from collapsing into a bubble. These pinning points are the regions where this domain was flattened out in figure 58a.

If a rotating in-plane field such as is used for domain propagation is applied to this sample it is observed that bubbles are generated from certain regions of this defect. These bubbles fill up the adjacent areas and this type of uncontrolled generation would be disastrous to device operation.

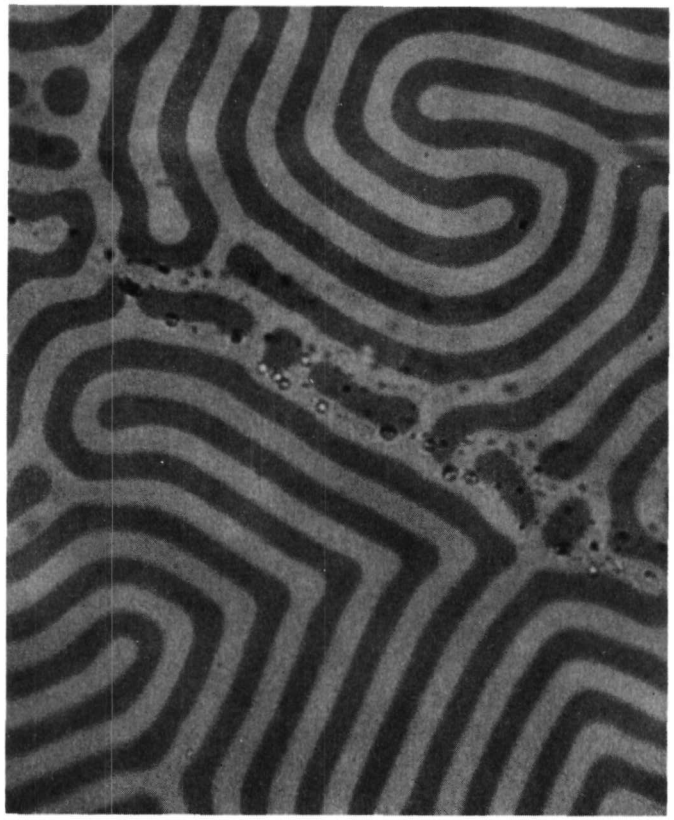

(a) Microscope focussed on film.

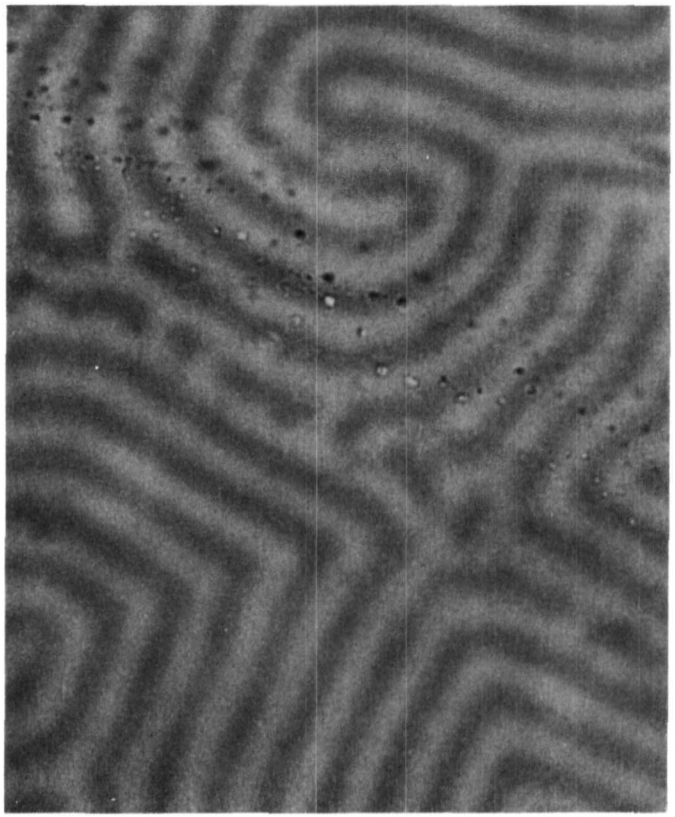

(b) Microscope focussed into substrate.

Figure 57. – An Imperfection in a Bubble Domain Film/Substrate Combination

(a) Zero external field.

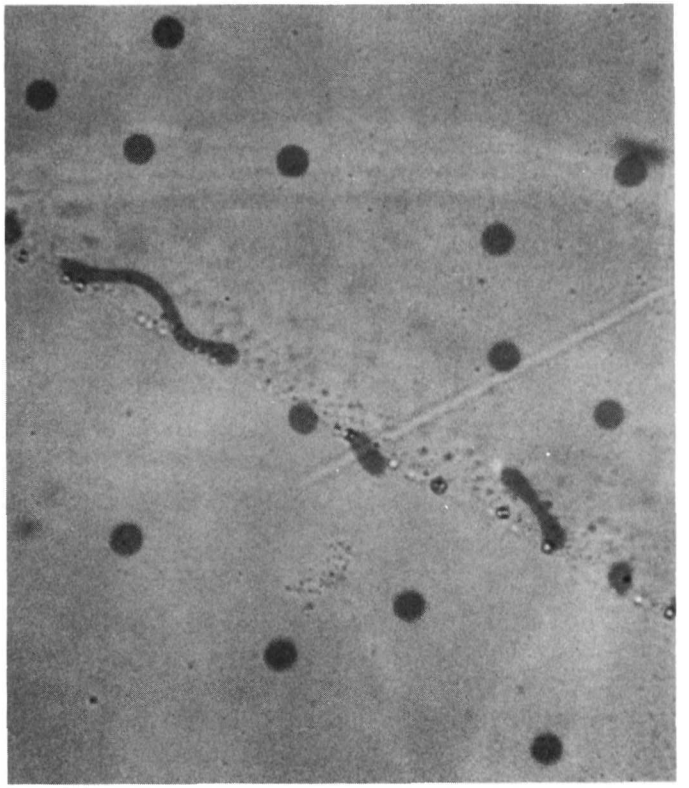

(b) External field = 70 oe.

Figure 58. – Effect of Imperfection on Magnetic-Domain Patterns

The effects of the defect described above are an example of the type of problems that must be solved in order to bring the bubble-domain technology to full realization. The occurrence of such defects must be related to the process variables and controls established to reduce such occurrences to an acceptable level.

It is worthwhile to note that this defect was not identified until the film was tested with a small shift register overlay. The domain behavior in the rotating in-plane field then revealed that something was wrong. Thus, it is useful, and even necessary, to investigate bubble-propagation characteristics as a material evaluation tool. It would be worthwhile to extend this technique to examine large film areas.

The X-ray topography techniques described previously represent another important tool for future studies. The most important task for the immediate future is an intensive effort to correlate the effects of film core and band structures on bubble-domain properties. There is some evidence from Faraday effect domain observations that the magnetic domain patterns in some films are affected by the band structure. If it is found that the core and band structures do have significant effects on bubble properties, then additional study of these defects will be necessary. Such studies would include determinations of the magnitude and spatial distribution (anisotropy) of the strains associated with the core and band structures. This can be accomplished using techniques similar to those already employed. Other techniques would be required to determine whether the incorporation of impurity atoms is an important factor in the development of the defect structures.

Heretofore, emphasis has been placed on elucidation of the major defect structures that are common to all of the substrates and are known to be propagated in the film; namely, the core and band structures. The nature and significance of substrate surface damage and other types of defects have not been given detailed consideration. Further topographic investigation of these defects and their influence on epitaxial films is also necessary.

The mechanism by which the CVD film is able to replicate the core and band structures of the underlying substrate is not understood. Further investigation of the interface region is required. Such studies would also lead to a better understanding of the film/substrate strain field that is an essential factor influencing bubble properties. It would be interesting to compare films grown by LPE with films grown by CVD to determine whether there are major differences in interfacial characteristics and in the replication of cores and bands. All of these subjects are amenable to analysis by X-ray diffraction methods.

Other areas must also be investigated more thoroughly. Of particular importance, the temperature sensitivity of the domain size must be carefully evaluated as a function of film composition for the purposes of minimizing temperature effects.

APPENDIX

A STRESS MODEL FOR HETEROEPITAXIAL MAGNETIC OXIDE FILMS GROWN BY CHEMICAL VAPOR DEPOSITION

(Published in Materials Research Bulletin Vol. 6, Page 1111 Nov. 1971)

P. J. Besser, J. E. Mee, P. E. Elkins and D. M. Heinz
Autonetics Division of North American Rockwell, Anaheim, CA 92803

ABSTRACT

A simple physical model is presented, which predicts the sign and magnitude of stress in heteroepitaxial films. The model explains experimental observations of ferromagnetic resonance, domain structure, and crazing in magnetic oxide films grown by chemical vapor deposition (CVD) on nonmagnetic substrates. It provides a means of predicting and developing compatible film-substrate combinations for epitaxial bubble domain materials utilizing a stress-induced uniaxial magnetic anisotropy. A basic result of the model, the conditions under which films can be grown in compression, has been verified experimentally for CVD iron garnets.

Introduction

It is a well-established fact that thin solid films deposited onto substrates of dissimilar materials are usually in a state of mechanical stress. In the case of epitaxial metal oxide films grown by chemical vapor deposition (CVD), many authors have reported on stress observations and effects in the films (1-10). The stress manifested itself in film-substrate bending, film cracking, changes in the film lattice constant; or, for magnetic oxides, in magnetostrictive effects. These investigators recognized that both thermal expansion and lattice constant mismatch between film and substrate should influence the magnitude and sign of the film stress. However, most of the observations led to the conclusion that thermal expansion mismatch was the dominant factor in determining film stress. The basis for this conclusion was primarily the occurrence of tensile stress in films that were more expansive than the substrate, but whose lattice constant was larger than that of the substrate so that the lattice mismatch, considered alone, should have produced compression. Although Pulliam (3) reported that spinel ferrites on MgO could be grown in either tension or compression, he was discussing the situation where the substrate was more expansive than the film. It will be shown that, under certain conditions, films in compression can also be obtained when the substrate is less expansive than the film.

Experimental results obtained by the authors on a variety of epitaxial magnetic oxide films have shown that the film-substrate lattice constant mismatch is vitally important in determining the sign and magnitude of stress in these deposits. A very significant observation is that only when the lattice mismatch exceeds certain critical values does the thermal expansion mismatch determine film stress.

A simple physical model has been developed to explain these experimental observations. The model predicts the sign and magnitude of film stress from data on room-temperature lattice mismatch and thermal expansion mismatch. This model will be presented in the following section. In the third section, experimental observations based on physical integrity, magnetic domain patterns, and ferromagnetic resonance (FMR) data will be compared with stress data computed from the model. Sime important consequences of the model and further experimental verification will be discussed in the fourth section.

The Model

Consider the heteroepitaxial growth of a cubic film material on a single crystal cubic substrate at elevated temperatures. In general, the lattice constant of the film, a_f, will differ from that of the substrate, a_s, at the growth temperature. For the purposes of the model, it is assumed that this mismatch in lattice constants is accommodated in one of two ways. For small values of lattice constant difference, the misfit is assumed to be taken up by the homogeneous elastic deformation of the film so that it fits to the substrate, which is considered to be massive compared to the film so that it does not deform. This range where the lattice mismatch is accommodated by elastic deformation will be referred to as Region I. As the mismatch is increased, limiting values are reached beyond which the stress is relieved by some mechanism, possibly the formation of misfit dislocations at the interface. This second range of lattice mismatch will be referred to as Region II.

The initial state of stress and that which is developed in the film upon cooling to room temperature are considerably different for the two regions. In Region I, the film is strained so that its lattice constant parallel to the substrate surface matches that of the substrate. The film then is in a stressed state at the deposition temperature, the sign and magnitude of which depend on the lattice mismatch and the elastic constants of the material at that temperature. The difference between the thermal expansion of the film, α_f, and that of the substrate, α_s, will modify the film stress as the sample is cooled. However, if elastic behavior persists over the entire temperature range, the stress level and sign at room temperature will depend only on the film-substrate lattice mismatch and the elastic constants of the film at room temperature. In this case the film stress is given by:

$$\sigma_I = \frac{Y}{1-\mu}\left(\frac{a_s - a_f}{a_f}\right) \qquad (1)$$

where Y and μ are the Young's modulus and the Poisson ratio of the film. The values of a_s and a_f in (1) are taken to be the bulk values at $300^{\circ}K$.

In Region II, it is assumed that the film takes on its equilibrium free lattice constant away from the interface so that it is essentially unstressed at the deposition

temperature. The film is considered to behave elastically on cooling so that stress develops as a result of the differential thermal expansion of the film and the substrate. The stress in this case is given by:

$$\sigma_{II} = \frac{Y}{1-\mu} (\alpha_f - \alpha_s) \Delta T \qquad (2)$$

where ΔT is the difference between deposition temperature and room temperature.

Thus, the two situations lead to different predictions of the film stress at room temperature. In Region I, the stress depends only on the room temperature lattice constant mismatch, whereas in Region II it is due only to thermal expansion mismatch. In both (1) and (2), it is assumed that the film behaves elastically between deposition and room temperature. The difference arises from the initial stress condition of the film at deposition temperature.

As an example, consider the case where the film is more expansive and has a larger room-temperature lattice constant than does the substrate; i.e., $\alpha_f > \alpha_s$ and $a_f > a_s$. This situation is shown schematically in Figure 1. Equation (1) predicts that the film will be in compression ($\sigma_I < 0$) whereas equation (2) predicts tension ($\sigma_{II} > 0$). Clearly, it should be possible to distinguish between the two situations by determining the film stress.

The results of the model are shown in Figure 2 for the condition $\alpha_f > \alpha_s$. In Region I, the film stress is linearly dependent on the lattice mismatch, begin tensile for $a_s > a_f$ and compressive for $a_f > a_s$. The boundaries of Region I are represented by Δa_1 and Δa_2, the limiting values of the lattice constant mismatch $\Delta a = (a_s - a_f)$. Thus, Δa_1 corresponds to the limiting state of tension and Δa_2 corresponds to the limiting state of compression. For $|a_s - a_f| > \Delta a_1$ or Δa_2 the stress is tensile having a value σ_{II} that is independent of $(a_s - a_f)$, and is determined by equation (2). In Figure 2, it has been assumed that the maximum values of stress attained in Region I, σ_1, and σ_2, are somewhat larger than σ_{II}. The transition from Region I to Region II is shown as being discontinuous, whereas in an actual case a more gradual transition between the two regions may well occur. Other diagrams similar to Figure 2 can be constructed from the model for different situations of interest such as $\alpha_s > \alpha_f$.

It should be pointed out that certain restrictions on the thermal expansion mismatch are implicit in the model and in its representation by Figure 2. If α_f and α_s differ too greatly, the films will always be either in tension ($\alpha_f \gg \alpha_s$) or compression ($\alpha_s \gg \alpha_f$), although there may still be regions where the magnitude of σ shows some dependence on $(a_s - a_f)$. Alternatively, when $\alpha_f = \alpha_s$ the thermal expansion stress, σ_{II}, will be zero. As a consequence of the experimental observations described in the following section, it has been found that the model is valid for CVD spinel ferrites and iron garnets if $|\alpha_f - \alpha_s| \leq 1\text{-}2 \times 10^{-6}\ ^oK^{-1}$. This condition ensures that $(a_s - a_f)$ at the deposition temperature does not differ drastically from its value at room temperature.

The relationship of the model to classical epitaxial theory has not been explored. Agreement of the model with the experimental observations presented in the following

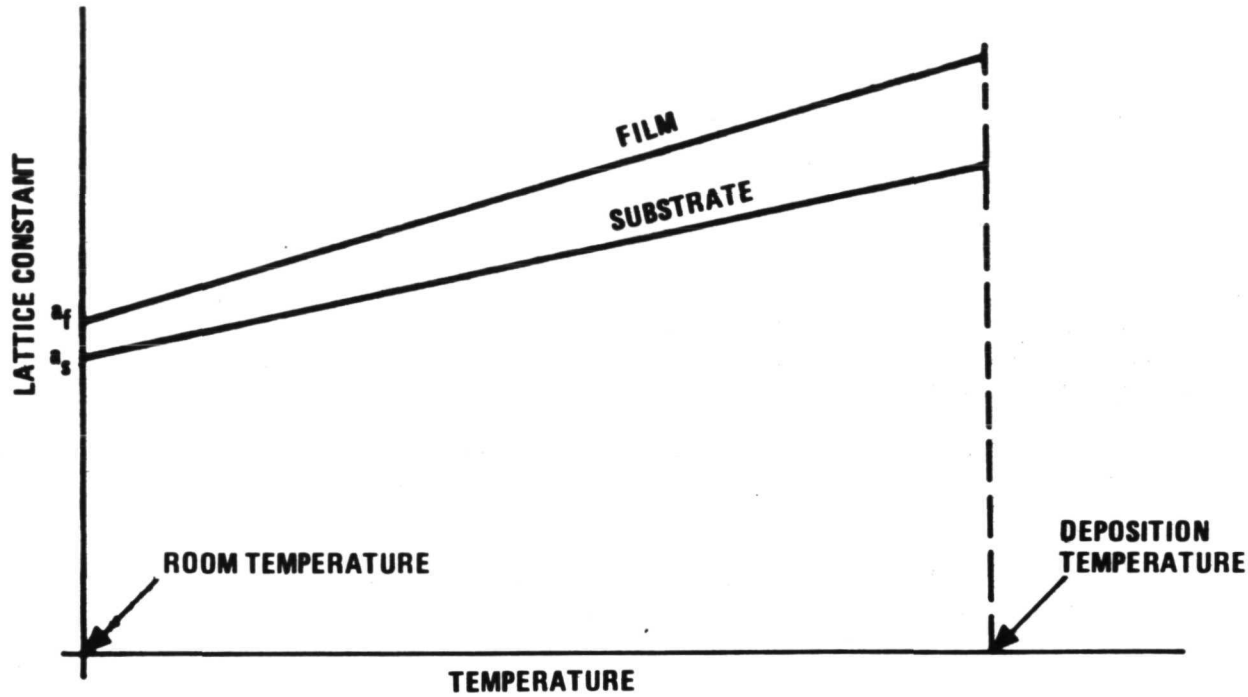

Figure 1. Temperature Variation of the Unconstrained Lattice Constants, of a Film and a Substrate for $a_f > a_s$, $\alpha_f > \alpha_s$

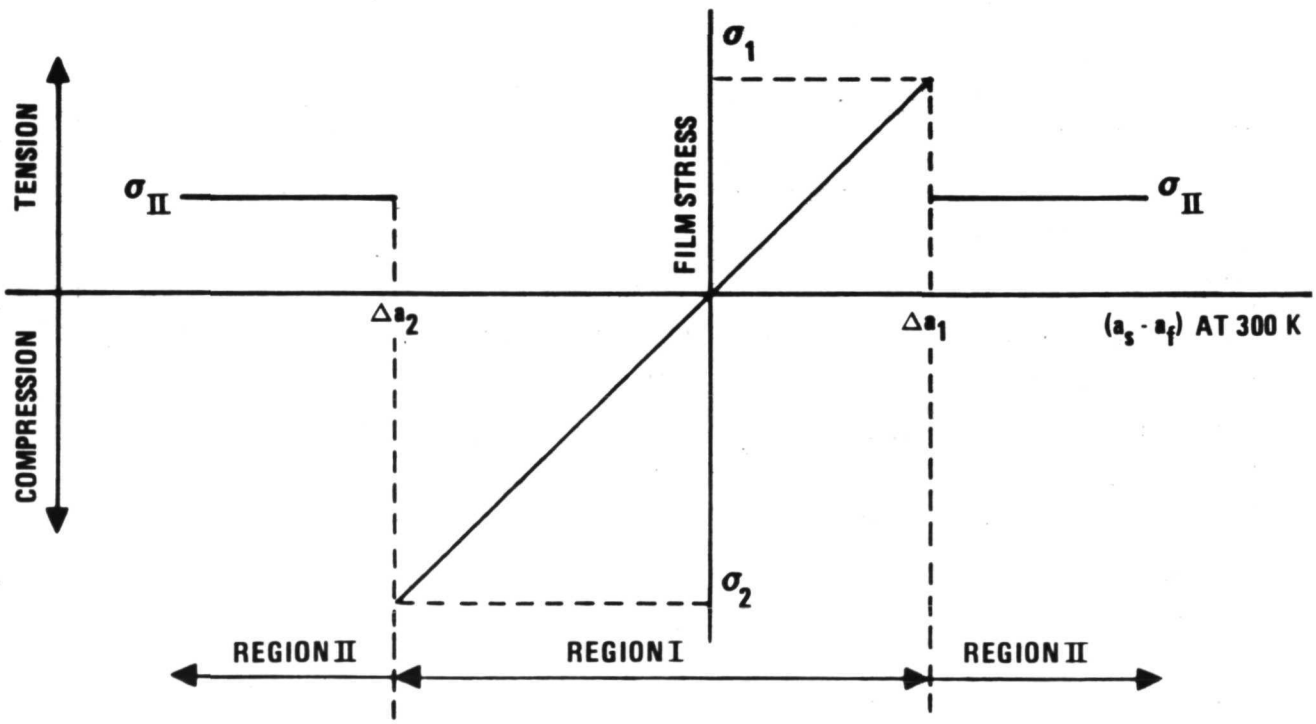

Figure 2. Idealized Stress Model for the Situation $\alpha_f > \alpha_s$, $\sigma_{II} < \sigma_1, \sigma_2$

sections has been taken as ample justification for its validity and usefulness. It is of interest to note, however, that Van der Merwe's theory of epitaxial films (11) does predict a transition from a coherent to a noncoherent state at a limiting value of lattice misfit.

Comparison with Experimental Observations

The model that has been described was developed over a period of time as a consequence of a large number of experimental observations on epitaxial films of ferrimagnetic oxides such as spinel ferrites and iron garnets. It has been successful in explaining most of the observed stress-related phenomena in such films and in predicting compatible film-substrate combinations for specific applications such as epitaxial bubble-domain materials (10).

Since yttrium iron garnet (YIG)* is one of the best characterized and most useful ferrimagnetic materials, it is an ideal vehicle for the testing and demonstration of the model. When YIG is grown on rare-earth-gallium or -aluminum garnets, the condition of Figure 2 that $\alpha_f > \alpha_s$ is satisfied, since YIG is more expansive than the gallium or aluminum garnets (12). The discussion to follow will be concerned primarily with YIG films on various nonmagnetic garnet substrates. The conclusions, however, have much broader application than to just these materials.

Single crystal YIG films were grown by CVD methods on nonmagnetic rare-earth-gallium and -aluminum garnet substrates identified in Table I. The deposits were characterized in terms of their ferromagnetic resonance (FMR) properties, magnetic domain structure, film-substrate lattice mismatch, and film crazing. Pertinent material parameters of YIG and substrates, which are referred to in the following discussion, are shown in Table I. The substrate crystals were grown by the Czochralski method.

Table I. Properties of YIG and Garnet Substrates

A. YIG ($300^{o}K$)		
Parameter	Value	Reference
Magnetization	$4\pi M = 1780$ gauss	Measured(1)
Anisotropy constant	$K_1 = -6000$ ergs/cm^3	14
Gyromagnetic ratio	$\gamma = 2.8$ MHz/oe	14
Magnetostriction constants	$\lambda_{111} = -2.4 \times 10^{-6}$, $\lambda_{100} = -1.4 \times 10^{-6}$	15
Lattice constant	$a = 12.376$ Å	12
Thermal expansion coefficient	$\alpha = 10.4 \times 10^{-6}\ ^{o}K^{-1}$	12
Young's modulus	$Y = 2 \times 10^{12}$	16, 17
Poisson ratio	$\mu = 0.29$	16, 17

*Other garnet compositions can be abbreviated conveniently in the same manner as for YIG; i.e., GdGG for $Gd_3Ga_5O_{12}$, SmGG for $Sm_3Ga_5O_{12}$, etc.

Table I. Concluded

B. Substrate Garnets		
Material	a (A) (2)	x 10^6 ($^oK^{-1}$) (3)
$Nd_3Ga_5O_{12}$ (NdGG)	12.506	9.2
$Sm_3Ga_5O_{12}$ (SmGG)	12.439	9.2
$Gd_3Ga_5O_{12}$ (GdGG)	12.383	9.2
$(YGd)_3\ Ga_5O_{12}$ (YGdGG)	12.367	9.2
$(DyGd)_3Ga_5O_{12}$ (DyGdGG)	12.359	9.2
$Gd_3\ (A\ell Ga)_5O_{12}$ (GdAℓGG)	12.355	9.2
$Tb_3Ga_5O_{12}$ (TbGG)	12.346	9.2
$Er_3Ga_5O_{12}$ (ErGG)	12.273	9.2
$(NdY)_3\ A\ell_5O_{12}$ (NdYAG)	12.011	8.6
$Y_3A\ell_5O_{12}$ (YAG)	12.008	8.6

1. Epitaxial film - by vibrating sample magnetometer.
2. All values except YAG from Ref 13.
3. GdGG and YAG values from Ref 12. Values for other gallium and aluminum garnets assumed to be approximately the same as GdGG and YAG.

FMR Results

Quantitative data on film stress was obtained from FMR experiments at 9.1 GHz. The anisotropy field, H_A, perpendicular to the plane of a stressed film is (10)

$$H_A = (2K_1 - 3\sigma\lambda_{100})/M \tag{3}$$

for a $\{100\}$ deposit and

$$H_A = (-4K_1 - 9\sigma\lambda_{111})/3M \tag{4}$$

for a $\{111\}$ deposit where the symbols in (3) and (4) are defined in Table I. From measurement of the perpendicular resonance condition, the anisotropy field can be determined from the expression

$$H_A = \frac{\omega}{\gamma} + 4\pi M - H_o. \tag{5}$$

Equation (5) neglects any contributions to the resonance condition from exchange or microwave demagnetizing effects. The resonance samples were all disks 0.5 mm in diameter and ~1-μm thick so that such effects would be small and reasonably constant (18).

Values of film stress were calculated from the FMR measurements on the CVD YIG films using the data of Table I and equations (3), (4), and (5). The stress obtained in this way is shown in Table II along with values of σ_I and σ_{II} calculated from equations (1) and (2).

Table II. Calculated Values of Film Stress for ~1-μm Thick YIG Deposits

Epitaxial Combination	$(a_s - a_f)$ (Å)	Stress ($\times 10^9$ dynes/cm^2)		
		σ_I	σ_{II}	FMR Data
1. YIG/NdGG	+0.230	+52	+4	+8.3
2. YIG/SmGG	+0.063	+14	+4	+14
3. YIG/GdGG	+0.007	+1.6	+3.9	+2.0
4. YIG/DyGdGG	-0.017	-3.9	+4	-4.4
5. YIG/TbGG	-0.030	-6.9	+4	-7.6
6. YIG/ErGG	-0.103	-23	+4	+2.6
7. YIG/NdYAG	-0.365	-83	+5	+4.8
8. YIG/YAG	-0.368	-84	+5.5	+5.7

Film deposition was performed at 1450°K, so the value of $\Delta T = 1150^{\circ}K$ was used for the thermal expansion calculations.

The behavior of the film stress as measured by FMR is in excellent agreement with that predicted by the model. The sign and magnitude of the stresses in samples 2 to 5 are close to the lattice mismatch values, σ_I, while samples 1, 6, and 7 have tensile stresses close to the thermal expansion values, σ_{II}. Of particular significance, the FMR data show that samples 4 and 5 are in compression.

These data indicate that $0.063\text{Å} < \Delta a_1 < 0.230\text{Å}$ and $-0.103\text{Å} < \Delta a_2 < -0.030\text{Å}$ for YIG films ~1-μm thick. It is particularly noteworthy that in Region I significant compressive stress can be obtained. This occurs if the lattice mismatch at deposition is large enough so that it is not fully compensated by stress-relieving thermal expansion effects.

Domain Observations

Since YIG has negative magnetostriction and a negative cubic anisotropy constant, the magnetic domain structures in this material give considerable useful qualitative information on the stress configuration.

The samples on which domain observations were performed were thicker (~3 to 5 μm) than those used for FMR studies so that the domain size and contrast would be suitable for viewing at convenient magnifications by the Faraday effect or the magnetic birefringence effect (19). The substrates used in the domain studies were YAG, ErGG, GdAℓGG, GdYGG, GdGG, and NdGG.

The magnetostrictive contribution to the magnetic anisotropy in YIG makes the direction perpendicular to the film plane an easy axis if the film is in tension, and a hard axis if the film is in compression (see equations (3) and (4)). The values of the magnetization, anisotropy constant, and wall energy for unstressed YIG are such that the domain magnetization should lie in the film plane for {100} and {111} deposits, which are only a few microns thick (20). Obviously, {110} deposits should also have in-place magnetization, since {111} directions lie in the film plane. The occurrence of a domain pattern where the domains have a component of magnetization normal to the film plane is thus an indication that the film is in tension.

Deposits of YIG on YAG (YIG/YAG) invariably have domains that are perpendicular to the film plane (6) showing that the films are in considerable tension. This is consistent with the assignment of this combination to Region II on the basis of the FMR results. Similar domain patterns are also observed in {111} films of YIG/NdGG and YIG/ErGG. The domains in both of these samples appear to be nearly normal to the film plane, as judged by the absence of any crystallographic preference for the domain wall directions and the occurrence of many single-walled domains.

The domain patterns of YIG/GdGG also show a component of magnetization normal to the film plane for {100}, {110}, and {111} orientations. The indications, however, are that the domains are inclined at an oblique angle to the film, since parallel-plate structures are typically observed with definite wall orientations related to crystallographic directions. For example, the domain walls are parallel to the < 110 > in {100} deposits. In-plane M-H loops have verified that there is a component of M parallel to the film surface in samples of YIG/GdGG.

The YIG films on the GdYGG and GdAℓGG substrates had in-plane domains that could be observed by the magnetic birefringence. These domains have a characteristic spike-like appearance similar to that observed in thin Ni-Fe films.

On the basis of these domain observations and the FMR results, it is concluded that YIG/YAG, YIG/ErGG, YIG/NdGG, and YIG/GdGG are in tension; while YIG/GdYGG and YIG/GdAℓGG are in compression. The first three combinations lie in Region II while the latter three are in Region I.

Film Cracking

The well-known tendency of epitaxial films to crack or craze can also be related to the stress model. The fracture stress of single crystal thin films of magnetic oxides appears to be a function of the film thickness. Deposits of YIG on garnet substrates are seldom crazed if the film thickness is ≤1 μm. Of the samples listed in Table II, only No. 2 is crazed. However, for film thicknesses of ~5μm, deposits of YIG/YAG, YIG/ErGG, and YIG/NdGG are all crazed. Generally the severity of the cracking increases with increasing film thickness. On GdGG, sound YIG films can be grown up to ~10-μm thick but beyond this thickness, cracks begin

to occur. Deposits of YIG/GdYGG and YIG/GdAlGG show no tendency to craze for deposits several μm thick.

The above observations in conjunction with the domain pattern data show that the crazing is a consequence of excessive tensile stress. The domain patterns in crazed films always indicate that the film is in tension. In the garnet system under consideration, combinations in Region II are almost invariably crazed when the film thicknesses are~5 μm. Samples in the tensile range of Region I may or may not craze depending on the film stress and the film thickness. No crazing has been observed for samples in the compressive range of Region I.

Discussion

The quantitative agreement between the model and the FMR results is quite good in view of the assumptions made in arriving at the stress values. The agreement is best in the range of greatest interest; i.e., Region I. Possible sources of discrepancy between the predicted and the observed stress values in Region II are: differences in substrate quality and thermal expansion, incomplete stress relief at deposition temperature, and inelastic behavior during the cooling from deposition temperature. The most significant point is that there does exist a region where the stress is determined essentially only by the room temperature lattice mismatch in a predictable fashion. An important consequence of this situation is that if the magnitude and sign of $(a_s - a_f)$ are suitable, the film can be left with residual compressive stress at room temperature. Such is the case for samples 4 and 5 of Table II.

The domain pattern and crazing observations on YIG/YAG and YIG/GdGG were initially rather misleading. The strong component of magnetization normal to the film plane indicated that these films were in tension, whereas the lattice mismatch predicted compression on YAG and zero stress on GdGG, whose room-temperature lattice constant was reported to be identical to that of YIG (12). Additionally, YIG films on YAG were crazed when more than~1.5-μm thick, whereas uncrazed films several microns thick could be grown on GdGG (6). Therefore, it appeared that thermal expansion mismatch was the dominant factor in determining the film stress, and the differences between the domain patterns and crazing for YIG/YAG and YIG/GdGG were attributed to the greater expansivity of the latter. (See Table I). Subsequently, however, YIG was grown on substrates such as GdYGG whose lattice constant is only slightly smaller than YIG, and the domain magnetizations were in the plane of the film, indicating that the film was in compression. This led to the understanding that the transition to Region II was occurring at Δa_2, which accounts for the tensile stress in YIG/YAG. Precision lattice constant measurements on the Czochralski-grown crystals of GdGG determined that the lattice constant of this material is 12.383A rather than the 12.376A obtained on polycrystalline samples (13). Therefore, a tensile stress would be expected in YIG/GdGG due to the lattice constant mismatch, and this combination represents the situation of Region I. Considerable additional experimental data has been collected from domain observations on samples of gallium-substituted YIG (Ga:YIG) grown for bubble-domain applications. For example, deposits of Ga:YIG with $a_f \approx 12.355$A grown on {111} GdGG showed vertical strip and bubble domains, while those grown on {111} TbGG had the magnetization lying in the plane of the film. These domain observations, although qualitative, offer confirming evidence for the validity of the model.

One of the first indications that the thermal expansion mismatch model was inadequate for explaining stresses in some of the films came with the observations of film crazing. Pure YIG could be grown several microns thick on GdGG without crazing. However, even small substitutions of Ga in YIG/GdGG invariably produced crazing in films~5-μm thick, and the severity of the crazing increased with Ga content. This is just the reverse of the behavior expected on the basis of thermal expansion mismatch, since the addition of Ga to YIG should reduce its expansion and produce a better expansion match to the substrate. On the basis of the model, the crazing behavior is understood, since $(a_s - a_f) > 0$ for YIG/GdGG and the addition of Ga decreases a_f and increases the tensile stress in the film, producing crazing.

The problem of crazing represents a real and severe limitation on the allowable magnitude of tensile stress in films. In Region II, CVD iron garnet films on gallium or aluminum garnet substrates are usually crazed if the films are more than 2- or 3-μm thick. Therefore, it is inadvisable to obtain tension in this system by utilizing lattice mismatches greater than Δa_1 or Δa_2. As a general rule of thumb, $\Delta a_1 \leq 0.010$A is advisable for films in tension. Somewhat larger mismatches appear to be tolerated in compression, as indicated by the observations on YIG/GdAlGG.

There are indications that the limiting mismatches Δa_1 and Δa_2 are dependent on film thickness, but the present data is insufficient to verify this point.

Although the examples have been restricted primarily to a single material, YIG, the model has been found to be applicable to a variety of CVD magnetic oxide films and is expected to be valid for any system that satisfies the conditions of elastic behavior. The model has proved very useful in predicting compatible film-substrate compositions for epitaxial bubble-domain materials and in interpreting the domain structure in these materials. The verification that a range of compression exists is particularly significant, since materials with positive magnetostriction can be grown in compression to produce the required uniaxial anisotropy. In particular, {111} deposits of TbIG grown on substrates with $a_s < a_f$ are in compression and show mobile bubble domains.

Summary

A simple model of stress in heteroepitaxial CVD magnetic oxide films has been developed. The most significant result is that the film stress is determined solely by the room-temperature lattice constant mismatch between film and substrate for small mismatches. Predictions of the model have been verified by growing films in compression as well as tension. The model is most applicable when thermal expansion coefficients for the film and substrate are reasonably well matched; e.g., $|\alpha_f - \alpha_s| \leq 1\text{-}2 \times 10^{-6}/^{o}K$. The validity of the model for CVD magnetic oxide films has been demonstrated by ferromagnetic resonance measurements and by observations of magnetic-domain structures and flim crazing.

The model provides a means of predicting film-substrate combinations that are useful for bubble-domain materials utilizing a stress-induced uniaxial magnetic anisotropy.

In agreement with the results of the model, iron garnet films with positive magnetostriction have been grown in compression and exhibit mobile bubble domains.

Acknowledgement

Portions of this work were supported by U. S. Army Electronics Command, Ft. Monmouth, New Jersey; the National Aeronautics and Space Administration, Langley Station, Virginia; and the U. S. Air Force Materials Laboratory, Dayton, Ohio.

The authors wish to express their gratitude to S. B. Austerman, J. L. Kenty and A. J. Hughes for their critical reading of the manuscript and for their many helpful suggestions.

References

1. R. E. Cech and E. I. Alessandrini, Trans. Am. Soc. Metals, 51, 150 (1959)

2. H. Takei and S. Chiba, J. Phys. Soc. Japan 21, 1255 (1966)

3. G. R. Pulliam, J. Appl. Phys. 38, 1120 (1967)

4. M. W. Vernon and F. J. Spooner, J. Material Sci. 4, 112 (1969)

5. F. J. Spooner and M. W. Vernon, J. Material Sci. 4, 734 (1969)

6. J. E. Mee, G. R. Pulliam, J. L. Archer and P. J. Besser, IEEE Trans. Magnetics 5, 717 (1969)

7. R. Zeyfang, J. Appl. Phys. 41, 3718 (1970)

8. B. F. Stein, J. Appl. Phys. 42, 1806 (1971)

9. R. L. Comstock, E. B. Moore and D. A. Nepala, IEEE Trans. Magnetics 6, 558 (1970)

10. D. M. Heinz, P. J. Besser, J. M. Owens, J. E. Mee and G. R. Pulliam, J. Appl. Phys. 42, 1243 (1971)

11. J. H. van der Merwe, J. Appl. Phys. 41, 4725 (1970)

12. S. Geller, G. P. Espinosa and P. B. Crandall, J. Appl. Crystallography 2, 86 (1969)

13. L. A. Moudy, Private Communication

14. Handbook of Microwave Ferrite Materials, W. H. Von Aulock, ed. (Academic, New York, 1965)

15. S. Iida, J. Phys. Soc. Japan 22, 1201 (1967)

16. E. G. Spencer, R. T. Denton, T. B. Bateman, W. B. Snow and L. G. Van Uitert, J. Appl. Phys. 34, 3059 (1963).

17. T. B. Bateman, J. Appl. Phys. 37, 2194 (1966)

18. J. E. Mee, P. J. Besser and F. A. Pizzarello, Final Report, Epitaxial Growth of Ferromagnetic Garnets, Tech. Rept. AFAL-TR-70-194. Air Force Avionics Laboratory, Dayton, Ohio.

19. J. F. Dillon, J. Appl. Phys. 29, 1286 (1958)

20. G. R. Pulliam, J. Appl. Phys. 38, 1120 (1967)

REFERENCES

1. J. E. Mee, P. J. Besser and E. C. Whitcomb, "Investigation of Single Crystal Ferrite Thin Film", Interim Report, Contract NAS12-522, NASA-ERC, Cambridge, Mass., Feb. 1970.

2. Ga. A. Zaionchkovskii, V. V. Lyukshin, and Yu. G. Saksonoo, "The Epitaxial Formation of Ferrites in Chemical Transport Reactions", Inorganic Materials P1782-1784, translated from Investiya Akademii Nauk USSR, Neorganicheskie Materialy 3, 2048 (1967).

3. J. E. Mee, J. L. Archer, R. H. Meade and T. N. Hamilton, "Chemical Vapor Deposition of Epitaxial YIG on YAG and Epitaxial GdIG on YAG," Appl. Phys. Letters, 10, 289 (1967).

4. J. E. Mee, "Chemical Vapor Deposition of Epitaxial Garnet Films," IEEE Trans. Magnetics, MAG-3, 190 (1967).

5. J. E. Mee, G. R. Pulliam, J. L. Archer, and P. J. Besser, "Magnetic Oxide Films," IEEE Trans. on Magnetics, MAG-5, 717 (1969)

6. J. E. Mee, P. J. Besser, and F. A. Pizzarello, "Epitaxial Growth of Ferromagnetic Garnets", Technical Report AFAL-TR-70-194, Sept. 1970.

7. P. J. Besser, "Orientation Dependence of Spin Wave Spectra in Single Crystal YIG Films," J. Appl. Phys. 42, 1570 (1971).

8. J. H. Collins, N. Rubino, H. R. Zapp, J. E. Mee, F. A. Pizzarello, G. R. Pulliam and T. N. Hamilton, "Shear Wave Generation at Microwave Frequencies Utilizing Epitaxial YIG Films on YAG," Appl. Phys. Ltrs. 13, 93 (1968).

9. J. L. Archer, W. L. Bongianni, and J. H. Collins, "Magnetically Tunable Microwave Bandstop Filters Using Epitaxial YIG Film Resonators," J. Appl. Phys. 41, 1359 (1970).

10. W. L. Bongianni and L. Young, "Bandpass and Bandsectioning Filters Using Epitaxial YIG Films," IEEE-GMTT Microwave Symposium, Newport Beach, Calif. May 11-15, 1970.

11. F. A. Pizzarello, J. H. Collins, and L. E. Coerver, "Magnetic Steering of Magnetostatic Waves in Epitaxial YIG Films," J. Appl, Phys. 41, 1016 (1970).

12. W. L. Bongianni, J. H. Collins, F. A. Pizzarello, and D. A. Wilson, "Propagating Magnetic Waves in Epitaxial YIG," IEEE-GMTT Microwave Symposium, Dallas, Texas May 5-8, 1969. Published in Proceedings, p. 376-380.

13. J. H. Collins and G. R. Pulliam, "Microwave Integrated Circuits Utilizing Epitaxial YIG Films," Invited paper at International Conf. on Ferrites, Kyoto, Japan, July 1970.

14. W. L. Bongianni, "Epitaxial YIG Microwave Circuits", Technical Report AFAL-TR-71-275, Aug. 1971.

15. B. F. Stein, "Magnetic Properties of GdIG Films Grown by Chemical Vapor Deposition", J. Appl. Phys. 41, 1262 (1970).

16. B. F. Stein and M. Kestigian, "Effect of Lattice and Thermal Mismatch on the Coercive Force of GdIG Films," J. Appl. Phys. 42, 1806 (1971).

17. B. F. Stein, "Growth and Some Magnetic Properties of GdIG Films," J. Appl. Phys. 42, 2336 (1971).

18. E. Sawatzky and E. Kay, "Preparation of Garnet Films by Sputtering," J. Appl. Phys. 39, 4700 (1968).

19. R. M. Josephs, "The Effect of Annealing on Sputtered GdIG Films", IEEE Trans Magnetics MAG-6, 533 (1970).

20. J. E. Mee, D. M. Heinz, T. N. Hamilton and G. R. Pulliam, "Chemical Vapor Deposition of Epitaxial Magnetic Oxides," Invited paper at Symposium on Materials for Information Storage at Electrochemical Society Meeting, Los Angeles, May 1970.

21. J. E. Mee, G. R. Pulliam, D. M. Heinz, J. M. Owens and P. J. Besser, "Mobile Cylindrical Domains in Epitaxial Ga:YIG Films," Appl. Phys. Letters, 18, 60 (1971).

22. D. M. Heinz, P. J. Besser, J. M. Owens, J. E. Mee, and G. R. Pulliam, "Mobile Cylindrical Magnetic Domains in Epitaxial Garnet Films," Invited paper at 16th Annual Conference on Magnetism and Magnetic Materials, Miami Beach, Nov. 1970, J. Appl. Phys. 42, 1243 (1971).

23. G. R. Pulliam, J. E. Mee, D. M. Heinz, P. J. Besser and J. H. Collins, "Formation and Characterization of Epitaxial Magnetic Oxide Films," Invited paper at International Conference on Ferrites, Kyoto, Japan, July 1970.

24. D. M. Heinz, P. J. Besser, P. E. Elkins, H. L. Glass, J. E. Mee and L. A. Moudy, "Epitaxial Film Growth of Bubble Domain Materials", Technical Report AFML-TR-71-126, June 1971.

25. D. M. Heinz, P. J. Besser, P. E. Elkins, J. E. Mee, L. A. Moudy and J. M. Owens, "Single Crystal Orthoferrites for Memory Applications", Technical Report TR ECOM-0258-1, May 1971.

26. McD. Robinson, A. H. Bobeck and J. W. Nielsen, "Chemical Vapor Deposition of Magnetic Garnets for Bubble Domain Devices," IEEE Trans. Magnetics MAG-7, 464 (1971).

27. L. K. Shick, J. W. Nielsen, A. H. Bobeck, A. J. Kurtzig, P. C. Michaelis and J. P. Reekstin, "Liquid Phase Epitaxial Growth of Uniaxial Garnet Films: Circuit Deposition and Bubble Propagation." Appl. Phys. Letters 18, 89 (1971).

28. H. J. Levinstein, R. W. Landorf and S. Licht, "A Rapid Technique for the Heteroepitaxial Growth of Thin Magnetic Garnet Films", IEEE Trans. Magnetics, MAG-7, 470 (1971).

29. J. E. Geusic, H. J. Levinstein, S. J. Licht, L. K. Shick and C. D. Brandle, "Cylindrical Magnetic Domain Epitaxial Films with Low Defect Density," Appl. Phys. Letters 19, 93 (1971).

30. A. H. Bobeck, "Properties and Device Applications of Magnetic Domains in Orthoferrites," Bell System Tech. J. 46, 1901 (1967).

31. A. H. Bobeck, R. F. Fischer, A. J. Perneski, J. P. Remeika and L. G. Van Uitert, "Application of Orthoferrites to Domain Wall Devices," IEEE Trans. Magnetics MAG-5, 544 (1969).

32. J. F. Dillon, "Observations of Domains in Ferrimagnetic Garnets by Transmitted Light", J. Appl. Phys. 29, 1286 (1958).

33. U. F. Gianola, D. H. Smith, A. A. Thiele and L. G. Van Uitert, "Material Requirements for Circular Magnetic Domain Devices," IEEE Trans. Magnetics MAG-5, 558 (1969).

34. J. W. Nielsen, "Properties and Preparation of Magnetic Materials for Bubble Domains," Met. Trans 2, 625 (1971).

35. L. G. Van Uitert, D. H. Smith, W. A. Bonner, W. H. Grodkiowicz and G. J. Zydzik, "Hexagonal Ferrites for Bubble Domain Devices," Matl. Res. Bull. 5 455 (1970).

36. A. H. Bobeck, et. al, "Uniaxial Magnetic Garnets for Domain Wall Bubble Devices," Appl. Phys. Lett. 17, 131 (1970).

37. A. A. Thiele, "The Theory of Cylindrical Magnetic Domains" Bell System Tech. J. 48, 3287 (1969).

38. J. Smit and H. P. J. Wijn, Ferrites (John Wiley and Sons, New York, 1959).

39. R. C. Sherwood, L. G. Van Uitert, R. Wolfe and R. C. Le Craw, "Variation of the Reorientation Temperature and Magnetic Crystal Anisotropy of the Rare-Earth Orthoferrites," Phys. Letters 25A, 297 (1967).

40. S. Geller, "Crystal Chemistry of the Garnets," Z. Krist. 125, 1 (1967).

41. E. F. Bertaut, F. Sayetat and F. Tcheou, "Magnetic Order of Tb^{3+} in $Tb_3Fe_5O_{12}$ at Low Temperature," Solid State Comm. 8, 239 (1970).

42. A. Rosencwaig, W. J. Tabor, F. B. Hagedorn and L. G. Van Uitert, "Noncubic Magnetic Anisotropies in Flux-Grown Rare-Earth Iron Garnets," Phys. Rev. Lett. 26, 775 (1971).

43. A. Rosencwaig, W. J. Tabor and R. D. Pierce, "Pair-Preference and Site-Preference Models for Rare-Earth Iron Garnets Exhibiting Noncubic Magnetic Anisotropies," Phys. Rev. Lett. 26, 779 (1971).

44. H. Callen, "Growth-Induced Anisotropy by Preferential Site-Ordering in Garnet Crystals," Appl. Phys. Lett. 18 311 (1971).

45. C. D. Mee, "The Magnetization Mechanism in Single-Crystal Garnet Slabs Near the Compensation Temperature," IBM J. Res. Develop. 11, 468 (1967).

46. S. H. Charap and J. M. Nemchik, "Behavior of Circular Domains in GdIG," IEEE Trans. Magnetics MAG-5, 566 (1969).

47. G. R. Pulliam, "Chemical Vapor Growth of Single Crystal Magnetic Oxide Films," J. Appl. Phys. 38, 1120 (1967).

48. P. J. Besser, J. E. Mee, P. E. Elkins and D. H. Heinz, "A Stress Model for Heteroepitaxial Magnetic Oxide Films Grown by Chemical Vapor Deposition," Mat. Res. Bull. 6, 1111 (1971).

49. A. H. Bobeck, E. G. Spencer, D. H. Smith and L. G. Van Uitert, "Magnetic Properties of Flux-Grown Uniaxial Garnets," IEEE Trans. Magnetics MAG-7, 461 (1971).

50. D. M. Heinz, P. J. Besser and J. E. Mee, "Cylindrical Magnetic Domains in Gallium-Substituted Erbium Iron Garnet Prepared by Chemical Deposition," Presented at the 17th Annual Conference on Magnetism and Magnetic Materials, Chicago, Nov. 1971.

51. P. J. Besser, J. E. Mee, D. M. Heinz, T. N. Hamilton, P. E. Elkins and E. C. Whitcomb, "Film-Substrate Matching Requirements for Bubble Domain Formation in CVD Garnet Films" Presented at 17th Annual Conference on Magnetism and Magnetic Materials, Chicago, Nov. 1971.

52. S. Schneider, R. S. Roth, and J. L. Waring, "Solid State Reactions Involving Oxide of Trivalent Cations", J. of Research, NBS 65A, 345 (1961).

53. R. C. Linares, "Growth of Garnet Laser Crystals", Solid State Communications, 2, 229 (1969).

54. A. F. Witt and H. C. Gatos, "Microscopic Rates of Growth in Single Crystals Pulled from the Melt: Indium Antimonide," J. Electrochemical Soc., 115, 70 (1968).

55. H. Kuhnl and W. Ernst, "Darstellung von wasserfreiem $FeCl_2$, $CrCl_2$, $FeBr_2$, and $CrBr_2$," Z. Anorg. u. Allgem. Chem 317, 84 (1962).

56. S. Geller, G. P. Espinosa, and P. B. Crandall, "Thermal Expansion of Yttrium and Gadolinium Iron, Gallium and Aluminum Garnets," J. Appl. Cryst. 2, 86 (1969).

57. Thermophysical Properties of High Temperature Materials, Vol. 4, Part II, Y. S. Touloukian, Ed., 1967, pp 1663-1664.

58. G. R. Pulliam, "Chemical Vapor Growth of Single Crystal Magnetic Oxide Films", J. Appl. Phys. 38, 1120 (1967).

59. U. K. Bonse, M. Hart and J. B. Newkirk, "X-Ray Diffraction Topography" Adv. in X-ray Anal. 10, 1 (1967).

60. A. R. Lang, "Direct Operation of Individual Dislocations by X-Ray Diffraction", J. Appl. Phys. 29, 597 (1958), 30, 1748 (1959).

61. A. H. Compton and S. K. Allison, "X-rays in Theory and Experiment", D. Van Nostrand, New York (1935) p709ff.

62. J. Basterfield, M. J. Prescott, and B. Cockayne, J. Matls, Sci. 3, 33 (1968).

63. B. Johnson and A. K. Walton, "The Infrared Refractive Index of Garnet Ferrites," British J. Appl. Phys. 16, 475 (1965).

64. B. F. Stein, Private Communication

65. J. F. Dillon, "Observation of Domains in Ferrimagnetic Garnets by Transmitted Light" J. Appl. Phys. 29, 1286 (1958).

66. J. M. Nemchik, "Circular Domain Configuration in GdIG," J. Appl. Phys. 40, 1086 (1969).

67. S. H. Charap and J. M. Nemchik, "Behavior of Circular Domains in GdIG," IEEE Trans. Magnetics, MAG-5, 566 (1969).

68. A. J. Kurtzig and F. B. Hagedorn, "Noncubic Magnetic Anisotropies in Bulk and Thin Film Garnets," IEEE Trans. Magnetics, MAG-7, 473 (1971).

69. G. F. Dionne, "Magnetic Moment versus Temperature Curves of Ferrimagnetic Garnet Materials," Technical Report #480 Lincoln Laboratory, MIT., Sept. 1970.

70. A. H. Bobeck, R. F. Fischer, A. J. Perneski, J. P. Pemeika and L. G. Van Uitert, "Application of Orthoferrites to Domain Wall Devices," IEEE Trans. Magnetics MAG-5, 544 (1969).

71. B. F. Stein and M. Kestigian, "Effect of Lattice and Thermal Mismatch on the Coercive Force of GdIG Films," J. Appl. Phys. 42, 1806 (1971).

72. R. L. Comstock, E. B. Moore and D. A. Nepela, "Magnetic Properties of Tb-Substituted GdIG Films Chemically Deposited on YAG Substrates," IEEE Trans. Mag, MAG-6, 558 (1970).

73. F. C. Rossol, "Domain Wall Mobility in Rare Earth Orthoferrites by Direct Stroboscopic Observation of Moving Domain Walls," J. Appl. Phys. 40, 1082 (1969).

74. A. H. Bobeck, "A Second Look at Magnetic Bubbles," IEEE Trans. Magnetics, MAG-6, 445 (1970).

75. B. A. Calhoun, E. A. Geiss and L. L. Rosier, "Dynamic Behavior of Domain Walls in Low Moment Yttrium - Gallium - Iron Garnet Crystals," Appl. Phys. Letters 18, 287 (1971).

76. D. C. Leo, D. A. Lepore and J. W. Nielsen, "Dependence of the Magnetic Properties of $Y_3Fe_{5-x}Ga_xO_{12}$ and $Y_3Fe_{5-x}Al_xO_{12}$ on Thermal History", J. Appl. Phys. 37, 1083 (1966).

77. F. Euler, B. R. Capone and E. R. Czerlinsky, "Effects of Heat Treatment on the Magnetic Properties of Substituted YIG," IEEE Trans. Magnetics MAG-3, 509 (1967).

78. A. J. Perneski, "Propagation of Cylindrical Magnetic Domains in Orthoferrites", IEEE Trans. on Magnetics Vol. MAG-5, 554 (1969).

79. D. M. Heinz, L. A. Moudy, P. E. Elkins and D. J. Klein, "Properties of the Dysprosium-Gadolinium Gallium Garnet System", Presented at the 13th Annual Conference on Electronic Materials Committee of the Metallurgical Society of AIME, San Francisco, Aug. 30, 1971.

80. A. Axelrad and H. Callen, "Growth-Induced Anisotropy Arising from the Tetrahedral Sites in Garnets", to be published in Appl. Phys. Letters, Dec. 1971.

81. W. J. DeBonte, "Theory of the Static Stability of Thick-Walled Cylindrical Domains in Uniaxial Platelets", 17th Annual Conference on Magnetism and Magnetic Materials, Chicago, Nov. 1971.

82. F. B. Hagedorn, "Domain Wall Motion in Bubble Domain Materials" 17th Annual Conference on Magnetism and Magnetic Materials, Chicago, Nov. 1971.

83. M. Sparks "Ferromagnetic Relaxation Theory", McGraw-Hill (1964).

84. Ferromagnetic Resonance, S. Vonsovskii, ed. Pergamon Press, 1966.

85. A. H. Marrish, The Physical Principles of Magnetism, Wiley, 1965.

86. E. A. Geiss, B. E. Argyle, B. A. Calhoun, D.C. Cranemeyer, E. Klokholm, T. R. McGuire and T. S. Plaskett, "Rare Earth - Yttrium Iron-Gallium Garnet Epitaxial Films For Magnetic Bubble Domain Applications, Mat. Res. Bull. 6, 1141 (1971).

87. W. A. Crossley, R. W. Cooper, J. L. Page and R. P. van Stapele "Faraday Rotation in Rare-Earth Iron Garnets", Phys. Rev. 181, 896 (1969).

NEW TECHNOLOGY APPENDIX

The major accomplishment of this program was the achievement of epitaxial films of GaYGdIG that display good bubble domain characteristics. The best film/substrate combination was $Y_{2.4}Gd_{0.6}Fe_{4.0}Ga_{1.0}O_{12}/Gd_3Ga_5O_{12}$ (see Sections 4.2.5, 5.1.7 and 6.1).

Other advances included:

1. Establishing necessary deposition conditions for growing smooth films (p 40 - 45).

2. Growing single crystals of several gallium garnets which had not been previously reported (Section 4.1). They were the unsubstituted garnets NdGaG and SmGaG and the mixed garnets NdGdGaG, NdSmGaG and SmGdGaG.

3. Performing thermal expansion experiments which show that variations in thermal expansion coefficient with gallium garnet compositions is less than two percent for the compositions investigated (Section 5.2).

4. Obtaining the first X-ray topographs of epitaxial bubble garnet films (section 5.4.2.3).